General approach to high power, coherent visible and ultraviolet light sources

Andersen, Martin Thalbitzer; Tidemand-Lichtenberg, Peter; Pedersen, Christian

Publication date:
2009

Document Version
Publisher's PDF, also known as Version of record

M. T. Andersen

General approach to high power, coherent visible and ultraviolet light sources

Martin Thalbitzer Andersen was born on the 30th of June, 1978 in Copenhagen (Herlev), Denmark. He studiet Applied Physics at Technical University of Denmark from 1999 to 205, here he quickly turned towards the field of optics and laser physics and recieved his candidate degree (Civilingeniør) in December 2005 for the thesis *"Development of laser systems for bio-photonic applications"*. After the candidate degree he was offered a Ph.D position to continue his work in the field of nonlinear optics.

Currently Martin Thalbitzer Andersen is employed as postdoc at Risø DTU, here he is working on a miniaturized version of the Risø reader, a project founded by European Space Agency (ESA). The aimfor this project is to build a reader that should be sent to Mars for dating sediments.

Martin Thalbitzer Andersen er født den 30. juni 1978 i København (Herlev), Danmark. Han studerede Teknisk Fysik på Danmarks Tekniske Universitet fra 1999 til 2005, her viste det sig hurtigt at det var optikken og laser fysikken der var interessant, og han opnåede sin kandidatgrad (Civilingeniør) i december 2005 for afhandlingen *"Development of laser systems for bio-photonic applications"*. Efter kandidatgraden fik han et tilbud om et ph.d. stipendiat så han kunne fortsætte sit arbejde inden for ikke lineær optik.

I øjeblikket er Martin Thalbitzer Andersen ansat som postdoc på Risø DTU og arbejder på en miniature udgave af Risø readeren, et projekt, der støttes af den Europæiske Rumfarts Organisation (ESA). Målet med projektet er at bygge en reader, som skal datere aflejringer på Mars.

DTU Physics
Department of Physics
Technical University of Denmark

Fysikvej
Building 309
2800 Kongens Lyngby
Denmark
Tel: +45 45 25 33 44

www.fysik.dtu.dk

ISBN 978-87-993734-0-6

General approach to high power, coherent visible and ultraviolet light sources

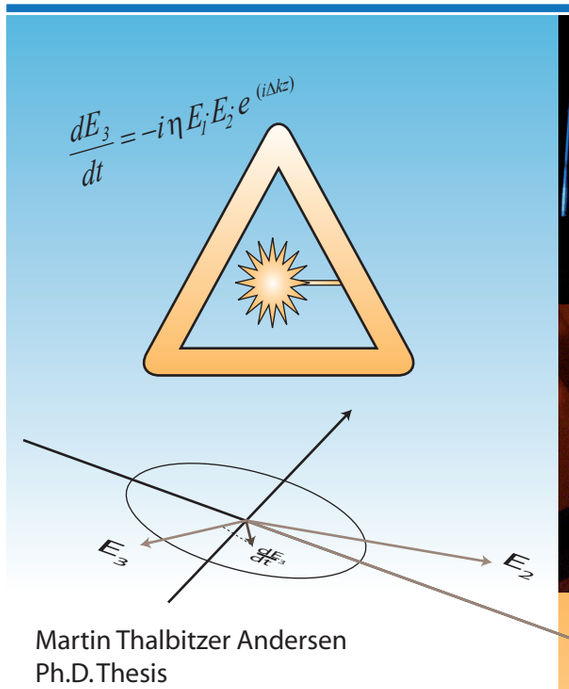

Martin Thalbitzer Andersen
Ph.D. Thesis
April 2009

DTU Physics
Department of Physics

DTU Physics
Technical University of Denmark

General approach to high power, coherent visible and ultraviolet light sources

Martin Thalbitzer Andersen

Ph.D. Thesis
submitted for the degree of
Doctor of Philosophy in Physics

Supervisors:

Associate Professor Peter Tidemand-Lichtenberg

Associate Professor Christian Pedersen

April 2009

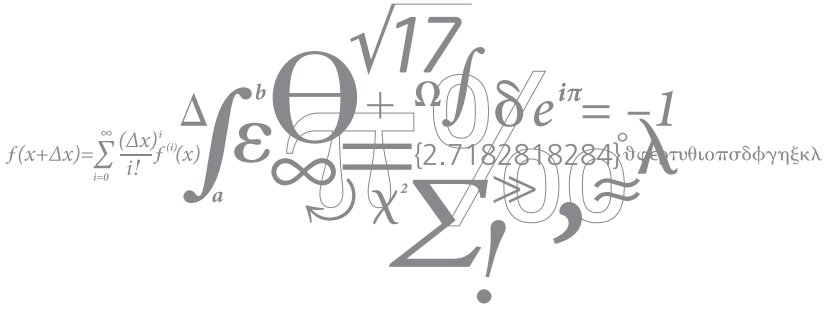

ISBN: 978-87-993734-0-6
Printed by Jespersen Tryk+Digital, Copenhagen, Denmark

Abstract

The main goal of this project is to develop a generic approach to synthesise any wavelength in the visible and UV spectral region based on sum frequency generation. The approach is based on a hybrid system combining solid state and semiconductor technology.

The generation of light in the UV spectral region require nonlinear materials with a transparency range extending into the ultraviolet, the ability to sustain high photon energies and with the ability to obtain phasematching for the desired nonlinear conversion process. In this project experiments are conducted using three differently co-doped GdCOB crystals. The crystals are optimized for noncritical phasematching in the blue-UV spectral region through co-doping with Lu and Sc, a nonlinear coefficient for these crystals of 0.78, 0.81 and 0.89 pm/V are measured, which is comparable to LBO. The ability to adjust the noncritical phasematching by co-doping of these crystals makes them promising candidates for generation of light in the blue-UV region.

A novel method for cavity dumping based on nonlinear frequency conversion is investigated. A high finesse laser is constructed with an intracavity nonlinear material inserted in a beam waist. The nonlinear material is phasematched to support sum frequency generation between the 1342nm circulating field in the cavity and a single pass passively Q-Switched 1064nm laser, effectively converting the circulating power whenever a single pass pulse is present. Furthermore the Q-Switched laser can easily be frequency doubled in a single pass configuration, therefore the nonlinear cavity dumping approach is suggested for the generation of 340nm UV light, using 532nm pulses to cavity dump a 946nm Nd:YAG laser. Furthermore experiments are conducted tripling a Q-switched 1064nm laser to 355nm by cascaded second harmonic and sum frequency generation using periodically poled KTP and BBO for the SHG and SFG process, respectively. The 355nm light is used to promote different photo induced reactions.

The main limitation of reaching any desired wavelength in the visible spectrum using sum frequency generation is the limited laser lines available from efficient solid state lasers. One fundamental way to overcome this limitation is to use semiconductor lasers to provide one of the fundamental fields. The problem of using semiconductor lasers for nonlinear frequency conversion has previously been the lag of coherence of these devices. This problem can, however, to a large extent be solved using external cavity tapered diode lasers, which allows for the generation of coherent radiation at the watt power level. Using differently doped semiconductor materials these devices can potentially cover the wavelength range from the red and into the infrared spectral range. These devices are very efficient, however, the available devices in the visible region are still very inefficient, therefore a generic approach using high finesse solid state lasers with intracavity nonlinear materials and single pass tapered diode was sought to cover the shorter wavelength range.

In this project more then 300mW of 488nm power is generated by direct sum frequency mixing of a solid state laser and a single pass external cavity tapered diode laser. The performance of the device is compared to systems where the output of the tapered diode laser is spatially filtered and to an all solid state laser system based on mixing with a single frequency Ti:Sapphire laser.

Finally experiments with a semiconductor disk laser used as the high finesse cavity laser and sum frequency mixing with a single pass solid state laser is con-

ducted. These experiments show that it is possible to design systems exploiting the benefits of semiconductor based lasers and nonlinear sum frequency generation to cover large parts of the optical spectrum, which has previously been difficult to access due to the lag of efficient, coherent light sources

Resumé

Hoved målet med dette projekt er a udvikle et generisk princip til at lave enhver bølgelængde i det synlige og UV del af det optiske spektrum. Princippet er baseret på sum frekvens generering (SFG) mellem et hybrid system bestående af solid state og halvleder teknologi.

Lyskilder i UV delen af det optiske spektrum kræver materialer der er gennemsigtige, modstandsdygtige mod høje optiske intensiteter, samtidig med at det skal være velegnet til fasematch af den ikke lineære proces. I dette projekt bliver der udført forsøg med tre forskelligt doterede GdCOB krystaller. Krystallerne er optimeret for ikke kritisk fasematch i det blå og UV del af det optiske spektrum, ved hjælp af forskellige doteringer med Lu og Sc. Den ikke lineære koefficient for disse krystaller er blevet fundet til 0.78, 0.81 and 0.89 pm/V, dette er sammenligneligt med LBO. Evnen til at ændre den ikke kritiske fasematch ved ændring af doteringen for disse krystaller gør dem oplagt som materiale for ikke lineær frekvens konvertering i den blå og UV del af det optiske spektrum

En ny metode til at tømme en laser kavitet baseret på ikke lineær frekvens konvertering bliver undersøgt. En høj finesse kavitet med ikke lineære materiale placeret i en beam waist i kaviteten er blevet bygget. Det ikke lineære materiale er fasematchet til SFG mellem kavitetens 1342nm felt og en Q-switched 1064nm laser, dette konverterer effektivt det cirkulerende felt i kaviteten, hver gang en puls fra 1064nm laseren rammer det ikke lineære medie. Derudover kan en pulset laser effektivt blive frekvens fordoblet i en single pass konfiguration. Derfor er det ikke lineære kavitets tømnings metode også forsøgt anvendt til generering af 340nm UV lys, ved at bruge 532nm pulser fra en doblede 1064nm laser til at tømme en 946nm Nd:YAG laser kavitet. Desuden er der blevet udført et eksperiment til tredobling af 1064nm pulsen til 355nm. Ved hjælp af en kaskade proces af anden harmonisk generering og derefter SFG i periodisk polet KTP og BBO. 355nm lyset er derefter brugt til forskellige fotokemiske forsøg.

Begrænsningen for at når en hvilken som helst bølgelængde i det synlige spektrum ved brug af SFG, er det beskedne antal laser linjer som eksisterer for effektive solid state lasere. En metode til at omgå denne begrænsning er ved at bruge halvleder lasere som en af laser kilderne. Problemet ved at bruge halvleder lasere til frekvens konvertering skyldes deres dårlige kohærens. Dette problem vil bliver forsøgt løst ved at bruge ekstern kavitets taperede diode lasere, da disse tillader generering af kohærent lys i watt området. Ved at bruge forskellige legeringer af halvleder materialer kan denne type laser porentielt dække bølgelængde området fra rødt lys til det infrarøde. Disse lasere er meget effektive, mens de eksisterende halvleder materiale i det synlige område er ret ineffektive. Derfor er det med denne generiske tilgang, hvor en høj finesse solid state kavitet med et ikke lineært medie placeret internt i kaviteten og en halvleder single pass taperet diode, forsøgt at dække de kortere bølgelængder.

I dette projekt bliver der genereret mere end 300mW effekt ved 488nm ved SFG mellem en solid state laser og en taperet diode laser. Dette system er sammenlignet med systemer hvor den taperede diode laser bliver rumligt filtreret og et rent solid state system, baseret på mixing med en Ti:Safir ringlaser

Til sidst er der blevet udført et eksperiment med en halvleder disk laser. Denne er brugt som laser i en høj finesse kavitet, hvor single pass laseren er en solid state laser. Systemet viser at det er muligt at udnytte fordelene ved halvleder lasere og

SFG til at dække store dele af det optiske spektrum, som tidligere har været svært at nå på grund af manglen på effektive kohærente lyskilder.

Preface

This thesis is based uppon the research undertaken between March 2006 and February 2009 at DTU Physics and Risø DTU, Technical University of Denmark, Kongens Lyngby, Denmark and at Institute of Photonics, Strathclyde University, Glasgow, Scotland. This Ph.D. project was financed by the Danish Technical Research Council, grant 274-050377, and under supervision by Associate professor Peter Tidemand-Lichtenberg and Associate professor Christian Pedersen.

Firstly, I would like to express my gratitude towards my supervisor Associate Professor Peter Tidemand-Lichtenberg for supervision and guidance throughout this project. His door is always open and he is ready for discussions nearly at any time without any prearranged scheduled meeting. I would also like to thank my second supervisor Christian Pedersen, especially for his direct approach for acknowledging ones work.

I would like to thank all the people in the optics group, DTU Physics at Technical University of Denmark for their interest in my project, a special thanks to Mikael Ø. Lassen, Anders Tipsmark, Metin Sabunco and Alexander Huck for useful discussions and funny contributions throughout the years as a master student and Ph.D. student. A special thanks goes to Emir Karamemehdović for the collaboration and great team work throughout this project. I also want to acknowledge the help from my fellow Ph.D. student Haynes Chen during the final writing.

Also a thanks to my professor Preben Buchhave, who always seems to have the time for whatever theoretically problem in the field of optics that I have encountered during my study as Ph.D. A special thank goes to the optics group technician Søren Hjort for fixing and assembling whatever known or unknown equipment that is needed in a certain experiment.

During my Ph.D project I spend two months at Institute of Photonics, Strathclyde University in Glasgow, Scotland, and I would like to express my gratitude towards Dr. Jennifer E. Hastie for her great knowledge and experience in the field of lasers, and her open-minded hospitality towards guest researches like me.

A special thanks goes to Peter J. Schlosser for the team work during the uncountable hours in the lab, and his well organised lab notes. Also I would like to thank all the people at the Institute for there warm hospitality they showed me. A special thank goes to the fellow students Loyd McKnight, Antony Smith, Caroline Muellenbroich and Rolf Birch for creating a cosy atmosphere during my stay. I would like to thank Dr. John Mark Hopkins and Dr. Stephane Calvez for their quick and useful response when asking for detailed information's about technical drawings.

For the small chemical experiment I would like to thank my brother Henrik T. Andersen, Frederik Diness and Line Kessel for helping me out with explaining the chemical issues.

At last I would like to thank my family and friends for the support they showed me during the study and especially during the final writing of this thesis.

Martin Thalbitzer Andersen
April, 2009

Contents

Chapter 1

Introduction

The understanding of the physics that eventually lead to the development of the laser, was laid in the end of the 19^{th} century, when Max Planck solved the problem of the blackbody radiation in 1899 [1]. He could do so only by postulating that the electromagnetic field had to be quantized in photons with energy $h\nu$, where h is Planck's constant and ν is the frequency of the electromagnetic wave [2]. In 1905 Einstein took this quantized model for the electromagnetic field and used it to give a simple explanation for the nature of absorption of light in matter [3]. As an example he used this model to explain the photoelectric effect, which was first observed in 1839 by Becquerel. In 1917 Einstein proposed a combined theory for absorption, spontaneous emission and stimulated emission based on probability coefficients, and the foundation for the invention of the laser was laid [4]. The first system based on amplification by stimulated emission was, however, the maser (microwave) and was built in 1953 by Townes *et al.* [5]. Though in 1960 T. Maiman demonstrated the first optical maser and had it published in *Nature* since it was rejected for publishing in *Physical Review Letters* [6]. The acronym LASER which is the term used today was invented by G. Gould and appeared the year before in his conference paper *"The LASER, Light Amplification by Stimulated Emission Radiation"* to emphasise that it was light instead of microwave [7]. At that time the laser was seen as *"a solution looking for a problem"* though today no one doubt the usefulness of the laser, and it is used virtually everywhere, e.g. in medicine, science, communications, welding and more.

Later the same year as Maiman demonstrated the ruby laser the first gas laser was built by Ali Javan *et al.* and it was based on a mixture of Helium and Neon gasses (HeNe laser) [8]. Probably the most important laser today is the semiconductor diode laser which account for more than 90% of all lasers sold in total. It was proposed by Nicolay G. Basov and the first demonstration of a semiconductor laser diode was made in 1962 by Robert N. Hall [9]. This laser diode was based on gallium and arsenide (GaAs) emitting light at 850nm, it was, however, necessary to use liquid nitrogen to cool the diode under operation, and it took eight years before the first semiconductor based laser diode was operated at room temperature, the breakthrough was to use a heterostructure of GaAs and aluminium doped GaAs (AlGaAs) instead of pure GaAs [10]. Becasue the use of heterostructured layers makes it possible to tailor the bandgap i.e the lasing wavelength and other properties of the semiconductor diode laser, this technique is widely used in the fabrication of these devices today.

1.1 Nonlinearity

Nonlinear behavior such as the Pockels and Kerr effect were observed already in the end of the 19th century. Also saturation effects in the luminescence of dye molecules was observed in 1941 before the invention of the laser [11]. Though quickly after the invention of the laser, new nonlinear effects was observed, and harmonic generation of the oscillating wavelength was first observed only one year later in 1961 by Franken *et al.* Here Second Harmonic Generation (SHG) of a ruby laser generating 347nm light was done using quartz as the nonlinear material [12]. The efficiency was, however, very low as quartz exhibit a very small nonlinear coefficient. For more efficient frequency conversion the nonlinear material needs to be optimized for the wanted interaction and by increasing the intensity of the fundamental field the conversion can also be enhanced. The nonlinear frequency conversion is not limited to SHG alone, in fact SHG is a special case of the more general sum frequency generation (SFG) where two arbitrary oscillating fields are mixed to generate the sum of their frequencies as demonstrated in 1962 by Miller *et al.* [13]. The opposite process can also occur where the two interacting oscillating fields generate the difference between the two frequencies, this is referred to as difference frequency generation (DFG). There are many different approach for optimizing the conversion, in chapter 2 some of these important methods for optimizing the nonlinear frequency conversion are explained.

1.1.1 Material optimisation

For optimum frequency conversion the phase velocity of the fundamental wave(s) and the SHG(SFG) signal have to be matched in order for efficient energy transfer between them to take place. Phasematching is achieved when the phase velocity of the induced polarisation and the generated field are the same [1], and in some cases the birefringence of special materials can be adjusted to fulfil this. Typically the propagation direction in the material or the temperature of the material are used as tuning parameter to obtain phasematching.

There are, however, other ways to change the birefringence of a material to obtain the wanted phasematching, and as shown by Aka *et al.* GdCOB crystals with different co-doping of rare earth elements can be optimised for wavelengths in the blue-UV spectral region [14]. These wavelengths are difficult to get directly by solid state lasers and frequency conversion into the blue-UV region of the spectrum is therefore an area of high interest as high quality light sources have found an increasing number of applications in this particular wavelength range. They are used e.g. for optical data storage, color display, medical diagnostic (bio-markers) and psoriasis treatment. To achieve coherent light in this spectral region, frequency conversion of near infrared (NIR) diode-pumped solid-state lasers (DSSL) has proven to be an efficient, compact and less power consuming alternative to gas lasers. However the high energy of short wavelength photons are absorbed in many materials which can lead to optical damage even for low intensities. It is therefore difficult to generate a particular wavelength due to limitations in available materials. Crystals with high nonlinearity and low UV absorption are therefore a research area of high interest and in chapter 3 experiments conducted with three GdCOB crystals with co-doping of Lutetium and Scandium are presented.

[1] For SFG phasematching can be achieved when the refractive indices are not the same, though conservation of momentum has to be fulfilled.

1.1.2 Cavity enhanced frequency conversion

While the nonlinear coupling is very weak, conversion efficiency is proportional to the fundamental intensity squared (harmonic generation), and different enhancement schemes can be used to increase the nonlinear conversion. By placing the nonlinear material inside a cavity which is resonant for the fundamental wavelength the nonlinear coupling can be drastically improved. For sum frequency generation the dependence is linearly proportional to the incident power, and the coupling can be done either doubly resonant where the nonlinear media is placed in a cavity resonant for both fundamental fields and singly resonant where only one of the fields are resonant and the other is single passed through the nonlinear media. The benefits of using doubly resonant system is the high intensities of both fields, though due to the nonlinear coupling unwanted noise and intensity fluctuations can occur [15]. These noise characteristics are also seen in intracavity SHG and the term *green noise* is often used. In the singly resonant case green noise is absent and it is speculated that singly resonant sum frequency generation is less noisy compared to doubly resonant and intracavity second harmonic generation.

1.1.3 Cavity dumping

Nonlinear frequency conversion can also be done using pulsed laser sources. Generation of pulsed light can be done either passively or actively. Passively Q-switched lasers are simple and provide an easy and simple way for effective second harmonic frequency conversion due to relative high peak power achievable by this technique. Sum frequency generation on the other hand require some means of synchronising the pulses of two Q-switched lasers. One method for passively synchronisation between two laser cavities has been demonstrated by Tidemand-Lichtenberg *et al.* [16]. This method can, however, not be extended to any desirable wavelengths, and saturable components for synchronisation are required. The problem of synchronisation can be overcome if one of the interacting lasers runs under continuous wave operation, then conversion is done each time a pulse is incident on the nonlinear media. To enhance the obtainable energy and peak power of the generated pulse, the system can be build in a singly resonant configuration for the continuous wave laser, then each time a pulse is incident on the nonlinear media the high circulating intracavity power of the continuous wave laser is effectively dumped through the nonlinear interaction. Beside from being a simple way to generate pulsed light, this is also the first time nonlinear cavity dumping is demonstrated. Usually cavity dumping is based on the electronically controlled Pockels effect or acousto-optic effect. This novel scheme is presented in chapter 4.

1.1.4 Cascading to UV

To reach the UV region in a simple manner tripling and quadrupling of Q-Switched 1064nm lasers has been demonstrated using cascaded nonlinear materials first doubling the 1064nm light, and secondly either doubling the 532nm light or mixing the 532nm light with the residual 1064nm light. A 355nm laser based on cascading nonlinear materials is presented in chapter 5. Furthermore the possibility of combining the cascading with the cavity dumping scheme is briefly discussed, the combination shows that hard to get wavelengths can be generated and is here exemplified by generation of 340nm pulses.

1.2 Generic approach

Since the wavelength of solid state lasers is inherently determined by the atomic transitions of the lasing medium, only specific wavelengths can be generated with these types of lasers. The common approach for visible light sources have been limited to second harmonic generation, and applications are forced to adapt to the available light sources rather than the opposite. In the more general case of sum frequency generation more wavelengths can be reached, and high efficiencies have been demonstrated using all solid state lasers [17]. There is, however, a huge benefit by changing to semiconductor laser diodes. Firstly they have a very high electrical to optical conversion efficiency, secondly the bandgap can be engineered to target nearly any wavelength in the red-infrared region of the optical spectrum. Furthermore the broad gain bandwidth of diode lasers adds large tuneability to the generated light which is not possible with most solid state materials. A system targeting the 488nm laser line of Argon Ion lasers is presented in chapter 6. It is based on a hybrid between solid state technology and semiconductor technology. The performance of this hybrid system is then compared to a version where the mode of the single pass laser has been cleaned using a single mode polarisation maintaining fibre, before mixing with the solid state laser, in chapter 7. Finally these 488nm systems are compared to a solid state system, where the solid state laser consist of a single frequency Ti:S laser, in chapter 8.

1.2.1 Semiconductor Disk Laser

Thermal lensing can be a limiting factor in the performance of the laser. Lowering the doping of the laser material reduces thermal lensing, this however, reduce the absorption of the pump power, and a longer gain region is often needed, leading to strict design parameter in order to keep the mode overlap between the laser field and the pump [18].

To compensate for thermal effects Giesen *et al.* proposed the concept of thin disk lasers [19]. Here the heat flow is mostly axial instead of radial as seen in normal end pumped solid state systems, which reduces thermal lensing. The small length of the gain material, require a high doping concentration for efficient absorption of the pump, which limits the available solid state laser materials, since high doping can result in unwanted defects in the gain material.

Semiconductor materials exhibit a single pass gain, that are orders of magnitude larger than solid state laser materials, and the gain region can therefore be made very small. This makes it easier to effectively remove the heat induced by electrical or optical pumping, thereby reducing the thermal distortion when high thermal load is present and possibly allowing for power scaling of semiconductor based lasers to high power levels. Therefore moving towards an all semiconductor approach for the sum frequency system is of high interest, allowing the freedom of engineering both bandgaps for a specific sum frequency mixing process and the large tuning range of semiconductor materials potentially capable of providing, combined with the power scaling, the pathway to high power visible tuneable light sources is opened. Semiconductor materials is therefore an obvious candidate to use for high power thin disk lasers, and in chapter 9 a hybrid sum frequency system based on a singly resonant optically pumped semiconductor disk laser with the nonlinear material placed intracavity and a solid state single pass laser is presented.

1.3 Publications

The work presented in this thesis has been published in the following refereed journals and conference proceedings.

- *Singly-resonant sum frequency generation of visible light in a semiconductor disk laser*
  M. T. Andersen, P. J. Schlosser, J. E. Hastie, P. Tidemand-Lichtenberg, M. D. Dawson and C. Pedersen.
  Optics Express, Vol. **17**, Issue 8, 6010-6017, April 2009

- *Efficient visible light generation by mixing of a solid-state laser and a tapered diode laser*
  E. Karamehmedović, C. Pedersen, **M. T. Andersen** and P. Tidemand-Lichtenberg.
  Optics Express, Vol. **15**, Issue 19, 12240-12245, September 2007

- *Nonlinear cavity dumping of a high finesse frequency mixing module*
  P. Tidemand-Lichtenberg, **M. T. Andersen**, S. Johansson, C. Canalias, F. Laurell, P. Buchhave, E. Karamehmedović and C. Pedersen.
  Optics Express, Vol. **15**, Issue 15, 9799-9803, July 2007

- *First measurement of the nonlinear coefficient for* $Gd_{1-X}Lu_XCa_4O(BO_3)_3$ *and* $Gd_{1-X}Sc_XCa_4O(BO_3)_3$ *crystals*
  M. T. Andersen, J. L. Mortnsen, S. Germershausen, P. Tidemand-Lichtenberg, P. Buchhave, L. Gheorghe, V. Lupei and L. Pascal and G. Aka.
  Optics Express, Vol. **15**, Issue 8, 4893-4901, April 2007

- *Intracavity Frequency Mixing in a Semiconductor Disk Laser Generating* $>100mW$ *in the Yellow-Orange*
  J. E. Hastie, **M. T. Andersen**, M. D. Dawson and P. Tidemand-Lichtenberg
  ASSP 2009, MB22, (Poster, abstract), January 2009

- *Theoretical comparison of SHG and SFG Efficiencies for visible light generation*
  P. Tidemand-Lichtenberg, K. P. Sørensen, **M. T. Andersen**, P. Buchhave and C. Pedersen
  EOSAM 2008, TOM 6 002 948, (Poster, abstract), October 2008

- *Comparison of a Ti:S Laser and a Tapered External Cavity Diode Laser for Sum Frequency Generation in a High-Finesse 1342 nm Nd:*YVO_4 *Laser*
  M. T. Andersen, P. Tidemand-Lichtenberg, E. Karamehmedović and C. Pedersen.
  ASSP 2008, WB19, (Poster, abstract), January 2008

- *300 mW of coherent light at 488 nm using a generic approach*
  E. Karamehmedović, C. Pedersen, **M. T. Andersen** and P. Tidemand-Lichtenberg.
  Photonic West SPIE 2008, Vol. **6875**, (Oral, paper), January 2008

- *Generation of pulsed light in the visible spectral region based on non-linear cavity dumping*
  S. Johansson, **M. T. Andersen**, P. Tidemand-Lichtenberg, J. Janousek, P. Buchhave and F. Laurell.
  Nothern Optics 2006, T36, (Poster), 2006

- *Pulsed, all solid-state light source in the visible spectral region based on non-linear cavity dumping*
  P. Tidemand-Lichtenberg, **M. T. Andersen**, S. Johansson, J. Janousek, P. Buchhave and F. Laurell.
  ASSP 2006, TuB19, (Poster, abstract), January 2006

Chapter 2

Theory

2.1 Laser types

Today a wide variety of laser types exits such as gas-, solid state-, fibre-, semiconductor-, dye- lasers and many more. They all have properties which may be advantageous depending on the application. In this project the attention will be on solid state lasers and semiconductor lasers, their properties and characteristic will be explained in this section. Semiconductor based lasers are solid state lasers but they are usually considered by their own.

2.1.1 Solid state laser

The solid state technology is based on glass or crystalline materials as the *host* material, and *dopants* of typically rare earth elements are introduced. The atomic transitions of the *dopants* are used for the laser action and theoretically laser action is treated either as a three level or a four level scheme.

The four level system consist of four energy levels as seen on figure 2.1. In the absence of any pump source the system is in thermal equilibrium and the majority of electrons are found in the ground level (E0), when a pump photon with an energy corresponding to the transition from the ground level to the pump band, absorption of the photon can occur and the electron is transferred to the pump band (E3). The pump band is not a sharp level but, depending on the material and broadening mechanism it consist of discrete or continuous energy levels, and the pumping of the system may be accomplished with a broad band pump source. The lifetime of the pump band is short, and the electrons in the pump band are transferred to the upper state laser level (E2) due to nonradiative processes (phonons). From the upper laser level the electrons can transfer to the lower laser level (E1) by emitting a photon corresponding to the energy of the transition. The lower laser level also have a short lifetime and the electrons are returned to the ground level (E0) by nonradiative processes (phonons). For laser action to occur sufficiently feedback needs to be established and the gain has to exceeds the losses of the system and electrons are predominantly transferred to the lower laser level by stimulated emission. The advantage of a four level system is that due to the relative long lifetime of the upper laser level compared to the lower level population inversion is achieved even at very low pump powers, therefore four level systems tends to have a low threshold. furthermore since the laser action is achieved between two

intermediate energy levels, reabsorption of the laser field is also minimised since there are no transition from the ground level with the energy of the photons of the laser field. Thus reabsorption takes place for the minor populated lower laser level (E1) or by excited state absorption (ESA) in the case of higher-lying energy levels than depicted in the four level scheme.

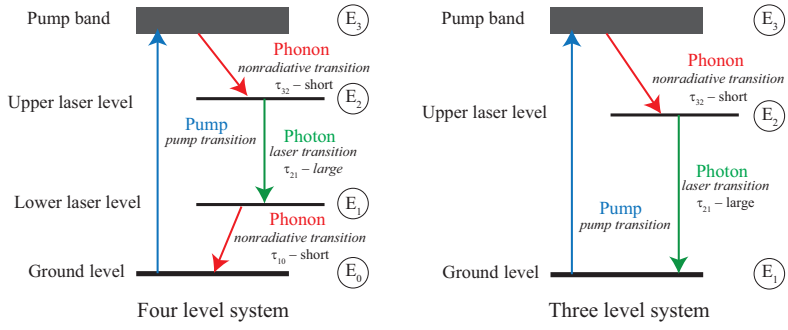

Figure 2.1: Schematic drawing of a three and four level system. For a three level laser the stimulated emission takes place between the upper laser level (E2) and the groundlevel (E1). For a four level system the stimulated emission is done between the upper laser level (E3) and the lower laser level (E2).

The three level system consists of three energy levels as seen on figure 2.1. Here laser action takes place between the upper laser level (E2) and the ground level (E1) directly, and as a consequence population inversion is first achieved when the electron density in the upper laser level is larger than in the ground level. Three level lasers therefore tends to have a higher threshold compared to four level systems. Because of the direct transition to the ground level reabsorption of the laser field can take place, transferring an electron to the upper laser level by absorption of a laser photon, this can result in selfpulsing as the part of the laser material without population inversion can act as a saturable absorber. Especially in fibre lasers where the gain region can be many metres selfpulsing have been observed [20, 21]. Therefore it is important that population inversion is present throughout the length of a three level gain media, and the length is usually adapted to the available pump power.

The most important doping element used in solid state lasers is neodynium(Nd), and for this work Nd doped yttrium orthovanadate (Nd:YVO_4) and Nd doped yttrium aluminium garnet (Nd:YAG) are used. Also Titanium doped Sapphire (Ti:S) is used for 488nm generation.

Nd:YVO_4

The Nd:YVO_4 material is a uniaxial birefringent crystal and the maximum gain is linear polarised along the π direction. The Nd:YVO_4 has a very strong absorption around 808nm and the absorption is polarisation dependent with the strongest absorption for pump light polarised in the same direction as the laser light. Because of stark splitting of the pump level the absorption profile is broadened and the spectra of common pump diodes at 808nm is therefore efficiently absorbed in

Nd:YVO_4 based lasers. The thermal conductivity is low compared to Nd:YAG crystal and because of the very strong absorption of pump power, thermal fracture can be an issue for high power systems [1]. To reduce the effect of the thermal load different schemes can be used such as: lowering the doping which increases the absorption length, adding an undoped region of pure YVO reduces the thermal gradient of the laser crystal and changing the pump source to a longer wavelength to minimise the Stoke shift between the pump and lasing wavelength, for example by direct pumping into the upper laser level [18, 22, 23].

Lasing can be achieved at three different transitions, namely 914nm, 1064nm and the 1342nm transition. The 914nm is a quasi three level system because the lower laser level correspond to the upper manifold of the $^4I_{9/2}$ level (ground level), which is thermal populated at room temperature according to the Boltzmann distribution [24]. The 1064nm and the 1342nm transitions can be treated as four level systems. In this work the 1064nm and the 1342nm transition is used for continuous wave operation.

Nd:YAG

Nd:YAG is the most used crystal for laser operation, due to its favourable properties, it has a high thermal conductivity compared to for example Nd:YVO_4. The Nd:YAG has strong absorption around 808nm though the absorption of Nd:YVO_4 is up to seven times stronger than for Nd:YAG at this wavelength. The YAG material is a isotropic crystal and therefore it has no preferred polarisation for absorption or emission, and in order to obtain linear polarised laser emission the insertion of polarising selective element such as a Brewster window is necessary. Due to its long upper state lifetime the Nd:YAG crystal is excellent for pulsed operation using continuous wave pumping. The main emission lines for Nd:YAG are the 946nm, 1064nm, 1319nm and the 1338nm transition, where the 946nm can be treated as a three level system, the others are all four level laser systems. In this work the 1064nm transition is used in Q-Switched operation, and the 946nm is considered for generation of pulsed 340nm UV light.

Ti:S

The titanium doped sapphire (Ti:S) crystal is of great interest because of its broad fluorescence bandwidth which allow tuneable output from 680nm to 1180nm, this very large gain bandwidth also allows for the generation of ultra short pulses [25].

The large gain bandwidth is due to the coupling of electronic energy levels and vibrational energy levels. On figure 2.2 a schematic representation of the energy structure for Ti:S is shown. Electrons are pumped into the pump band and relaxes to the bottom by vibrational relaxation (Upper laser level, E2). From the upper laser level the electron can decay into one of the lower energy levels by emission of a photon, and because of the broad lower band emission can take place from around 680nm to 1180nm. In this work the Ti:S laser is used for emission around 766nm [26].

[1] Thermal fracture of a 0.5% atm doped Nd:YVO_4 has been observed for a pump power of 25W at 808nm.

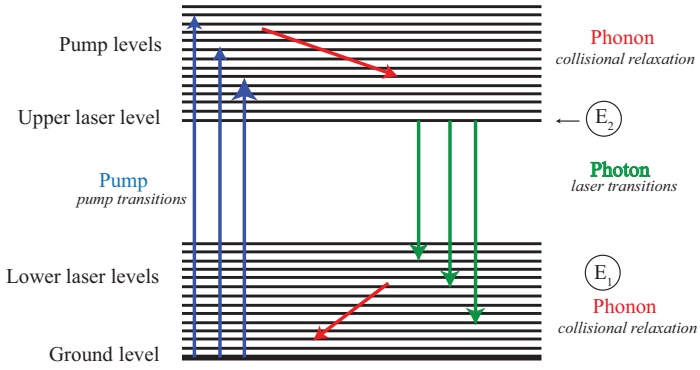

Figure 2.2: Schematic drawing of the energy levels for titanium sapphire.

2.1.2 Semiconductor materials

Semiconductor lasers are also solid state laser, but are usually considered as a group by its own. Semiconductor based lasers consists of alternating layers of alloyed dielectric materials. Usually elements such as Al, Ga, As, In and P is used and by changing the composition of these elements the bandgap can be engineered. A diagram showing the possible bandgaps as function of the composition is shown in figure 2.3. The direct bandgap materials are the ones suitable for light sources as they allow for direct transition between the conduction band (upper laser level) and the lower laser level (valence band), whereas for indirect bandgap materials direct transition require the assistance of phonons to occur. Indirect bandgap materials are, however, suitable as detectors. There are many types of semiconductor diode lasers such as broad area diodes (multimode), ridge waveguides (single mode), quantum dot, quantum wells etc. For this work Broad Area Laser (BAL) diodes, Tapered External Cavity Diode Laser (ECDL) and Semiconductor Disk Lasers (SDL) are used and these will be described in more detail in the following sections.

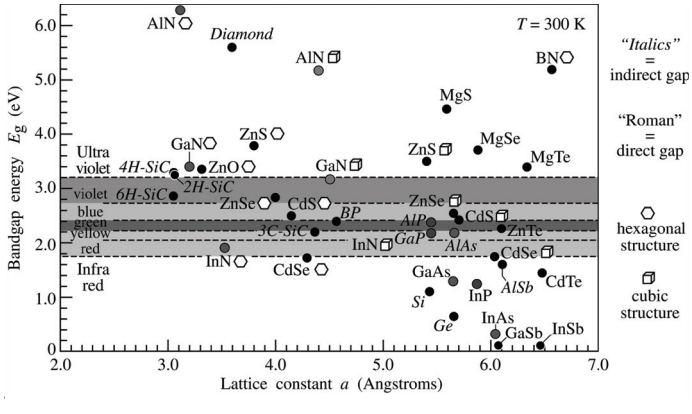

Figure 2.3: Lattice constant and bandgap for semiconductors at room temperature [27].

BAL

Broad area laser diodes are the most simple type of semiconductors diode lasers. The active gain area typically have dimensions of $1\mu m \times 100-200\mu m \times 500-800\mu m$ (height x width x length). This acts as a waveguiding structure emitting from the edge of the diode laser. With the highly asymmetrical structure of the diode the emission from the typically $1\mu m \times 100\mu m$ area the beam is close to single mode operation in the vertical plane with a M^2 value close to 1, whereas the horizontal plane contains multiple modes and the M^2 value is typically in the order of 20 or more, see equation 2.1 for definition of the M^2 value. The difference in the beam quality for the two directions denoted the fast axis (vertical plane) and the slow axis (horizontal plane) results in a difference in the divergence angle for the two planes. The spectral emission for a broad area laser diode is typically in the order of a few nanometres.

The M^2 value defines the deviation of the divergence angle of the beam to a diffraction limited Gaussian beam, and is often used to describe the quality of a beam.

$$\theta = M^2 \frac{\lambda}{\pi W_0} \tag{2.1}$$

Where W_0 is the beam waist and λ is the wavelength. The lowest value for M^2 is 1 as this defines the diffraction limit of a Gaussian beam. For higher values of M^2 it is seen that the far field divergence angle θ is increased and the M^2 tells how well a beam with a given beam divergence can be focused. For a BAL diode the multimode operation for the slow axis is seen do increase the M^2 factor. The beam quality can in general, not be described just by a single number as some properties of the beam may depend on other factors. BAL diodes are therefore usually used to pump solid state lasers, as the poor beam quality and poor coherence length of the emitted light can not be used directly for nonlinear frequency conversion.

Tapered Diode

To improve these properties different kind of feedback schemes can be applied. One way is to use injection seeding where a single frequency laser is used in order to force oscillation at a particular frequency, other method is to filter the emission of the diode itself and use it for selfseeding of the diode. These methods includes, but not limited to, Fabry-Perot cavity, diffraction grating and volume Bragg grating feedback mechanism [28–30]. While a huge improvement is seen in the emitted frequency spectrum, the spatial beam quality shows only minor improvements. Since the number of spatial number is inherently determined by the geometry of the active region in the semiconductor amplifier, single mode operation can be obtained by keeping the active region small so that it only supports one spatial mode, this, however, limits the output power of the diode. To improve both properties J. N. Walpole suggested to use a ridge waveguide in combination with a tapered section, such a structure is depicted at figure 2.4 [31].

The ridge waveguide is used to force single mode operation and the tapered section acts as an amplifier. The tapered angle is chosen to support the divergence of the single mode field emanating from the ridge waveguide. Depending on the coating of the rear facets, the tapered diode can act as a laser or a amplifier for a beam incident on the ridge waveguide. Because of the many parameters that

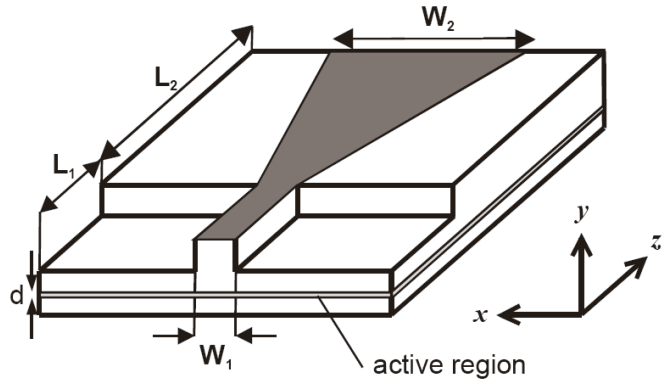

Figure 2.4: Schematic drawing of the tapered diode. d is the vertical thickness of the active region, W_1 is the lateral thickness of the ridge waveguide, W_2 is the lateral thickness of the tapered part at the output facets, L_1 is the length of the ridge waveguide and L_2 is the length of the tapered region. The tapered angle is typically around 6° [32].

influence the performance of the diode, the classification of different types of diodes is often given as a ratio between the output power and the quality factors of the emission. This is termed the brightness of the diode and is given as:

$$B = \frac{P}{A\Omega} \tag{2.2}$$

where P is the output power of the diode, A is the emitting area and Ω is the solid angle in which the power is emitted. When the beam is close to a divergence limited beam the brightness is given as.

$$B = \frac{P}{\pi W_0^2 \pi \theta^2} \overset{\text{eq 2.1}}{=} \frac{P}{\pi W_0^2 \pi \left(\mathrm{M}^2 \frac{\lambda}{\pi W_0}\right)^2} = \frac{P}{\left(\mathrm{M}^2\right)^2 \lambda^2} \approx \frac{P}{\lambda^2} \tag{2.3}$$

In this work the tapered diode is used in the Littrow configuration, here the small emission from the AR coated rear end of the ridge waveguide is collimated and incident on a diffraction grating, the first order reflection is then used as feedback. This ensures single frequency operation and the ridge waveguide structure suppresses oscillations at high order transverse modes. By tilting the grating the wavelength of the tapered diode can be tuned within the gain bandwidth of the diode [33, 34]. This ensures a compact and simple system where the tapered diode provide its own feedback. While the tapered structure in combination with the ridge waveguide do indeed improve the beam quality of the output, the difference in the vertical and horizontal geometry of the output facet introduce a slow and a fast axis (astigmatism) where the typical larger horizontal dimension gives rise to a virtual focal point located inside the diode depending on the pump current applied to the tapered diode. For the vertical dimension the focal point is located at the facet of the diode [35].

VECSEL - SDL

An alternative to the tapered diode is the optically pumped vertical external cavity surface emitting laser (VECSEL) or semiconductor disk laser (SDL). Similar to solid state disk lasers the optically pumping of the SDL allows for power scaling with the pump spot size and maintaining of high beam quality [36]. Since semiconductor materials exhibit very high gain coefficient compared to regular solid state materials, it is especially suited for the thin disk concept, as the small vertical dimension allows for efficient heat removal, though still maintaining a high gain. The structure of a typical SDL is shown at figure 2.5. The distributed Bragg reflector act as the rear mirror, usually high reflective over the gain bandwidth of the SDL.

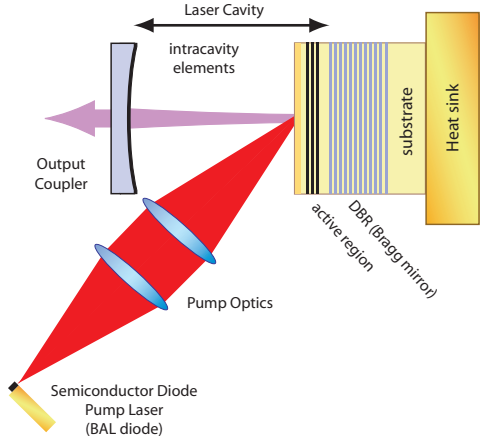

Figure 2.5: Schematic drawing of the SDL structure. DBR is the distributed Bragg reflector which act as the end mirror, the active region is the gain structure of the SDL consisting of either quantum wells or planes of quantum dots. The pumping is incident at an relatively large angle though due the axial cooling and the small size, thermal issues such as thermal lensing is reduced [37].

The active region is made of quantum wells or planes of quantum dots. On top of the active region a carrier confinement window is placed this layer is added to prevent pump generated carrier to be lost to nonradiative recombinations, finally a small protective layer is deposited to protect the structure. In many configurations a intracavity heatspreader is bonded on the SDL to increase heat removal, the most common heatspreader is diamond since it has the highest known thermal conductivity and is transparent in the spectral region of most SDLs. Just as the tapered diodes SDLs have a large tuning range typically between 10nm to 20nm. This structure is used as the intracavity gain media in the SFG system described in chapter 9

2.2 Nonlinear Optics - Frequency conversion

When an electromagnetic wave $\mathscr{E}$ is propagating through a dielectric medium it induces a dipole polarisation $\mathscr{P}$. In many cases this induces polarisation in the material can be considered linear, i.e. it depends linearly on the applied field strength. Though after the invention of the laser it was possible to generate very intense electromagnetic fields, and the linear approximation may no longer be valid, this was first observed by Franken *et al.* in 1961 [12]. A representation of a linear and nonlinear medium are show on figure 2.6. If we express the dipole polarisation $\mathscr{P}$

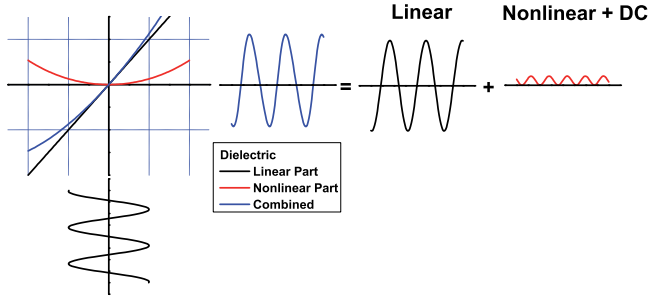

Figure 2.6: The response for a linear and a nonlinear dielectric medium

as a power series of the field strength $\mathscr{E}$, we get

$$\mathscr{P} = \epsilon_0 \left[\chi^{(1)} \mathscr{E} + \chi^{(2)} \mathscr{E}^2 + \chi^{(3)} \mathscr{E}^3 + \cdots \right] \tag{2.4}$$

The $\chi^{(1)}$ is the linear susceptibility, and gives the linear response of the media. $\chi^{(2)}$ and $\chi^{(3)}$ are called the second and third order nonlinear optical susceptibility tensor respectively. These are responsible for most for the nonlinear effects exploited in the field of nonlinear optics. For simplicity the medium is assumed lossless. In centrosymmetric materials $\chi^{(2)}$ is zero, and $\chi^{(3)}$ is the most important nonlinear term this is the case for liquids, gasses and fibres [38]. Whereas in noncentrosymmetric such as crystalline materials $\chi^{(2)}$ is many orders of magnitude larger than $\chi^{(3)}$. Throughout this work only processes for noncentrosymmetric materials are exploited, and $\chi^{(3)}$ effects are mostly ignored. It should be mentioned that where $\chi^{(2)}$ is absent in centrosymmetric materials, $\chi^{(3)}$ is still present in noncentrosymmetric materials. It is convenient to represent $\chi^{(2)}$ in terms of the nonlinear coefficient d, and we have that $\chi^{(2)} = 2d$, the change is minor but is widely used.
Since the $\chi^{(2)}$ term has a $\mathscr{E}^2$ dependence, the interaction can involve two fields which generate, amplify or diminish a third field, this is termed Three Wave Mixing(TWM). $\chi^{(3)}$ which has a $\mathscr{E}^3$ dependence gives four fields interaction and hence is regarded Four Wave Mixing(FWM).

2.3 Coupled wave equation

The interaction between light and matter are conveniently described in terms of the nonlinear wave equation which can be derived from Maxwell's equations [38]:

$$\nabla^2 \mathscr{E} - \mu_0 \epsilon_0 \epsilon \frac{\partial^2 \mathscr{E}}{\partial t^2} = \mu_0 \frac{\partial^2 \mathscr{P}^{NL}}{\partial t^2} \tag{2.5}$$

where μ_0 is the vacuum permeability, ϵ_0 is the permittivity of free space and $\epsilon = (1 - \chi_0)$ is the relative permittivity. The nonlinear response of the media is seen to act as a source term on the right hand side. For free space propagation in vacuum this source term is "0" and equation 2.5 is just the linear wave equation. In the case of a second order nonlinear media the third order terms and higher can be neglected, and $\mathscr{P}^{NL}$ is given by $\mathscr{P}^{NL} \approx 2\epsilon_0 d \mathscr{E}^2$.

In the case of three monochromatic, collimated (plane wave approximation) and continuous wave incident on a lossless medium, the electric field $\mathscr{E}$ is then given as a superposition of three interacting waves, with angular frequencies ω_1, ω_2, ω_3 and electric field amplitudes A_1, A_2 and A_3. With z direction chosen as the propagation axis the electric field is given as:

$$\mathscr{E}(z,t) = \sum_{n=1,2,3} \frac{1}{2} \left(A_n \cdot e^{i(k_n z - \omega_n t)} + c.c. \right) \tag{2.6}$$

where $k_n = n_n \omega_n / c$, $\epsilon(\omega) = n_n^2$ and c.c. is the complex conjugate. The factor $1/2$ in front is just a convenient scaling of the amplitudes, ensuring that $|\mathscr{E}_n| = A_n \cdot \sin(k_n z - \omega_n t)$. The induced nonlinear polarisation can now be evaluated by inserting equation 2.6 into $\mathscr{P}^{NL}$, this gives a sum of 36 terms (including the complex conjugate) which include all the possible interactions, and with some rewriting the nonlinear polarisation can be written as:

$$\mathscr{P}^{NL} = \frac{1}{2} d \epsilon_0 \sum_{n,m=\pm1,\pm2,\pm3} A_n A_m e^{i(k_n + k_m)z - (\omega_n + \omega_m)t} \tag{2.7}$$

where $\omega_{-n} = -\omega_n$, $k_{-n} = -k_n$ and $A_{-n} = A_n^*$. Despite the many terms, only some of them are different from zero when looking at a specific material and state of the interacting fields [39]. For the case of sum frequency generation where $\omega_3 = \omega_1 + \omega_2$ and ignoring terms for SHG and OR equation 2.7 simplifies into three nonlinear radiating terms, by identifying the terms oscillating at the same frequency on the left and right hand side of the equation:

$$\mathscr{P}_1^{NL} = d \epsilon_0 A_3 A_2^* e^{i(k_3 - k_2)z - (\omega_3 - \omega_2)t} + c.c. \tag{2.8}$$

$$\mathscr{P}_2^{NL} = d \epsilon_0 A_3 A_1^* e^{i(k_3 - k_1)z - (\omega_3 - \omega_1)t} + c.c. \tag{2.9}$$

$$\mathscr{P}_3^{NL} = d \epsilon_0 A_1 A_2 e^{i(k_1 + k_2)z - (\omega_1 + \omega_2)t} + c.c. \tag{2.10}$$

Now $\mathscr{E}(z,t)$ can be inserted on the left hand side of equation 2.5 and the corresponding $\mathscr{P}^{NL}$ is inserted on the right hand side which gives three coupled equations, and for ω_3 the equation is given as:

$$\begin{aligned} &\frac{1}{2} \left(\left[\frac{d^2 A_3}{dz^2} + 2ik_3 \frac{dA_3}{dz} - A_3 k_3^2 + A_3 \frac{\epsilon(\omega_3)\omega_3^2}{c^2} \right] \cdot e^{i(k_3 z - \omega_3 t)} + c.c. \right) \\ &\quad = \frac{\omega_3^2 d}{c^2} A_1 A_2 e^{i(k_1 + k_2)z - (\omega_1 + \omega_2)t} + c.c. \end{aligned} \tag{2.11}$$

The two last terms inside the hard brackets is seen to cancel out each other, and the time oscillation can be also be removed on both sides since $\omega_3 = \omega_1 + \omega_2$. The resulting equation can then be written as:

$$\frac{1}{2}\left(\frac{d^2A_3}{dz^2} + 2ik_3\frac{dA_3}{dz}\right) = \frac{\omega_3^2 d}{c^2}A_1A_2e^{i(k_1+k_2-k_3)z} \tag{2.12}$$

By applying the slowly varying envelope approximation:

$$\left|\frac{d^2A_3}{dz^2}\right| \ll \left|k_3\frac{dA_3}{dz}\right| \tag{2.13}$$

Which is valid as long as the fractional change in the amplitude A_3 is much smaller than unity on the scale of an optical wavelength, equation 2.12 can be simplified further, and for the three interacting fields these relations are found to:

$$\begin{aligned}
\frac{dA_1}{dz} &= -\frac{i\omega_1}{n_1c_0}dA_3A_2^*e^{-i\Delta kz} \\
\frac{dA_2}{dz} &= -\frac{i\omega_2}{n_2c_0}dA_3A_1^*e^{-i\Delta kz} \\
\frac{dA_3}{dz} &= -\frac{i\omega_3}{n_3c_0}dA_1A_2e^{i\Delta kz}
\end{aligned} \tag{2.14}$$

where $\Delta k = k_1 + k_2 - k_3$.

Assuming that the two input fields can be considered constant for an interaction length L, which is valid as long as the conversion is not too strong, $A_3(L)$ can then be found by integration:

$$A_3(L) = -\int_0^L \frac{i\omega_3}{n_3c_0}dA_1A_2e^{i\Delta kz}dz = -\frac{i\omega_3}{n_3c_0}dA_1A_2\left(\frac{e^{i\Delta kL}-1}{i\Delta K}\right) \tag{2.15}$$

$$\tag{2.16}$$

The intensity can be found from the electric amplitude to.

$$I_n = \frac{1}{2}n_n\epsilon_0c_0\left|A_n\right|^2 \tag{2.17}$$

And I_3 is then given as:

$$\begin{aligned}
I_3 &= \frac{1}{2}n_3\epsilon_0c_0\left|A_3\right|^2 = \frac{\epsilon_0\omega_3^2}{2n_3c_0}d^2\left|A_1\right|^2\left|A_2\right|^2\left|\frac{e^{i\Delta kL}-1}{i\Delta K}\right|^2 \\
&= \frac{2\omega_3^2d^2}{\epsilon_0n_1n_2n_3c_0^3}I_1I_2\left|\frac{e^{i\Delta kL}-1}{i\Delta K}\right|^2 = \frac{2\omega_3^2d^2}{\epsilon_0n_1n_2n_3c_0^3}I_1I_2L^2\mathrm{sinc}^2\left(\frac{\Delta kL}{2}\right)
\end{aligned} \tag{2.18}$$

Assuming that the interacting beams are circular the power can be found as:

$$P_n = I_n\pi W_n^2 \tag{2.19}$$

where W_n is the spot size (radius) of the beam. Substituting equation 2.19 into equation 2.18 the power of the generated beam can be written as:

$$P_3 = \frac{2\omega_3^2d^2L^2}{\pi\epsilon_0n_1n_2n_3c_0^3}\frac{W_3^2}{W_1^2W_2^2}P_1P_2\mathrm{sinc}^2\left(\frac{\Delta kL}{2}\right) \tag{2.20}$$

Here the linear dependence on the incident power to the generated power is clearly seen, and the phasemismatch in the sinc function is seen to reduce the coupling efficiency. The L^2 dependence found in this expression originates from the plane wave approximation used. Considering focused Gaussian beams the expression is found to [40]:

$$P_3 = \frac{4\omega_3^2 d^2 L}{\pi\epsilon_0 n_1 n_2 n_3 c_0^3} \frac{k_1 \cdot k_2}{k_3} P_1 P_2 h_m \tag{2.21}$$

Where h_m is the Boyd Kleinman factor.

2.3.1 Optical parametric processes for $\chi^{(2)}$

For the most general case two electromagnetic fields, with angular frequencies ω_1 and ω_2 are both incident on a nonlinear dielectric media. The nonlinear induced polarisation namely $\chi^{(2)}\tilde{\mathscr{E}}^2$ then contains spectral components at 0, $2\omega_1$, $2\omega_2$, $\omega_1+\omega_2$, $\omega_1-\omega_2$. Thus frequencies are generated at all possible combinations of differences or sums of the incident beams, these processes are termed Difference Frequency Generation(DFG) and Sum Frequency Generation(SFG)[2]. The degenerate case where $\omega_1 \cong \omega_2$ the incident field interact with itself, the first "0" term is Optical Rectification(OP), which is a widely used technique for terahertz generation [43, 44]. The second and third term is the process of Second Harmonic Generation(SHG) and was observed shortly after the invention of the laser [12].

Even though the two beams at frequencies ω_1 and ω_2 induces polarisation densities in the nonlinear medium at all combinations 0, $2\omega_1$, $2\omega_2$, $\omega_1+\omega_2$, $\omega_1-\omega_2$ on a microscopic scale, they are in general not observed at the same time, since each process require different conditions in order to coherently add up on a macroscopic scale. The full derivation of the second order nonlinearity from Maxwell's equations is not undertaken here and is treated in various textbooks and papers such as [38, 45, 46].

The physical conditions that has to be fulfilled for each process is energy conservation ($\omega_3 = \omega_1 + \omega_2$), which states that the total energy is the same before and after the nonlinear interaction. To establish macroscopic energy transfer between the interacting beams, conservation of momentum or phasematching also has to be fulfilled. By changing the phasematching conditions one selects one of the mentioned interactions. Where the energy condition is simple in the sense that it always apply, phasematching can be difficult to obtain.

2.4 Phasematching

Conservation of momentum or phasematching is the second requirement and this is the one that allows for the optimisation of a desired process. The phasematch condition is reversible, so a NonLinear Optical (NLO) media made for SFG of $\omega_1+\omega_2$ giving ω_3, is also phasematched for the opposite process of splitting ω_3 into ω_1 and ω_2, although the relative phase between the interacting fields decides the direction of energy flow. For example if the incident fields are very strong compared to the

[2]For the difference frequency generation the ω_2 is amplified in the same process because of energy conservation, this is called Optical Parametric Amplification (OPA) of ω_2. If only one ω_1 is incident on the media optimized for DFG ω_2 will be generated as spontaneous emission[41, 42], this interaction is called Spontaneous Parametric Down Conversion (SPDC).

interaction length backconversion can occur. Though as shown in chapter 4 by placing the nonlinear media intracavity this phenomenon is more complicated.

To maximise a particular interaction of interest, each dipole induced in the nonlinear media must add up constructively as the fields propagate through the media, to generate a macroscopic field of the wanted interaction.

$$\boldsymbol{k}_1 \pm \boldsymbol{k}_2 = \boldsymbol{k}_3 \Leftrightarrow \boldsymbol{k}_1 \pm \boldsymbol{k}_2 - \boldsymbol{k}_3 = \boldsymbol{0} \tag{2.22}$$

where $\boldsymbol{k}_n$ is the wavevector with numerical value defined as $|k_n| = \frac{2\pi n_n}{\lambda_n}$. The equation states that the total length of the interacting wavevector has to be equal to the total length of the generated field wavevector. Though it may seem simple, equation 2.22 can be difficult to fulfil and for some interaction it may not even be possible if only the bulk material properties are taken into account. The most common way to achieve phasematching is to make use of the birefringence of the material. Nonlinear materials have different refractive indices for different propagation direction and polarisation of light(Uniaxial and Biaxial crystals). Using Birefringent Phase Matching(BPM) the phasemismatch between the interacting beams may be offset by appropriate choice of propagation direction through the NLO crystal. In general high frequencies have higher refractive indices compared to lower frequencies, and phasematch can only be achieved by polarising the high frequency along the extraodinary axis(negative uniaxial crystals) and the ordinary axis(positive uniaxial crystals)[38]. The limitation of this kind of phasematching is that the nonlinear coefficient that is present for the direction where the interaction is phasematched can be small or even zero, also walk off is experienced if propagation is not taking place along the principal axis of the material, since the propagation direction for the extraordinary beam, $\boldsymbol{k_e}$, in general does not coincide with the pointing vector $\boldsymbol{s}$. In the case where the propagation do coincide with the principal axis phasematching is termed NonCritical PhaseMatching (NCPM). As shown chapter 3 crystals can be specially made where impurities(dopants) are introduced to alter the refractive indices of the NLO crystal. Here instead of choosing the right angle through the crystal for phasematching, doping material is added to the NLO crystal until phasematching can be achieved along one of the principal axis in the crystal [47, 48]. For more properties on common nonlinear optical crystals most of them are listed in *"Handbook of Nonlinear Optical Crystals"* [49].

A different approach is to use noncollinear phasematching. The difference between collinear (scalar) and noncollinear(vector phase matching) and are shown on figure 2.7, it is clear that collinear phasematching can be more efficient compared to noncollinear as the interaction length decreases for increasing angle between the interacting waves. This, however, may be the only way to offset the phasemismatch.

To distinguish between different ways of achieving phasematching, typically phasematching is divided into three main groups, termed Type I, Type II and Type III and they are listed in table 2.1. Here type III is regarded as the case where all interacting beams are polarised in the same direction. For Type I both fundamentals are either ordinary or extraordinary waves and the generated is polarised along the opposite axis. For Type II phasematching the two fundamentals are orthogonal polarised, one along the ordinary and the other along the extraordinary axis of the crystal, and depending on the crystal the generated signal is polarised along the ordinary or the extraordinary axis. As mentioned the pointing vector does not in general coincide with the extraordinary axis and as a consequence the interacting length for type I and II is in general not equal to the full length of the crystal. In

Type I the generated beam and for Type II the fundamental polarised along the extraordinary axis can experience walk off.

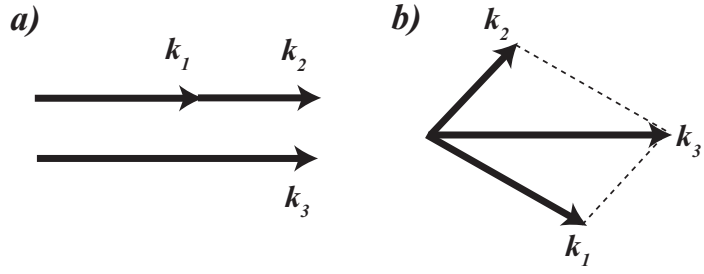

Figure 2.7: a) Scalar phasematching all beams are collinear with each other, b) vector phase matching the interacting wavevector are vector phasematched

The third type of phasematching is in practise not possible using only the bulk properties of the NLO crystals. This interaction is however possible to achieve using a method termed Quasi Phase Matching(QPM) and the basic idea was mentioned by Armstrong in 1962 [45] and first demonstrated by Boyd *et al.* [50].

Table 2.1: Types of main phasematching for nonlinear crystals, ***o*** stands for ordinary and ***e*** for extraordinary polarisation

Type	Phasematching	Interaction	Crystal	Method
I	***ooe***	$\boldsymbol{k}_{o1} + \boldsymbol{k}_{o2} = \boldsymbol{k}_{e3}$	negative	BPM, QPM
	eeo	$\boldsymbol{k}_{e1} + \boldsymbol{k}_{e2} = \boldsymbol{k}_{o3}$	positive	BPM, QPM
II	***oee***	$\boldsymbol{k}_{o1} + \boldsymbol{k}_{e2} = \boldsymbol{k}_{e3}$	negative	BPM, QPM
	eoo	$\boldsymbol{k}_{e1} + \boldsymbol{k}_{o2} = \boldsymbol{k}_{o3}$	positive	BPM, QPM
III	***ooo***	$\boldsymbol{k}_{o1} + \boldsymbol{k}_{o2} = \boldsymbol{k}_{o3}$		QPM
	eee	$\boldsymbol{k}_{e1} + \boldsymbol{k}_{e2} = \boldsymbol{k}_{e3}$		QPM

2.4.1 Quasi Phasematching

The first demonstration of a single crystal exhibit alternating sign for the nonlinear coefficient was first done for $LiNbO_3$ in 1980 by Feng *et al.* [51]. The idea is to offset the accumulated phasemismatch between the interacting waves. This can be done by inversion of the nonlinear response of the media. By rotating a slice of the crystal structure 180 degrees around the propagation axis the nonlinear coefficient changes sign and the phasemismatch runs "backwards". A QPM crystal consists of many domains with a nonlinear coefficient alternating between $\pm d$ for propagation along the length of the crystal. Equation 2.22 is only valid when the interaction is perfectly phasematched, more generally it has the form:

$$\boldsymbol{k}_1 \pm \boldsymbol{k}_2 - \boldsymbol{k}_3 = \boldsymbol{\Delta k} \tag{2.23}$$

where $\boldsymbol{\Delta k}$ is the wavevector mismatch the "+" correspond to SFG and "-" to DFG. The phasemismatch between the interacting beams accumulates as they propagate along the media, and as long as this is less than π the two incident waves adds up

to the third wave, though when the phasemismatch exceeds π the energy flow is reversed and power flows back to the fundamental fields. The length it takes to reach a phasemismatch of π is denoted the coherence length l_c. This is a cyclic process and is illustrated at figure 2.8.

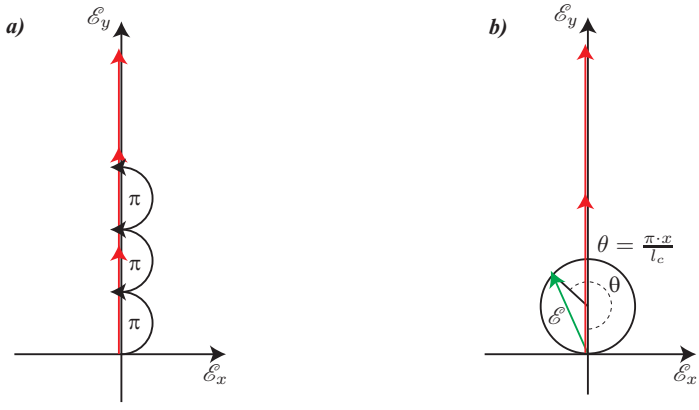

Figure 2.8: Schematic representation of the cyclic behavior of the phasemismatch [52]. Red line indicate the perfect phasemacth case, Black line periodically phasematching. Each arrow indicate the same length of interaction. a) The amount of conversion for a periodic QPM media compared to perfect phasematching, after each coherence length the crystal is inverted. The ratio between perfect phasematching and QPM is $\frac{2}{\pi} \approx 64\%$. b) Bulk media with no QPM structure. The generation will cycle periodically for each $2 \cdot l_c$.

The cyclic representation is also illustrative when looking at the effect of poling errors like random period errors and random duty cycle errors described by Fejer *et al.* [53]. In regular periodic poling techniques the most common problem is slight variation in the domain length. Depending on the technique used the variation is either Randomly Period Errors (RPE), which is the main error if the poled structure is assembled by individual plates of varying thickness. Here errors accumulate from the previous layers. The second type is Random Duty Cycle Errors (RDCE) here the average period is constant $\Lambda = 2 \cdot l_c$, but alternating layers can have local perturbed boundary errors. This is mainly the case where fabrication is done by a method maintaining the average position of the boundaries for example in lithographic fabrication [53]. At figure 2.9 the effect of up to 10% error in the periods is shown for a total of ten domains, the effect is seen to lower the efficiency slightly.

The error introduced for the poling structure not only reduce the conversion efficiency it also alter the shape of the acceptance bandwidth of the device. As the conversion efficiency decrease due to errors the spectral acceptance bandwidth increase, and for high efficiency periodically poled devices attempts are made to reduce these errors. Though by deliberately introducing changes in the poling structure the acceptance bandwidth can be tailored to a specific application, and some types of aperiodic structures are mentioned in section 2.4.1 and 2.4.1 of this chapter.

With QPM all the mentioned phasematching types given in table 2.1 can be made. The direction d_{33} usually has the highest nonlinearity but can only be exploited using Type III phasematching, so even though it may seem that BPM is advantageous over QPM in terms of higher conversion efficiency, the high d_{33} coef-

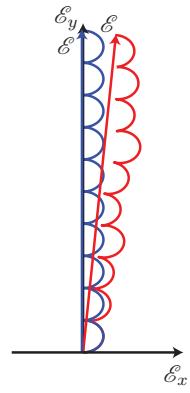

Figure 2.9: Red line: The effect of up to 10% error in the thickness of the individual layers for a total of ten domains. Blue line: Error free poling.

ficient combined with QPM can be many times more efficient compared to BPM. Since all waves for type III the phasematching is always noncritical in the same direction making this method even more favourable. On figure 2.10 a comparison between QPM and BPM for KTP is shown, the nonlinear coefficient used are $d_{33} = 15pm/V$ for the QPM crystal, and $d_{32} = 2.65pm/V$ is used for BPM. For some cases of interactions very small poling periods are required, and due to fabrications limitations a higher order of periodicity is chosen instead. The third order poling is also shown here each domain is $3 \cdot l_c$ long instead of just a single l_c, this reduce the effective nonlinear coefficient.

Mathematically the poling period is introduced as a propagation vector for the crystal itself, and without further proof it is given by:

$$\boldsymbol{k}_1 \pm \boldsymbol{k}_2 - \boldsymbol{k}_3 = \boldsymbol{\Delta k} - \boldsymbol{k}_{\boldsymbol{\Delta}}, \quad |k_\Delta| = \frac{2 \cdot \pi}{m \cdot \Delta} = \frac{2 \cdot \pi}{m \cdot 2 \cdot l_c} = \frac{\pi}{m \cdot l_c} \tag{2.24}$$

Where Δ is one poling period and m describes the order of poling. The length of each domain scales with m For $m = 1$ one period simply consist of two domains each with length $l_c = \frac{\Lambda}{2}$ with opposite nonlinear coefficient, in this way the relative phase between the fundamentals and generated is maintained for a energy flow towards the generated field. If the nonlinear coefficient is not altered the energy flow is reversed. For higher order phasematching the individual domain are given by $(m \times L_c)$. The cycling flow of energy though the odd number of coherence length secures that the energy eventually flow towards the generated harmonic wave.

Aperiodic poling

Periodic poling with inverted domains is the most efficient way to phasematch a single interaction using QPM, though more sophisticated method has been developed, and recent aperiodic poling has shown some interesting properties. If two interactions are to be phasematched at the same time the normal method is simply to place (cascading) two crystal after each other, where they each phasematch one of the two interactions. Though the limitations is that the crystal has to be in the right order as the second interaction can be dependent on the first one. An example is 355nm generation from a 1064nm light source, first part of the 1064nm

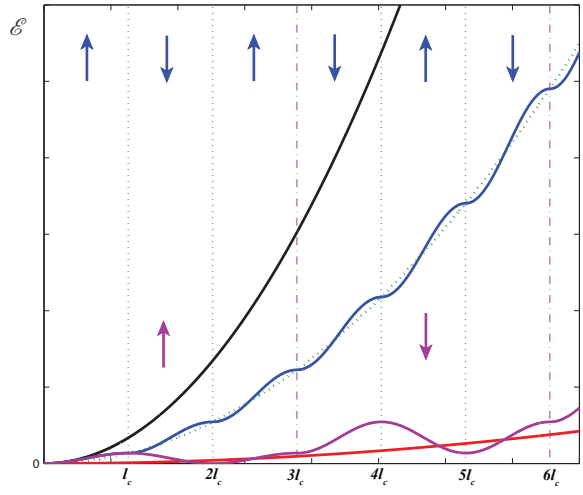

Figure 2.10: Diagram showing different ways to achieve phasematching, the vertically dashed lines indicate borders between normal and inverted domains. Black line shows the conversion if perfect phasematch for the d_{33} direction could be achieved. Blue line is for a periodically poled KTP and the green line shows the same just using an effective nonlinear coefficient. The red line shows BPM using a nonlinear coefficient of $d = 2.65$. The violet line shows a third order periodically poled KTP. The arrows indicate the poling corresponding to the line of the same color.

is frequency doubled to 532nm, and the two waves are then summed in the second crystal. These processes can be phasematched in a single crystal using aperiodic poling [54–56]. The principle is to construct a poling structure which has characteristic frequencies corresponding to the phasemismatch of the interactions which are going to be phasematched. In general a periodic function in real space(x) will give a peak in k-space at the periodic frequency. The restriction in real space is that the we can only allow for either +1 or -1 values for the nonlinear coefficient, zero is also a possibility though in order to get the highest efficiency this is not beneficial. The function for a 1-dimensional periodically poled structure in real space is simply given by:

$$g(z) = \text{sign}\left(\sin\left(k_1 \cdot z\right)\right) \tag{2.25}$$

The sign function ensures that structure only contain discrete values of 1 or -1. The simplest method to include one more interaction is to introduce a second sin function the following way:

$$g\left(z\right) = \text{sign}\left(C_1 \sin\left(k_1 \cdot z\right) + C_2 \sin\left(k_2 \cdot z\right)\right) \tag{2.26}$$

Here C_1 and C_2 are real constants $\in [-1, 1]$ that determines the relative nonlinear efficiency between the two interactions of the resulting structure. On figure 2.11 (a) the first part of the domain structure is shown and on (b) the corresponding k-space is given, the values used for this example is $k_1 = 0.3\mu$m, $k_2 = 0.5\mu$m, $C_1 = 0.95$ and $C_2 = 1$ and the total length of interaction is 1mm.

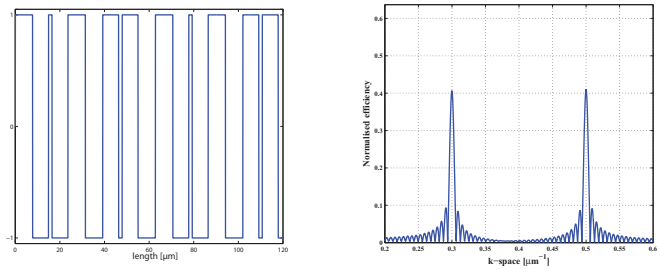

(a) (b)

Figure 2.11: (a) The first part of the structure for $k_1 = 0.3\mu$m and $k_2 = 0.5\mu$m. (b) The corresponding k-space for the given phasemismatch vectors. The efficiency is seen to be more than 40% of each interaction.

The method of construction the $g(z)$ using a simple sign and sine function to generate the structure can easily be generalised to handle an arbitrary amount of interaction by adding $C_n \sin(k_n \cdot z)$ terms.

$$g(z) = \text{sign}\left(\sum_{n=1}^{N} C_n \sin(k_n \cdot z)\right) \tag{2.27}$$

This function includes the wanted mismatch wavevectors at $k_n = \Delta k_n$, and the structure of the nonlinear material can be evaluated directly. The C_n coefficients can be varied in order to increase or lower the particular interaction. The method of multiple interaction can be expanded to the 2-Dimensional case and a detailed analysis can for example be found by Bahabad *et al.* [57] and Lifshitz *et al.* [58]

Recently an aperiodic KTP crystal for SHG of 1342nm and SFG of 1064nm and 1342nm has been tested and preliminary measurement shows the ability to phasematch the two interaction. The poling structure was designed for phasematching the two interaction at two different temperature. The measurement is shown at figure 2.12

Alternative poling

Other types of poling exits and some of them will be briefly mentioned here. A common method to obtain more than one type of QPM in one crystal, is to have channels with different periodicity see figure 2.13 (left). By translating the crystal perpendicular to propagation direction of the incident beams the appropriate channel can be selected. Another type of poling is the fanned structure where the poling periodicity changes from one side of the crystal to the other side of the crystal perpendicular to propagation direction. By translating the crystal the poling period changes continuously see figure 2.13 (centre). These two types of poling can be useful if the interacting beams can be tuned, since this typically changes the phasematch condition. A third type of poling is the chirped structure where the poling period changes throughout the crystal see figure 2.13 (right). This poling is especially suited for broad spectral frequency conversion as the acceptance bandwidth is larger. For short pulse frequency conversion the chirped structure can be

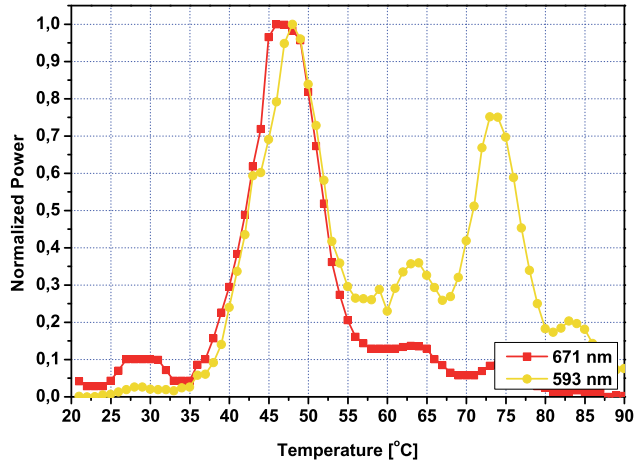

Figure 2.12: Temperature scan of the aperiodic KTP made for phasematching 1342nm + 1342nm = 671nm and 1342nm + 1064nm = 593nm. The measured phasematching temperatures are found to T_{SHG} = 46.5 ° C and T_{SFG} = 73.5 ° C. The extra peak for the yellow light is due to 671nm light leaking into the 593nm detector.

used for pulse compression of the generated beam.

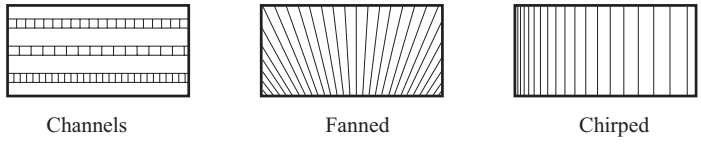

Figure 2.13: Schematic drawing of three types of poling. (left) Three channel poling with different periodic structure. (centre) fanned grating where the period changes continuously from one side of the crystal to the other. (right) chirped poling where the poling increases continuously through propagation.

Another type of poling is the random poling. Even though it may seem as a low efficient way to achieve the wanted interaction, it do have some interesting/special properties. Because of the randomness a random poled crystal contains a whole collection of reciprocal lattice vectors (k_Δ's) and as a consequence the wavelength acceptance bandwidth can be very large, though the efficiency will be low. Depending how the distribution of the reciprocal lattice vectors can be controlled the nonlinear efficiency as function of mismatch wavevector can be shaped to give the optimum response for the interacting waves. The idea of using random poling for phasematching has drawn much attention especially in very fast optics, where very broad acceptance bandwidths are needed, for example in the growing field of attosecond physics [55, 59]. One could expect that there would be no conversion at all as the different reciprocal lattice vectors interfere so they cancel each other out, and at specific **k** vectors this is also the case, but not in general. Such a random poled structure is shown on figure 2.14 a) using the same quadrature diagram from figure 2.8. The size for the individual domains are chosen to be completely random, in

the interval $[0, 2{\cdot}l_c]$, where $l_c = 6.3\mu m$ is the coherence length. The value specified is the wavevector mismatch for SFG between 1342nm and 1064nm in KTP for the d_{33} direction. The nonlinear efficiency as function of wavevector mismatch is shown on figure 2.14 b).

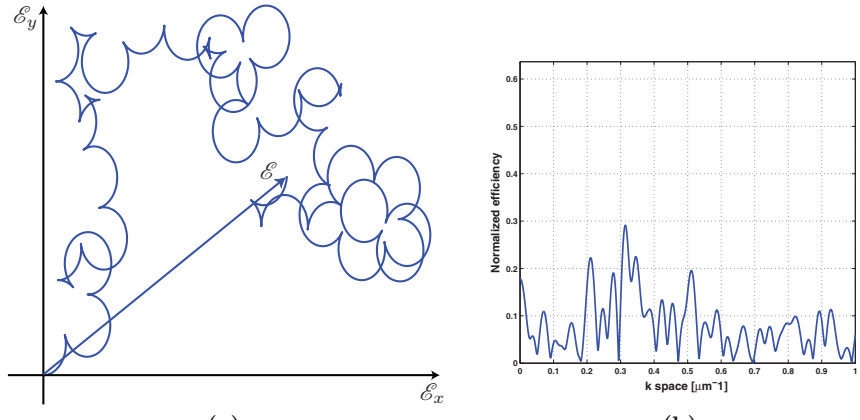

(a) (b)

Figure 2.14: A simulation for the efficiency for a random period crystal with 40 domains. (a) Phasewalk for a interaction with a coherence length of $l_c = 6.3\mu m$. (b) The nonlinear efficiency is low but broadened giving the possibility to phasematch over a large range.

2.5 General approach

In this project a general approach is sought, for synthesising reliable, compact coherent light sources with a predetermined wavelength in the visible and UV spectral range. The approach is based on sum frequency generation between two different light sources in the single resonant configuration, where the nonlinear material is placed intracavity in one of the laser resonator and the other light source is single passed through the nonlinear material see figure 2.15. As most solid state ma-

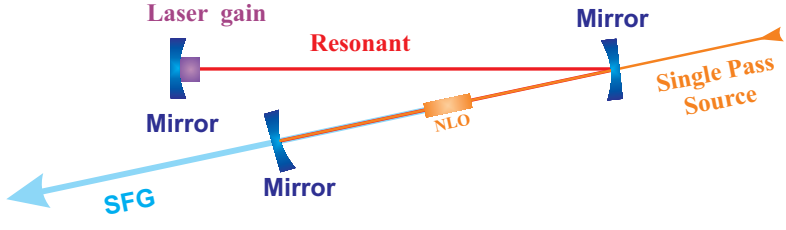

Figure 2.15: Schematic setup for the general approach for light generation.

terials are limited to a few atomic transition the usual route for generation of a predetermined wavelength in visible or UV light has been to generate third or forth harmonic of a Q-switched or mode-locked laser. This results in a wavelength in the UV region which is then downconverted using the UV light as pump source for a

optical parametric oscillator (OPO), and by angle tuning the nonlinear material of the OPO the predetermined wavelength can be reached [60, 61].

2.6 Generic approach

As shown on figure 2.3 a wide range of semiconductor materials are available that allows emission in the near infrared area, and a generic approach for synthesising any predetermined wavelength in the visible and UV spectral range based on a hybrid between solid state technology and semiconductor technology. By substituting the single pass source with a high power external cavity diode laser (ECDL), adding selection of centre wavelength and tuneability, and placing the nonlinear material intracavity in a solid state laser hereby exploring the high circulating fields found in some solid state laser. With this generic approach where no active components are needed the system can be made compact and simple. At figure 2.16 the reachable wavelength for such systems are shown for the most common solid state transition lines, namely 916nm, 946nm, 1064nm, 1319nm and 1342nm, mixed with common semiconductor wavelength potentially available from 650nm to 1150nm [3]

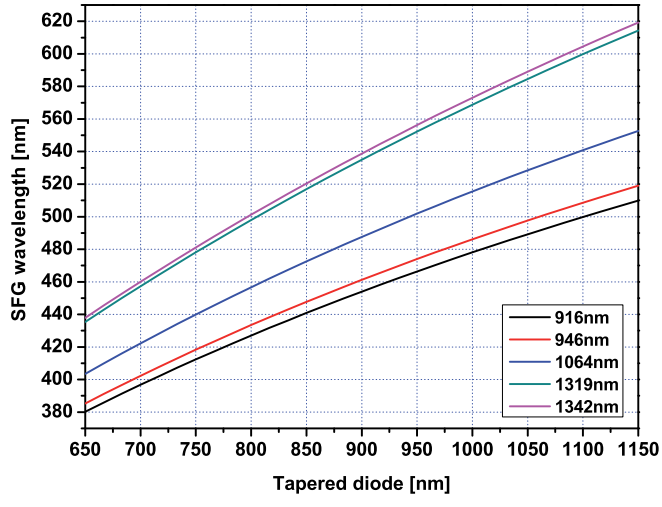

Figure 2.16: The available wavelength through sum frequency generation between the common transition lines in Nd:YVO_4 and Nd:YAG laser crystal and available wavelength for tapered diodes.

2.7 Singly resonant SFG

Intracavity SFG and SHG frequency conversion is known to have amplitude fluctuations (green noise) under multimode operation, this behavior increase with increasing single pass conversion hereby limiting system performance when scaling to high powers [15]. From this point singly resonant configuration are interesting

[3] *Ferdinand Braun Institute, www.fbh-berlin.com*

as there are no coupling between the modal gain in the two lasers and therefore no green noise. However, preliminary theoretical studies suggest that another kind of instabilities arise as the nonlinear coupling is increased. In the present singly resonant configuration simulations predict that for a total optical pump power of 4W, where 2W is used as pump for the intracavity four level laser and 2W is used as single pass power, results in instabilities, for realistic values of laser parameters and nonlinear coupling coefficients see figure 2.17.

First the steady state solution for the circulating and generated power is found by evaluating the loss due to the nonlinear conversion. This is done by calculating the nonlinear loss (L_{NLO}) for the initial circulating power of the resonant field, the nonlinear loss is then used for evaluating a new circulating power and by iteration the steady state circulating power and nonlinear loss is found. Then the circulating power is pertubated by 1%, and the damping coefficient α for the relaxation oscillation is calculated, using the constant nonlinear loss found for the steady state solution (red line) and considering power dependent nonlinear loss (black line) respectively. The relaxation oscillations are approximated by a damping term and a oscillating term given as:

$$P_{circ} = e^{\alpha t} \cdot \sin(\omega_r t) \tag{2.28}$$

Where α is the damping coefficient and ω_r is the oscillation frequency. From this expression it is clear that for positive values of α the oscillation is not damped, and the system becomes unstable. This indicate that at a certain nonlinear coupling strength the steady state value found by standard rate equation becomes a unstable point of operation for the system, for OPO system similar behavior have been observed by Turnbull *et al.* [62]. This is in strong contrast to SHG where it is know that the nonlinear coupling suppress the relaxation oscillations see figure 2.17 (green and blue line). Further experiments are required to confirm this prediction, though observation of instabilities has been seen in experiments conducted prior to this theoretical analysis. These simulations have been published at the EOSAM 2008 conference [63].

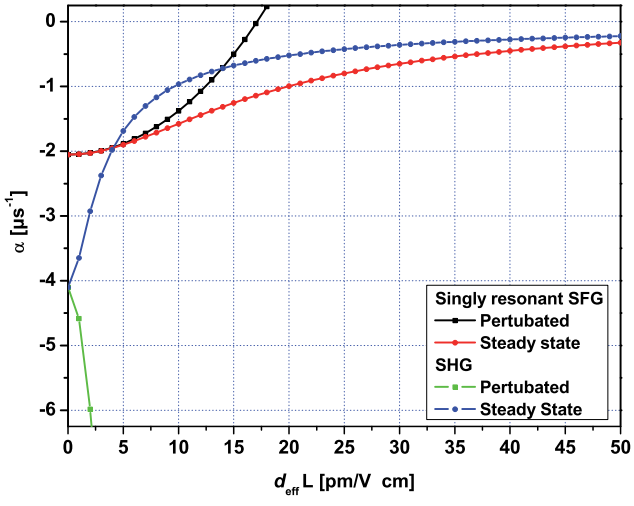

Figure 2.17: Stability for a singly resonant SFG system generating 460nm between a 1342nm laser and a 808nm laser. The 1342nm cavity is pumped by a 2W 808nm pump and 2W single pass power 808nm power is incident on the nonlinear media. (black) the steady state value is perturbated (red) steady state value

Chapter 3

NCPM in GdCOB type crystals

In this chapter the nonlinear properties of three differently co-doped nonlinear optical crystals are presented. Based on measurements using a Continuous Wave (CW) tuneable Ti:Shapphire laser, the effective nonlinear coefficient and temperature acceptance bandwidths are calculated for two Lu and one Sc co-doped $GdCa_4O(BO_3)_3$ type nonlinear crystals. The wavelength for NonCritical PhaseMatching (NCPM) by Second Harmonic Generation (SHG) into the blue-UV spectral region is found by optimising the oscillating wavelength and the angle of incidence on the crystals.

This work has been published in:

- *First measurement of the nonlinear coefficient for $Gd_{1-X}Lu_XCa_4O(BO_3)_3$ and $Gd_{1-X}Sc_XCa_4O(BO_3)_3$ crystals*
  M. T. Andersen, J. L. Mortnsen, S. Germershausen, P. Tidemand-Lichtenberg, P. Buchhave, L. Gheorghe, V. Lupei and L. Pascal and G. Aka.
  Optics Express, Vol. **15**, Issue 8, 4893-4901, April 2007

3.1 Introduction

Nonlinear crystals used for frequency conversion are a key component in visible solid state lasers. New crystals for nonlinear optical frequency conversion, are constantly being developed, as the need for easy generation and high conversion of specific wavelengths require that the properties of the nonlinear materials are carefully controlled. There are many different approaches to achieve optimum phasematching, commonly used techniques are Quasi PhaseMatching (QPM), where parts of the material is inverted in a specific pattern, or changing the propagation direction through the material. Where the QPM technique benefits from freedom of choice regarding propagation direction, the drawback is the trade off on the effective nonlinear coefficient and the small aperture due to the limitation in the fabrication technique, which sets the maximum poling depth to $\approx$ 1-2 millimetres. For birefringent phasematched materials the effective nonlinear coefficient is equal to the material nonlinear coefficient, though since the propagation direction is decided by the phasematching properties of the interaction, it does not necessary exploit the highest nonlinear coefficient found in the material and there may also be other ef-

fects like walkoff, which reduce the conversion efficiency. The aperture is, however, larger than for QPM crystals, making birefringent phasematching the choice for very high power lasers where large beam sizes is essential to avoid damaging the nonlinear crystals. Introducing different co-dopings in the birefringent material alter the birefringence/refractive indices and phasematching can in some cases be achieved along the desired propagation direction in the bulk material, eliminating walkoff thereby achieving NCPM along the direction with the highest nonlinear coefficient. Another problem for bulk phasematching is that for some wavelengths it is impossible to achieve phasematching. In the visible region. Gerard Aka *et al.* [14] reported that a new type of crystal $GdCa_4O(OB_3)_3$ (GdCOB) had nonlinearities comparable to BBO, by gradually exchanging the doping composition of Gd in the COB crystal with Ytrrium (Y) the wavelength, for which NCPM can be achieved, is shifted. The change from pure GdCOB to pure YCOB for SHG Type I phasematch gives a nearly linear change of 120nm from 831nm to 725nm for the NCPM wavelength and from 1255nm to 1032nm for type II phasematching [64]. With these crystals it is possible to eliminate the effect of walkoff by changing the composition.
To investigate the properties of new types of crystals belonging to the ReCOB group, here Re is rare earth material, GdCOB crystal co-doped with (Lu) and Scandium (Sc) is made using the Czochralski method [65].

3.2 Experimental setup

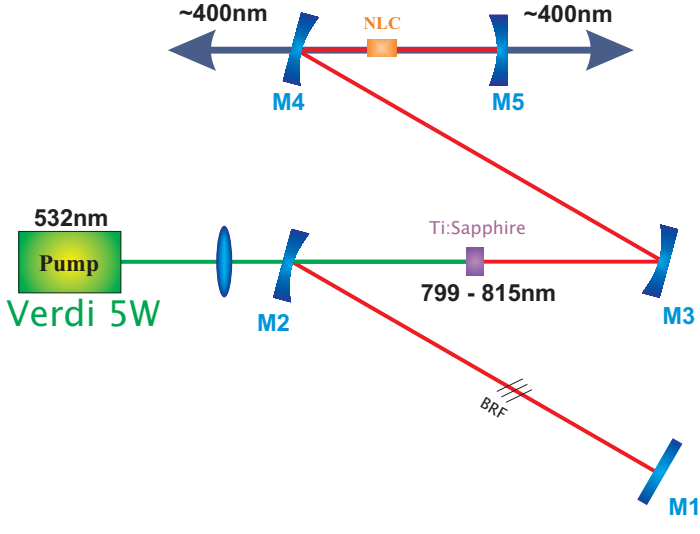

Figure 3.1: Schematic drawing of the Ti:S laser setup: The NLC is placed in the circular beam waist formed between M4 and M5.

For the experiments the setup shown in figure 3.1 is used to perform the characterisation of co-doped nonlinear crystals. The Ti:S laser is pumped with a Verdi V5 laser capable of delivering up to 5.5W at 532nm. The pump is focused by a lens, $f = 100$mm, through mirror M2 into a beam waist of 50μm in the Ti:S laser crystal (LC).

Mirrors M1 - M5 are all high reflecting (HR) for the fundamental NIR wavelength. Mirrors M1 ($r = \infty$)mm, M2 and M3 ($r = -100$mm) are antireflection coated (AR) for the pump wavelength, and mirrors M4 and M5 ($r = -50$mm) are broadband AR coated for the generated blue-UV light.
The distance from M1 to M2 is 200mm, from M2 to M3 113.5mm, from M3 to M4 208mm and from M4 to M5 the distance is 77mm, resulting in a circular beam waist of 23μm between M4 and M5, where the nonlinear crystal (NLC) is inserted. A 3-plate birefringent filter (BRF) inserted between M1 and M2 is used for tuning of the oscillating wavelength.
For the single pass experiment a plane output coupler is inserted in the beam waist between mirror M3 and M4. The output coupler has a transmission of 10 % at the oscillating wavelengths. Figure 3.2 shows a typical spectrum of the Ti:S laser. The FWHM is measured to 31pm at 811.98nm with the Ti:S laser configured for the single pass experiment.

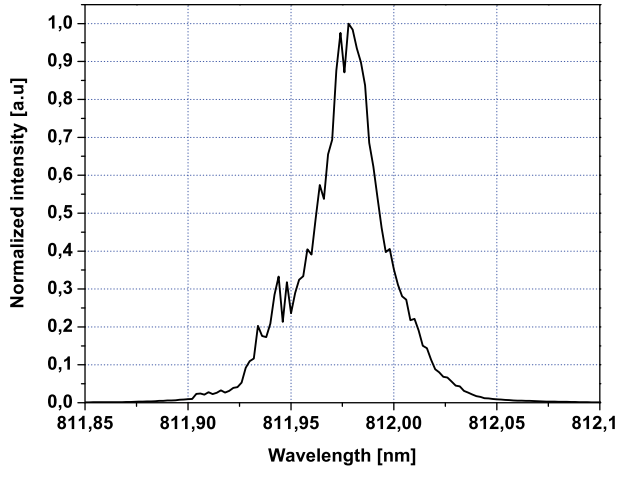

Figure 3.2: Measured spectrum of the Ti:S laser. The FHWM of the spectrum is measured to 31pm centred around 811.98nm.

3.3 Crystal Properties

The crystals used are biaxial, and NCPM occurs when the interacting beams are polarised along the principal axis of the crystal, propagation can be oriented along the **X,Y** or **Z** axis. In table 3.1 the NCPM wavelength for similar crystal with the same concentration of co-dopant are listed [65]. In the current experiment the crystals are oriented for propagation along the **Y** axis and polarised in the **Z** direction. NCPM then occurs around 800nm for the fundamental wavelength of the Ti:S laser generating second harmonic light in the blue-UV region. The measured spectrum of the Ti:S laser shown in figure 3.2 is compared to the calculated data for the

Table 3.1: Calculated and measured NCPM wavelength for SHG and Temperature acceptance bandwidth reported by Gheorghe *et al.* in similar crystals to the ones used in this experiment. The axis given are the direction of propagation (Polarisation of the fundamental). The full width half maximum value for the wavelength are calculated based on the reported sellmeier equation (FWHM)[65].

Crystal Re-COB	**Y**-axis (**Z**) NCPM wavelength Cal./Meas.	**Z**-axis (**Y**) NCPM wavelength Cal./Meas.	FWHM ΔTl [K·cm]	FWHM $\Delta\lambda l$ [nm·cm]
$Gd_{0.871}Lu_{0.129}$-	792.23/792.52nm	921.93/922.36nm	38.8	0.37
$Gd_{0.93}Lu_{0.07}$-	807.73/806.30nm	941.66/938.86nm	38.5	0.40
$Gd_{0.96}Sc_{0.04}$-	802.04/801.32nm	934.35/932.00nm	39.4	0.38

FWHM wavelength acceptance bandwidth shown in table 3.1. It is seen that the measured spectrum from the laser is more than one order of magnitude narrower than the acceptance parameters of the nonlinear crystals, it is therefore appropriate to assume the laser operates at a single frequency when calculating the conversion efficiency of the nonlinear materials. The dimensions of the three crystals are shown at figure 3.3: (left) $Gd_{0.871}Lu_{0.129}Ca_4O(BO_3)_3$, (centre) $Gd_{0.93}Lu_{0.07}Ca_4O(BO_3)_3$ and (right) $Gd_{0.96}Sc_{0.04}Ca_4O(BO_3)_3$. All crystals are AR coated for both the fundamental and the second harmonic wavelengths.

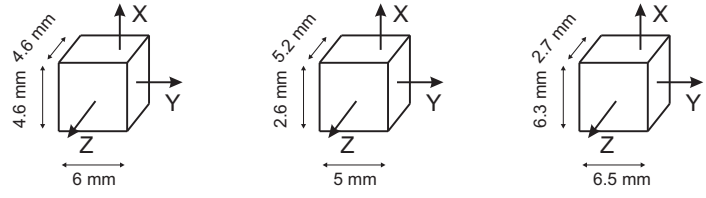

Figure 3.3: The dimensions of the used crystal: (left) $Gd_{0.871}Lu_{0.129}Ca_4O(BO_3)_3$, (centre) $Gd_{0.93}Lu_{0.07}Ca_4O(BO_3)_3$ and (right) $Gd_{0.96}Sc_{0.04}Ca_4O(BO_3)_3$

In the current setup it is not possible to measure the crystals properties for NCPM along the **Z** axis and polarised in the **Y** direction, since laser action of the Ti:S laser was limited by the coating of the mirrors (680-880nm).

3.4 NCPM and ΔTl

First the phasematching wavelength and temperature acceptance bandwidth (ΔTl) are measured for the NLCs. This is done in the single pass configuration. The output of the Ti:S laser is focused into the NLC. The output power of the Ti:S is measured to be approximately 700mW during the single pass measurements on the three crystals.

The $Gd_{0.871}Lu_{0.129}Ca_4O(BO_3)_3$ crystal is mounted in a temperature controlled oven and adjusted to 40 °C, and the fundamental wavelength of the Ti:S laser is optimized for maximum blue light generation by adjusting the BRF. For this crystal the optimum fundamental wavelength is found to 799.0nm, as oppose to the calculated 792nm found in table 1. This, however, is calculated at 25 °C. In order to see

if the difference could be due to the elevated temperature of the NLC, a temperature scan is performed while monitoring the conversion efficiency. This measurement is shown in figure 3.4.

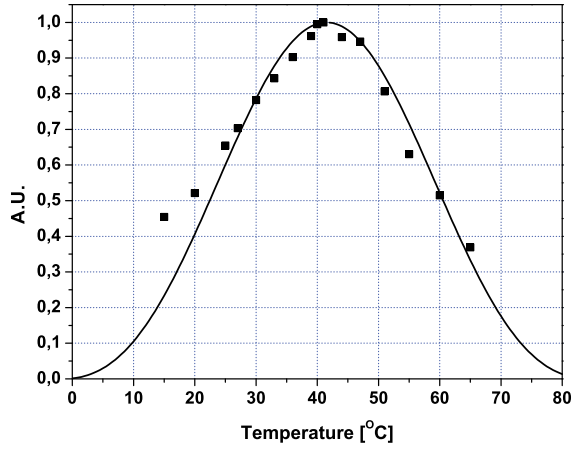

Figure 3.4: Temperature acceptance bandwidth for the $Gd_{0.871}Lu_{0.129}Ca_4O(BO_3)_3$ crystal measured at a fundamental wavelength of 799nm. The optimum temperature is found to $41.5 \pm 1\,^{\circ}C$, and the FWHM temperature bandwidth is measured to $38.1\,^{\circ}C$ for the 6mm long crystal.

To the author's knowledge no temperature dependent Sellmeier equations has been published for these materials. Similar measurements are shown on figure 3.5 for the two other NLCs. These measurements are obtained using a fundamental wavelength of 812.0nm and 814.8nm respectively. It should be noted that the lengths of these crystal are not identical.

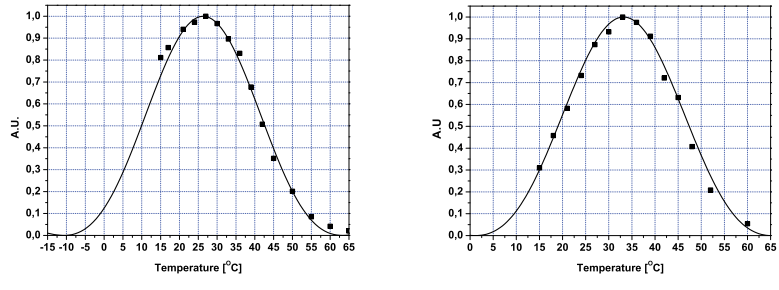

(a) **(b)**

Figure 3.5: Measured temperature acceptance bandwidth and temperature dependence for: (a) $Gd_{0.93}Lu_{0.07}Ca_4O(BO_3)_3$ at a fundamental wavelength of 812.0nm. (b) $Gd_{0.96}Sc_{0.04}Ca_4O(BO_3)_3$ at a fundamental wavelength of 814.8nm.

The centre temperature for the three crystals is seen to vary, though due to modehop of the Ti:S laser it is necessary to adjust the temperature together with the fundamental wavelength. It is seen that the values of the phasematching wavelengths measured are slightly different from the calculated values, especially in the case of the $Gd_{0.96}Sc_{0.04}Ca_4O(BO_3)_3$ crystal where the greatest deviation of 12.8nm is obtained. As a consequence, the deviations cannot be explained by the temperature alone. It is known that a minor change of the compositional parameter x can lead to a relatively large change in the phasematching wavelength. Thus one possible explanation of the obtained differences could be the presence of small nonuniformities in the composition of the grown crystals. The small values of the segregation coefficient of the Sc ions in the $GdCa_4O(BO_3)_3$ crystals ($k = 0.38$) [65], could explain the relative large deviation obtained for the $Gd_{0.96}Sc_{0.04}Ca_4O(BO_3)_3$ crystal. The temperature acceptance bandwidth are also seen to deviate with up to 22.2K·cm from the one found in [65] and shown in table 3.1. The measured parameters of the three crystals are summarised in table 3.2 where the measured temperature acceptance bandwidth are given in ΔTl [K·cm].

Table 3.2: Measured and calculated NCPM fundamental wavelength and FWHM temperature acceptance bandwidth of the used nonlinear materials.

Nonlinear crystal	**Y**-axis (**Z**) NCPM wavelength calculated / measured	Temperature centre / FWHM T [°C] / ΔTl [K·cm]
$Gd_{0.871}Lu_{0.129}Ca_4O(BO_3)_3$	792.23nm / 799.0nm	41.5 / 22.9
$Gd_{0.93}Lu_{0.07}Ca_4O(BO_3)_3$	807.73nm / 812.0nm	26.3 / 16.3
$Gd_{0.96}Sc_{0.04}Ca_4O(BO_3)_3$	802.04nm / 814nm	33.2 / 18.5

3.5 Blue light generation

The $Gd_{0.871}Lu_{0.129}Ca_4O(BO_3)_3$ crystal is then placed intracavity in the Ti:S laser as shown on figure 3.1 and temperature stabilised at the optimum phasematch temperature. The crystal is again orientated for beam propagation along the **Y**-axis and the fundamental field polarised in the **Z**-direction. The generated power is measured as function of pump power, see figure 3.6 (a). More than 37mW of Blue-UV light is measured through mirror M5 and a equally amount of light is observed though mirror M4. To measure the circulating power, which is essential for calculating the effective nonlinear coefficient, it is necessary to exchange one of the very highly reflecting mirrors with a 1% output coupler (M1). In this way it is possible to measure the generated second harmonic power as a function of fundamental power squared, see figure 3.6 (b). It is seen, that a linear relation exists between the square of the fundamental power and the generated second harmonic power as expected. This relation will be used for calculation of the effective nonlinear coefficient of the material in the following section. A similar experiment is made using the two differently co-doped crystals, and the results of these measurements are shown in figure 3.7 and 3.8. Comparing the graphs in figure 3.6, 3.7 and 3.8 (a), it is seen that the $Gd_{0.93}Lu_{0.07}Ca_4O(BO_3)_3$ crystal has a much higher threshold than the other two

crystals. When optimizing for blue-UV light generation, the pump power is set at its maximum (5.5W).

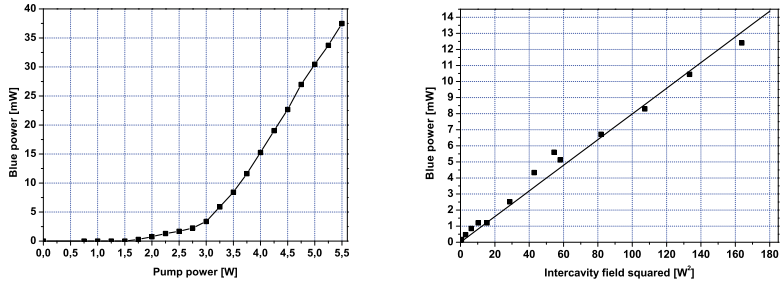

(a) **(b)**

Figure 3.6: Generated intracavity 399.50nm light propagating through mirror M5 for the $Gd_{0.871}Lu_{0.129}Ca_4O(BO_3)_3$ crystal. (a) As function of pump power in a high finesse cavity. (b) as function of the intracavity field squared with a 1% output coupler.

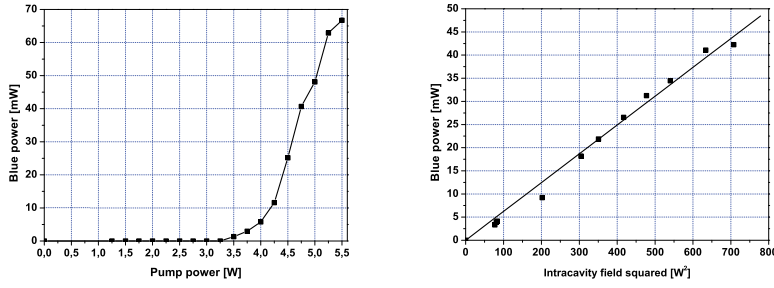

(a) **(b)**

Figure 3.7: Generated intracavity 405.60nm light propagating through mirror M5 for the $Gd_{0.93}Lu_{0.07}Ca_4O(BO_3)_3$ crystal. (a) As function of pump power in a high finesse cavity. (b) as function of the intercavity field squared with a 1% output coupler.

As the Ti:S laser shown in figure 3.1 has a very small stability range, the laser is not stable before a certain thermal lensing is present in the Ti:S crystal, since the crystals have different lengths the stability zone is shifted due to the change in the optical length, this cause a change in the thermal lensing needed to reach threshold. The setup is optimised for highest generation of blue-UV power, and not for lowest threshold. At figure 3.6 (b) the circulating power for the $Gd_{0.871}Lu_{0.129}Ca_4O(BO_3)_3$ crystal is very low compared to the two other crystals shown in figure 3.7 (b) and 3.8 (b).Making a closer examination of this crystal in a microscope, small impurities could be seen, which is believed to give rise to higher scattering losses.

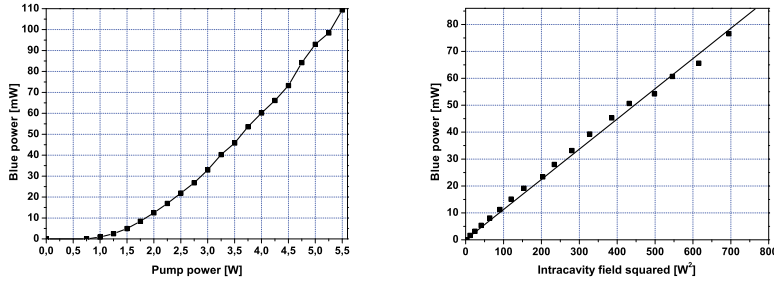

(a) **(b)**

Figure 3.8: Generated intracavity 407.40nm light propagating through mirror M5 for the $Gd_{0.96}Sc_{0.004}Ca_4O(BO_3)_3$ crystal. (a) As function of pump power in a high finesse cavity. (b) as function of the intracavity field squared with a 1% output coupler.

3.6 Calculating the nonlinear coefficient

From the above measurement the effective nonlinear coefficient, d_{eff}, can be calculated using equation 3.1 [40].

$$d_{eff} = \sqrt{\frac{P_{2\omega}}{P_{\omega}^2} \cdot \frac{\pi n_1^2 n_2 \epsilon_0 c^3}{2\omega^2 L k_\omega h_m}} \tag{3.1}$$

where P_ω is the fundamental power, $P_{2\omega}$ is the generated power, n_1 and n_2 are the refractive indices for the fundamental and the generated light respectively. L is the length of the crystal, k_ω is the wavevector of the fundamental wave in the media, ϵ_0 is the permittivity of free space, c is the speed of light, ω is the frequency of the fundamental and h_m is the Boyd Kleinman factor defined in [40]. This factor is estimated based on simulations done for the setup shown at figure 3.1. The calculation is strait forward, given the values listed in table 3.3.

Table 3.3: Summary of the parameters used for calculation of the effective nonlinear coefficients of the nonlinear materials

	$Gd_{0.871}Lu_{0.129}$	$Gd_{0.93}Lu_{0.07}$	$Gd_{0.96}Sc_{0.04}$	unit
w_0	23	23	23	μm
λ	799.00	812.00	814.80	nm
L	6.0	5.0	6.5	mm
h_m	0.66	0.58	0.71	
P_1	12.8	26.6	26.4	W
P_2	12.4	41.9	76.6	mW
d_{eff}	0.78	0.81	0.89	pm/V

It is seen that the nonlinear coefficients for these crystal is slightly higher than for LBO. With the ability to dope pure $GdCa_4O(BO_3)_3$ crystals with either Lutetium (Lu) or Scandium (Sc) and thereby achieve NCPM for any fixed wavelength, makes

these crystals very attractive in applications where a specific wavelength is required. The co-doping with either Lu or Sc however seems to reduce the effective nonlinear coefficient as the concentration of Gd is reduced, In table 3.4 the properties of the different rare earth doped COB crystal are compared and here the effective nonlinear coefficient of pure GdCOB crystal is found to be 1.3 which fits well with the obtained results that pure GdCOB crystal exhibits a stronger nonlinear response compared to the co-doped versions. The properties for propagation along the **X** axis are not shown, and are only theoretically reported for YCOB and GdCOB [64].

Table 3.4: Comparison of the nonlinear characteristics for rare earth doped COB crystals for non critical second harmonic generation. Numbers in parentheses are calculated values.

Crystal Re-COB	axis	d_{eff} [pm/V]	Type I [nm]	Type II [nm]	Temp. [K·cm]	ref.
$Gd_{0.871}Lu_{0.129}$-	**Y**	0.78	799	(1159.2)	22.9	
	Z		922.36	(1680.6)		[65]
$Gd_{0.93}Lu_{0.07}$-	**Y**	0.81	812	(1189.2/2448)	16.3	
	Z		932	(1618.8/1916)		[65]
$Gd_{0.96}Sc_{0.04}$-	**Y**	0.89	814.8	(1170.5/2511.8)	18.5	
	Z		938.86	(1505.3/2136.3)		[65]
Gd-	**Y**	1.3	831	1255	38	[47, 64]
	Z		973	(1557)		[64]
Y-	**Y**	1.1, 0.52	725	1032	65	[47, 64]
	Z		826	(1218)		[64]

3.7 Conclusion

The nonlinear coefficients for SHG of NIR light for three differently co-doped Gd-COB crystals have been measured. The light is propagating along the **Y** axis with the fundamental polarised along the **Z** direction. For $Gd_{0.871}Lu_{0.129}$ the nonlinear coefficient is found to be 0.78pm/V at a fundamental wavelength of 799nm. The temperature dependence acceptance bandwidth of the phasematching is measured to have a FWHM of 22.9K·cm. For $Gd_{0.93}Lu_{0.07}$ the nonlinear coefficient is calculated to 0.81pm/V for a fundamental wavelength of 812nm, and the temperature dependent FWHM acceptance temperature is measured to 16.3K·cm. The third crystal is $Gd_{0.96}Sc_{0.04}$ for which a nonlinear coefficient of 0.89pm/V is found by second harmonic generation of 815nm and the temperature dependent FWHM is measured to 18.5K·cm.

A total of 115mW of CW power at 407nm is generated in one direction using the 6.5mm long $Gd_{0.96}Sc_{0.04}$ crystal. Using NCPM it should be possible to scale this system further, both using a longer crystal and by increasing pump power. No signs of degradation of the NLCs have been seen throughout the experiments. The nonlinear coefficients are seen to be comparable to the value found for LBO ($d_{eff} = 0.75pm/V$), and the ability to obtain NCPM at a large range of wavelengths

makes this a promising candidate for nonlinear frequency conversion into the blue-UV spectral range for a number of applications.

3.8 Errata

The equation used in the ref [66] contains an error which unfortunately gives another estimate of the effective nonlinear coefficient for the three crystals. The values in the article are ≈ 0.5pm/V compared to the ones reported here of ≈ 0.8pm/V. The error origin from the textbook used for the calculation. The presented values and calculations in this chapter are based on the original article by G. D. Boyd and D. A. Kleinman [40]

Chapter 4

Nonlinear Cavity Dumping

In this chapter a novel generic approach for pulsed light generation in the visible spectrum is presented. The fundamental idea is that the high circulating intracavity power of an efficient IR laser can be cavity dumped through nonlinear frequency conversion into the visible spectrum as a high peak power pulse from a second laser is single passed through an intracavity nonlinear medium. The nonlinear induced loss by sum frequency mixing is proportional to the peak power of the single pass pulses. Therefore, the nonlinear loss is zero between the pulses, but in the presence of an injected pulse the nonlinear conversion can be highly efficient, thus essentially dumping the entire circulating intracavity field. In this realisation the experimental setup consists of a high finesse 1342nm Nd:YVO_4 laser cavity and a passively Q-switched 1064nm Nd:YAG laser. Periodically poled KTP is used as the nonlinear medium. Nonlinear cavity dumping of the 1342nm laser through nonlinear conversion to yellow 593nm pulses are realised.

This work has been published in:

- *Nonlinear cavity dumping of a high finesse frequency mixing module*
  P. Tidemand-Lichtenberg, **M. T. Andersen**, S. Johansson, C. Canalias, F. Laurell, P. Buchhave, E. Karamehmedovic and C. Pedersen.
  Optics Express, Vol. **15**, Issue 15, 9799-9803 (2007).

- *Generation of pulsed light in the visible spectral region based on non-linear cavity dumping*
  S. Johansson, **M. T. Andersen**, P. Tidemand-Lichtenberg, J. Janousek, P. Buchhave and F. Laurell.
  Northern Optics 2006, T36, (Poster), 2006

- *Pulsed, all solid-state light source in the visible spectral region based on non-linear cavity dumping*
  P. Tidemand-Lichtenberg, **M. T. Andersen**, S. Johansson, J. Janousek, P. Buchhave and F. Laurell.
  ASSP 2006, TuB19, (Poster, abstract), January 2006

4.1 Introduction

Lasers in the visible spectrum have over the past decade found an increasing number of applications, e.g. within the healthcare industry, for spectroscopy and imag-

ing use. Many wavelengths in the visible spectrum can be reached through second harmonic generation of efficient solid state lasers both in Continuous Wave (CW) and pulsed operation. In the CW regime efficient light sources based on sum frequency mixing have been demonstrated [17, 67, 68] using various power enhancement schemes. In the pulsed regime sum frequency mixing of synchronised Q-switched pulses has been demonstrated [69, 70]. Raman shifted pulsed lasers based either on solid state [71] or fibre lasers [72] has also been realised. Alternatively cascaded nonlinear frequency conversion of Qswitched lasers has been used for the generation of pulsed light in the visible and UV spectrum [73, 74].
In this chapter, a novel generic approach for generation of pulsed light in the visible spectrum based on sum frequency mixing of the circulating intracavity power of a high finesse CW laser and a single pass Q-switched laser is demonstrated.
In the following one possible realisation of the system, based on SFG between a high finesse folded cavity 1342nm Nd:YVO_4 laser and a passively Q-switched 1064nm Nd:YAG laser using periodically poled KTP is presented.

4.2 Nonlinear cavity dumping

The usual setup for cavity dumping the circulating field of a resonator is based on the use of an active component such as an Acoustic Optic Modulator (AOM) [75] or a pocklet cell in combination with a polarising beamsplitter [76]. In the first case the AOM is used to missalign the cavity and the stored circulating field is coupled out by this misalignment. In the second case the polarisation of the circulating field is rotated by applying an electric field over the pocklet cell, and the beam is coupled out through a polarising beamsplitter. In both cases the cavity dumping require active control and fast electronics capable of operating at timescales much shorter than the cavity roundtrip time. SFG between two pulsed lasers usually require some means of synchronising the pulses The advantage of the proposed system is that in contrary to the methods of SFG between two pulsed laser which usually require some means of synchronising the pulses, no synchronisation or fast electronics are needed since one of the lasers is operated as a CW laser. The pulsed laser can be realised either as a passive or active Q-switched system. The duration of the SFG pulses is controlled by the pulse duration of the Q-switched laser or ultimately by the cavity round trip time of the CW laser, provided that the nonlinear coupling is sufficiently strong to dump the entire circulating intracavity field within a single pass of the NLC. It should be noted, however, that the generated peak power in the visible is limited by the circulating power of the CW operated laser multiplied by the photon energy ratio.

4.2.1 System limitations

There are two limiting factors in this scheme. The circulating field is usually at least one order of magnitude smaller than the pulsed single pass laser. Therefore the peak power of the frequency converted beam is limited by the circulating power times the photon energy ratio. The maximum energy in each pulse is limited by the power stored in the CW laser cavity.

$$E_{SFG} = \tau_{rt} \cdot P_c \cdot \eta_{ratio} \tag{4.1}$$

where $\tau_{rt} = (2 \cdot l_{cav})/c$ is the roundtrip time of the cavity, l_{cav} is the length of the cavity and $\eta_{ratio} = \lambda_{cav}/\lambda_{SFG}$. In order to increase the peak power or the energy in the generated beam it is necessary to increase the circulating power or the cavity length respectively.

4.2.2 Saturation

As a consequence of these limitations the SFG field experience two types of saturation. These saturation effects are a function of the peak power and pulse length of the single pass laser. If the pulse length is shorter than the round trip length l_{rt} not all the power stored in the cavity is dumped regardless of the peak power of the pulsed laser. An increase of the pulse length will increase both the pulse length and the pulse energy of the generated beam. On the other hand pulses much longer than the roundtrip length of the cavity does not increase the pulse length or pulse energy since no frequency conversion occur when the whole circulating field is dumped. This is the case when the peak power is sufficiently strong to dump the whole circulating power in a single pass in one go. If the peak power of the single pass laser is so small that the circulating power of the cavity is not completely dumped in a single pass, the generated beam experience lower peak power than actually achievable and the pulse length will depend on both the length of the single pass pulse and the residual circulating field. It is clear that the amount of peak power necessary to dump the circulating field of the cavity depend on the coupling efficiency between the circulating field and the pulsed laser, furthermore the mode overlap between the two mixing lasers changes the coupling efficiency, therefore the saturation point depend on the actual setup.

4.2.3 Passive losses

When a laser cavity is pertubated for example by changing the pump power, or in this scheme by introduce a loss due to the mixing in the nonlinear crystal, the circulating field changes. After the pulse passes the nonlinear media the conversion due to the nonlinear interaction returns to zero and the intracavity field relaxes towards the previous steady state value for the circulating field. The steady state value is reached by relaxation oscillation governed by the rate equations. These oscillation depend of the pump power and the loss mechanism in the cavity, and by examine the characteristic frequency and damp rate of this oscillation the passive losses of the cavity can be roughly estimated. This is another method for determine the passive losses compared to the methods described in chapter 6.

4.2.4 Backconversion

When at least one of the interacting waves are sufficiently strong backconversion of the wanted process can occur. Since the conversion efficiency is proportional to the field strength, the used interaction length has to be adapted to the power level in order to avoid this reversal of the process. This is a consequence of the reversible nature of the three wave interaction described in detail by Amrstrong *et al.* [45], meaning that a nonlinear media phasematched for SFG works equally well for the opposite process DFG upon a change in the relative phase. In the CW case the phenomena can be examined directly by plotting the generated power as function of the incoming power of the fundamental. When the nonlinear media is placed

intracavity the dynamic is more complicated. For the experimental setup described in this chapter the roundtrip time of the 1342nm cavity also plays a vital role, and for pulses longer than the roundtrip time of the resonator, parts of the pulse will experience a decrease in the circulating field after one roundtrip time. Therefore in order to experience backconversion in the present setup the raise time of the single pass pulse should be sufficient to reach the power level needed for backconversion in less than the roundtrip time.

4.3 Setup

The setup consists of a folded cavity 1342nm laser with an intracavity periodically poled KTP crystal, and a single pass Q switched Nd:YAG laser, as shown in figure 4.1.

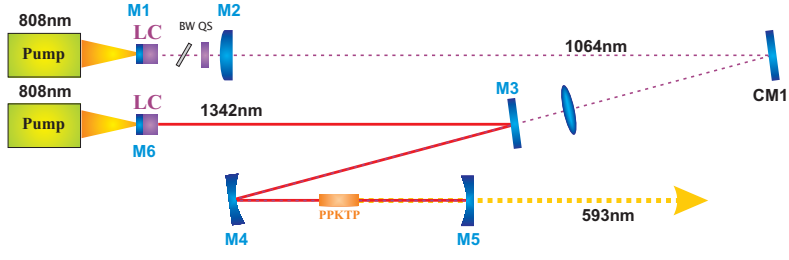

Figure 4.1: Schematic setup of the suggested generic approach for generation of visible laser pulses.

The 1342nm laser comprises a 8x3x3mm^3 Nd:YVO_4 crystal with a Nd doping of 0.5atm%, a coupling mirror M3 (planar), a mirror M4 ($r = -100$mm) and a end mirror M5 ($r = -50$mm). Mirrors M3, M4 and M5 and the left end facet of the laser crystal M6 is coated for high reflection at 1342nm, thereby forming a high finesse cavity. The Q-switched 1064nm laser consists of a 5mm long Ø 3mm Nd:YAG crystal (1.0atm%), a Brewster Window (BW), for polarisation control, a Cr:YAG saturable absorber, QS, acting as passive Q-switch and an output coupling mirror, M2 ($r = 500$mm, R= 84%@1064nm). The left end facet of the Nd:YAG crystal, M1, and the output mirror form an unstable cavity, however, supporting a stable Gaussian mode when sufficient thermal lensing is induced in the Nd:YAG crystal by the pump diode. Two different saturable absorbing crystals having a small signal transmission of 80% and 90%, respectively are used. The mirrors M3 and M5 are coated for high transmission at 1064nm, whereas the steering mirror CM1 and the folding mirror M4 are coated for high reflection at 1064nm. Lens, L, is used for mode matching of the two lasers in the nonlinear crystal. Both beam waist radii are approximately 40μm. The nonlinear material used in this setup is a 20mm long PP:KTP, with a QPM period of 12.65μm. Both lasers are pumped by 4W@808nm Broad Area Laser(BAL) diodes.

4.4 Simulations

In order to investigate the dynamic of the shown system, simulations are carried out in MatLab, and the code can be found in appendix A.1 and A.2. For all the

simulations the pump power for both lasers are kept constant at $P_{808} = 3.5W$. When the optical field of the 1342nm cavity is dumped through the interaction with the single pass pulse in the PPKTP, the optical field will return to the steady state circulating field through relaxation oscillation. Since the relaxation time of the intracavity field takes place on a much longer timescale (μs) than the nonlinear interaction (ns), the depletion of the circulating field is simulated to take place instantaneously by setting the photon density to '0'. The values for the passive losses are kept to a realistic value of 1.4% giving a cavity lifetime of $\approx$ 213ns and the stimulated emission cross section $\sigma_{1342} = 6.0 \cdot 10^{-23}\mathrm{m}^2$ [77]. The beam waist of the pump in the Nd:YVO_4 is set to $W_{pump} = 350\mu$m and the 1342nm waist is found using ABCD matrices to $W_{1342} \approx 190\mu$m. The absorption of the Nd:YVO_4 is set to 58% of the total pump power. With these values the intracavity field is calculated to $P_{circ} \approx 50$W. On figure 4.2 (a) the relaxation can be seen for the 1342nm field. When the 1342nm field is changed to '0' the population of the upper state laser level increases as shown on figure 4.2 (b), and the oscillation relaxes to the steady state value after $\approx 70\mu$s. It is seen that the circulating field peaks at around 6.5 times the steady state circulating field corresponding to 325W.

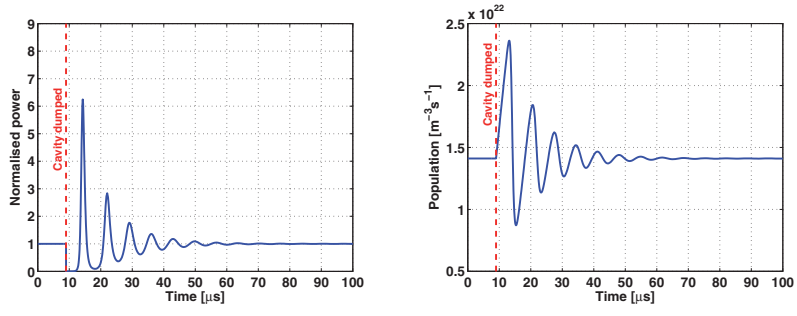

Figure 4.2: (a) Relaxation oscillations of the optical circulating field as function of time for a setup similar to the experimental setup. The steady state circulating field is normalised to 1.(b) Relaxation oscillation for the upper state laser level as function of time. The red dotted line indicates dumping of the optical circulating field

To investigate the possibility for backconversion, the SFG process is simulated in a configuration where both lasers are single passed and the singly resonant setup similar to the one used in this experiment. The plane wave approximation is used, and the steady state circulating field of the 1342nm cavity of 50W is used. A nonlinear coefficient of $d = 15pm/V$ is used giving a effective coefficient of $d_{eff} = 2/\pi \cdot d \approx 9.5$ for the 20mm long PPKTP and the duration of the 1064nm pulse is fixed to 7ns, the roundtrip length is $\approx$ 900mm giving a roundtrip time of $\approx$ 3ns. On figure 4.3 the resulting normalised powers as function of time are plotted for a incident 1064nm pulse of 6W peak power, (a) a double single pass and (b) for the singly resonant setup. The SFG wave is close to identical to the single pass pulse with the same duration for the two cases and the only major difference is the drop of the circulating field in the singly resonant case. Since the peak power of the 1064nm pulse is relatively low no backconversion is observed. When the 1064nm pulse is increased to 600W the difference between the two cases is more clear.

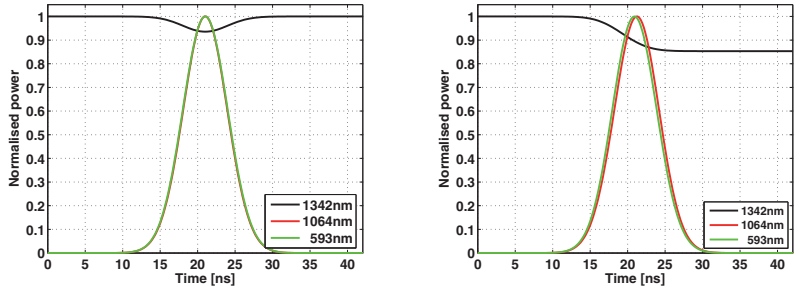

Figure 4.3: Normalised powers for the three interacting waves for a incident 1064nm pulse of 6W peak power, and 50W of 1342nm power incident on the PPKTP. (a) double single pass simulation. (b) singly resonant simulation. The roundtrip time of the 1342nm cavity is $\approx$ 3ns.

On figure 4.4 (a) the double single pass shows that the generated pulse is fragmented due to backconversion as the power of the 1064nm is increased towards the peak power of 600W. The plot is also symmetrical with respect to the peak of the 1064nm pulse which is expected. On figure 4.4 (b) backconversion also occur though because the 1342nm light is resonant, the circulating power is decreased from conversion with the front of the 1064nm pulse and the result is a decrease in the peak power of the resultant 593nm spikes. The SFG wave is also seen to have a shorter duration in time compared to the peak of the single pass pulse.

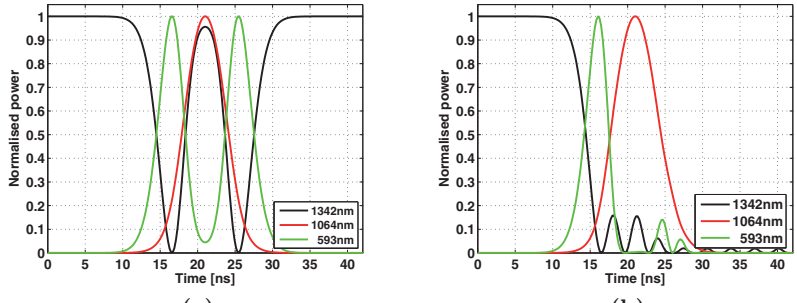

Figure 4.4: Normalised powers for the three interacting waves for a incident 1064nm pulse of 600W peak power, and 50W of 1342nm power. (a) double single pass simulation. (b) singly resonant simulation.

It is clear from the simulations that the shape of the generated 593nm pulse is not necessary identical to the input pulse and the FWHM of the pulse is not constant but depend on the relative power between the CW 1342nm and the 1064nm pulse. An increase in the peak power for the single pass laser will lead to saturation of the peak power and pulse energy. On figure 4.5 (a) the total energy of the generated 593nm pulse is plotted as function of the 1064nm peak power. and on 4.5 (b) the peak power of the generated 593nm pulse. Both plots are plotted for different

coupling efficiency between the interacting fields, where this coupling efficiency is introduced as a factor in each of the three equations 2.14.

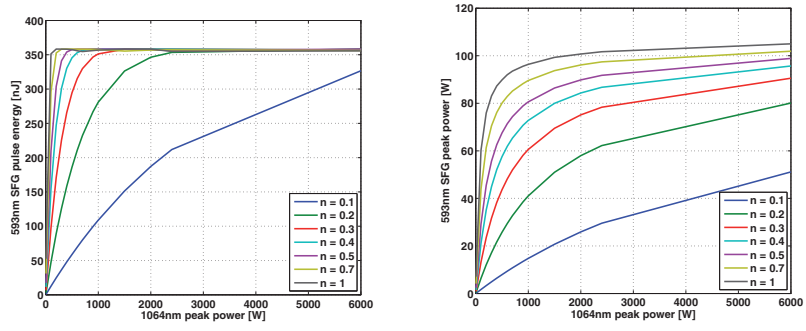

(a) (b)

Figure 4.5: (a) energy saturation of the SFG 593nm pulse. (b) peak power saturation of the 593nm pulse. n indicate the coupling efficiency, for peak pulses above 2000W the cavity is dumped even for a low coupling efficiency, whereas the peak power is lowered substantially as the coupling is degraded.

4.5 Measurements

First the performance of the Q-switched 1064nm laser is evaluated. Experimental data of the repetition rate as a function of pump power are shown in figure 4.6. As expected, the repetition rate increases as a function of the pump power. The saturation effect seen in the measured power is due to changing beam parameters caused by increased thermal lensing in the Nd:YAG crystal. The transverse intensity distribution is, however, Gaussian at all pump power levels. The FWHM pulse duration is almost constant at 7ns for all pump power levels, this corresponds to ≈ 2.3 roundtrip lengths of the 1342nm cavity. The peak power remained constant at approximately 10kW independent of the pump power, when using the 80% Cr:YAG saturable absorber. An intracavity circulating power of approx. 50W is obtained for the 1342nm laser in the absence of 1064nm pulses. It is known from CW experiments, that a conversion efficiency of more than 1%/W·cm can be obtained [17]. The nonlinear conversion of the 1342nm intracavity field into the generated 593nm, scales linearly with the peak power of the single pass laser. Thus even modest peak power of the single pass Q-switched laser will be sufficient to dump the circulating field of the 1342nm laser. The result is a visible light pulse with a duration corresponding to one or a few roundtrip times of the high finesse cavity. Part (a) of figure 4.7 shows a measurement of the circulating power of the 1342nm laser through mirror M4 when a Q-switched 1064nm pulse is single passed through the intracavity nonlinear material. It is clearly seen that the circulating 1342nm power is effectively dumped by the 1064nm pulse. The graph also shows the characteristic relaxation oscillations of the 1342nm laser as the circulating field returns to its steady state value.

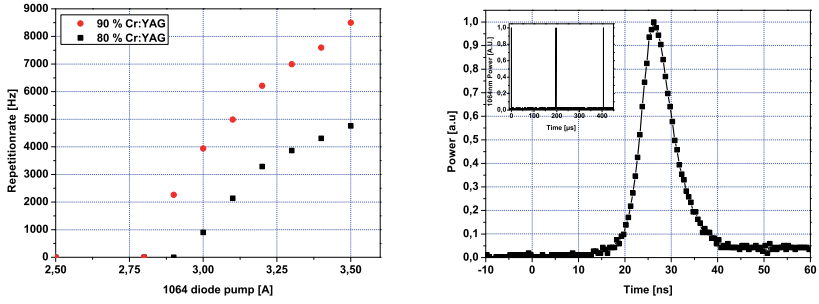

(a) (b)

Figure 4.6: Measured operation of the Q-switched 1064nm laser. Figure (a) shows the pulse repetition rate as a function of diode pump current. Figure (b) shows a typical trace of a single pulse and multiple pulses at a diode pump current of 3.5A, using the 80% Cr:YAG saturable absorber.

Figure 4.7 (b) shows the average yellow power as a function of diode pump current of the 1064nm laser. Note, however, the average power has by no means been optimized in the present setup. Comparing figure 4.7 (b) to figure 4.6 (a), it is clearly observed that the average visible power scales directly with the repetition rate of the Q-switched pulses.

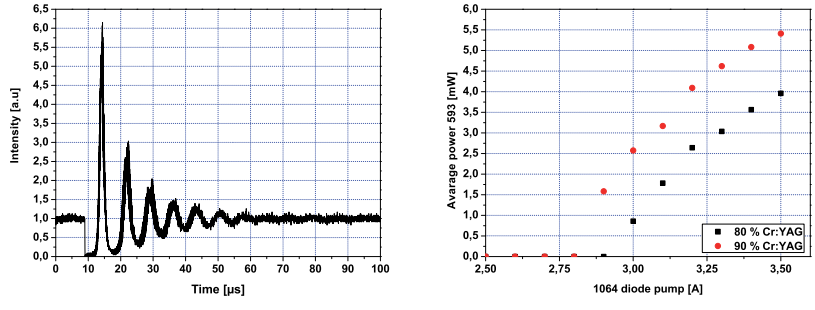

(a) (b)

Figure 4.7: (a) Measured power from the 1342nm laser when a high peak power 1064nm pulse is single passed through the intracavity nonlinear material. (b) Average yellow power as a function of diode pump current for the 1064nm laser.

Looking closer at the time evolution of the three interacting fields, figure 4.8 shows normalised power levels for the three interacting wavelengths. In figure (a) the 1064nm pulses have been attenuated to a peak power of approx. 6W, resulting in a modest decrease in the circulating 1342nm power, as indicated by the black curve. When the peak power of the Q-switched 1064nm laser is increased, the cavity dumping of the circulating 1342nm power is seen to be increasingly efficient. In figure 4.8 (b) it is even seen that all the 1342nm power is dumped in the form of a visible pulse before the tailing edge of the 1064nm pulse has passed the nonlinear

medium. Thus the peak power at 593nm is reached before the peak power of the 1064nm pulse is reached.

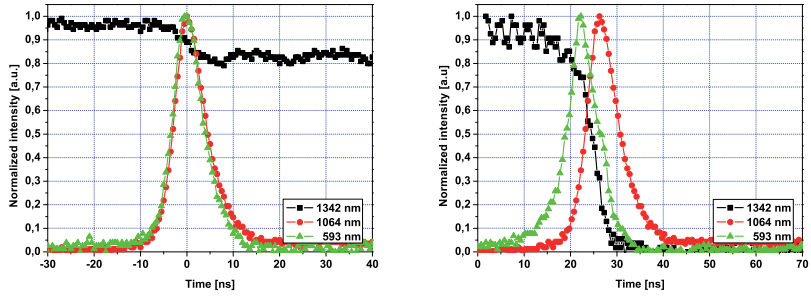

Figure 4.8: Measured power of the three interacting fields at 1342nm (Black curve), 1064nm (Red curve) and 593nm (Green curve). (a) The 1064nm laser has been attenuated to 6W of peak power. (b) the 1064nm laser at the position of the nonlinear crystal is attenuated to 2.4kW

The measurements shown in figure 4.8 and 4.9 were obtained using reflection type ND filters to attenuate the 1064nm peak power, without changing the mode overlap in the nonlinear crystal. Increasing the peak power of the 1064nm laser is seen to enhance this phenomenon further. However, this increase of the 1064nm peak power does not result in increased 593nm peak power as seen in figure 4.9 (b). In fact, both peak power as well as average power of the generated visible light saturates completely after a certain peak power level of the 1064nm laser is reached. This level corresponds to the point where all the circulating 1342nm power has been converted into a 593nm pulse, i.e. coupled out of the cavity. The only way to increase the visible average power further is by increasing the circulating power of the CW laser or increasing the repetition rate of the single pass laser. The peak power necessary to reach the saturation point depends on the beam size, the mode overlap in the nonlinear crystal and the effective nonlinearity of the nonlinear material. Figure 4.9(b) shows that the saturation point in the present configuration is reached at a peak power level of less than 1kW. At very high peak power it is expected that some backconversion would occur, but this is not observed, all parameters is kept constant when changing the attenuation of the 1064nm laser. The 1342nm is completely dumped and there is not observed any backconverted 1342nm light. Since backconversion only happens in the perfect phasematch case it is believed that the linewidth of the 1342nm laser, which is usually around 0.2-0.4nm, is enough to keep the system from initiating the backconversion from starting as it require a π phaseshift to be associated with the 1342nm wave or the residual 1342nm modes acts destructively in initiating the process.

4.5.1 Parameter estimation

By fitting the relaxation oscillation to the measured time evolution the total passive losses of the cavity can be estimated (Scattering, output coupling and other loss mechanism). On figure 4.10 the measured relaxation oscillation is overlapped with the simulated oscillation, it is seen that the used values for the simulation fits

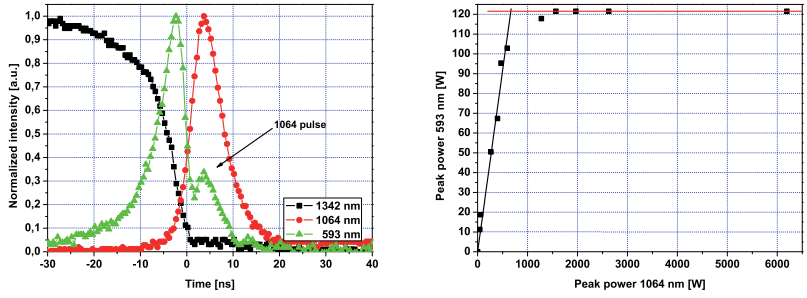

Figure 4.9: Measured power of the three interacting fields at 1342nm (Black curve), 1064nm (Red curve) and 593nm (Green curve) at a 1064nm peak power of 6kW (a). The secondary peak on the green trace is residual 1064nm pulse reaching the detector for the yellow light. (b) Saturation of the 593nm peak power as a function of 1064nm peak power.

very well with the measured, and the passive losses can be estimated to around $L_p \approx 1.5\%$. From the measurement of the time evolution for the three interacting fields and the saturation the efficiency of the coupling can be estimated. The relaxation simulation indicate that the mode matching is close to unity meaning that for example the mode overlap is close to optimum.

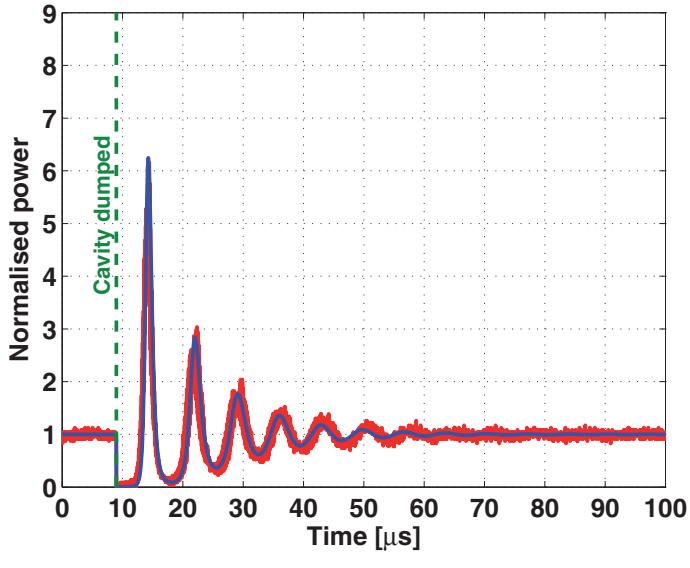

Figure 4.10: The measured data plotted together with the simulated results, from this simulation the passive losses is set to 1.4%. There is a small offset of 1 μs between the simulated and the measured cavity dumping in order for the oscillations to overlap.

By comparing figure 4.5 (b) and figure 4.8 (b) the mode matching also indicate a factor close to unity as these shows similar behavior. There are, however, some uncertainties due to the need for good filtering in order to remove all 1064nm light when measuring the relative low average power of the 593nm beam.

4.6 Conclusion

A novel generic approach for generation of pulsed radiation in the visible part of the spectrum is described. The approach has been exemplified in a specific setup generating pulses in the yellow part of the spectrum with peak powers of more than 100W. No backconversion has been observed even at high single pass powers and as simulation indicates the dynamic of the intracavity mixing reduces the prosses of backconversion. Furthermore there have been no attempt to force single frequency operation, and it is expected that this reduces backconversion even further.

The system has not yet been optimized in terms of average power, but this can be scaled in power by increasing the repetition rate of the pulsed single pass laser and by an increase in the circulating field.

Increasing the length of the high finesse cavity it is possible to store more energy and thereby increase the average power. An increase of the repetition rate would result in a linear increase of the average power without affecting the peak power of the visible pulses, as long as the circulating power reaches steady state between each pulse. Secondly, reducing the passive loss of the 1342nm laser cavity would result in increased intracavity power and thus increased peak power of the visible pulses. Relatively low peak power is needed in order to saturate the nonlinear conversion, meaning that a Q-switched laser operating at a higher repetition rate and reduced peak power would improve the overall efficiency of the system. The passive losses in the 1342nm cavity is estimated to $L_p = 1.5\%$ from the relaxation oscillation. A realistic scaling of the current system by reducing the passive losses and increasing the repetition rate of the Q-Switched laser would yield an increase of around 10 times in the average power and 4 times increase in the peak power, giving an average power of around 50-60mW and a peak power of 300-400W. Compared to a Raman based systems as demonstrated by Pask *et al.* [71] the performance is somewhat low. Though the possible for tailoring this pulsed SFG system to other wavelengths gives it huge diversity and in chapter 5 it demonstrate the synthesis of 340nm UV light based on cavity dumping of a 946nm Nd:YAG cavity is possible. In the proposed system the effective nonlinear coefficient of the nonlinear medium is of less importance, since the peak power of the single pass laser necessary to reach the depletion point is easily attained. In the suggested configuration low losses and high damage threshold of the nonlinear material is of higher importance than the high conversion efficiency, a nonlinear material such as a type I noncritically phase matched LBO, might be an appropriate choice of material for this configuration.

Chapter 5

Cascaded nonlinear UV light source

In this chapter a pulsed UV light source is investigated. In order to reach the UV region of the optical spectra two cascaded nonlinear optical crystals are used. First SHG of 1064nm light is used to generate 532nm light, then 355nm light is generated by SFG between the unconverted part of the 1064nm and 532nm wave. Combining this cascaded method for generating UV light with the nonlinear cavity dumping described in chapter 4 a whole range of different wavelengths in the UV region becomes available. This is demonstrated by generation of 340nm light. UV light is being used for a range of different applications, for example the modified Arbuzov reaction, and for irradiation of lenses from human eyes, and the presented 355nm UV light source is used for these experiments.

5.1 Introduction

UV light sources are very attractive for many applications such as lithography, chemical reactions and medical treatment. Traditionally Argon ion lasers has been used though high power UV laser based on solid state technology and nonlinear frequency conversion are becoming more and more widespread, due to their better efficiencies, compactness and ease of use compared to gas lasers. In order to efficiently generate UV light from a 1064nm Nd:YAG laser the frequency conversion is usually done extracavity, either tripling or quadrupling the 1064nm light [78, 79], this requiere active components such as Piezoeletric element and active feedback in order to be efficient are in general more complicated than passive systems. In this approach a passive Q-switch pulsed Nd:YAG laser similar to the one reported by Kitano *et al.* [80] is build. For conversion to 355nm light two nonlinear crystals are used for tripling the 1064nm pulses, first doubling in a PPKTP then SFG in a BBO.

5.2 Setup

The UV setup is shown on figure 5.1, it consists of a 5mm long Ø 3mm 1%atm doped Nd:YAG crystal (LC), and a Brewster window (BW) for polarisation control, a

Cr:YAG saturable absorber with a small signal transmission of 90% (QS) acting as a passive Q-switch and an output coupling mirror $r = 750$mm (M2), with a reflectivity of $R = 84\%$. The left end facet of the Nd:YAG crystal (M1) and the output coupling mirror forms an unstable cavity, however, supporting a Gaussian mode when sufficient thermal lensing is introduced in the Nd:YAG crystal by the pump diode. In order to avoid damaging the pump diode by the 1064nm pulses a filter (F1) coated high reflective for 1064nm and high transmitting for 808nm is inserted between the collimating lens($f = 4$mm, L1) and the focusing lens($f = 19$mm, L2). Using two steering mirrors, SM1 and SM2, which is inserted to make the setup more compact and to ease the alignment, the beam is single passed through a 12mm PPKTP poled (10mm poled) for type III SHG of 1064nm. The remaining 1064nm and the 532nm beam are then single passed through a 7mm long BBO cut for type I SFG between 532nm and 1064nm. The 355nm light is separated from the green and the infrared beam using the two filters F2 and F3. In order not to damage any of the two nonlinear crystals the lens, L3 ($f = 75$mm), is used to form a beam waist between the two crystals, this however reduces the nonlinear coupling. Though for the application which this setup is used for sufficient output power can be generated.

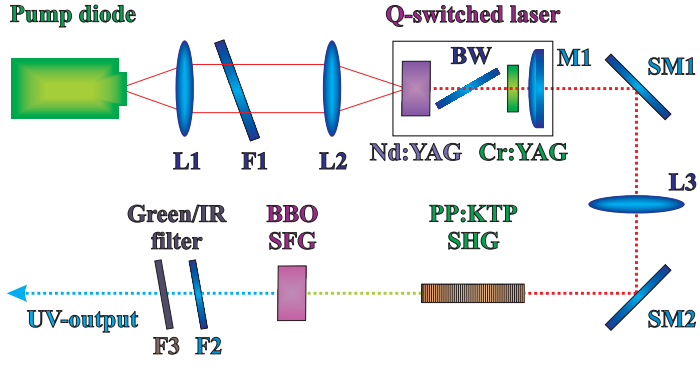

Figure 5.1: Setup for the 355 nm Q-Switched laser

5.3 Measurements

In figure 5.2 (a) the slope efficiency for the SFG 355nm light (black) and the Q-switched 1064nm laser (red) are shown, a maximum of 10mW of 355nm power is generated for a 1064nm average power of 450mW giving a conversion efficiency for the 1064nmm to 355nm light of 2% at the maximum pump power of ≈ 3.5W. The conversion efficiency factor from the pump power to the 10mW 355nm light is found to $\eta = 0.2\%$. When the laser is running close to the threshold time jitter is observed, which is normal for a passive Q-switched laser, and since the cavity is initial unstable even small changes in the thermal lensing caused by the pump beam or mechanical vibration can change the threshold condition. The variation may be small but the asymptotic behavior as seen on figure 5.2 (b) for the pulse separation results in large changes in the repetition rate even for minor changes. Time jitter is also observed at high pump power ($P_{pump} \approx 3.5$W). The reason is not clear, but

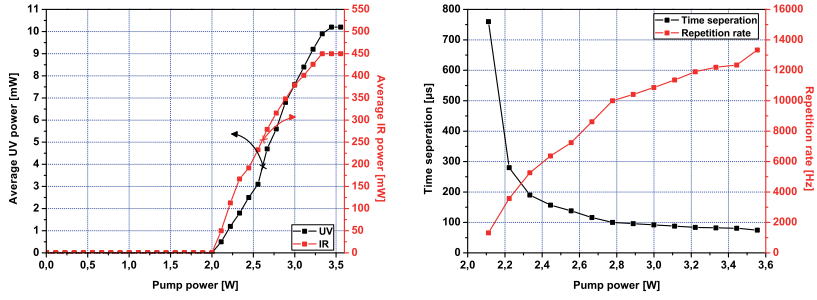

(a) (b)

Figure 5.2: (a) Slope efficiency for the 355nm light and 1064nm laser. Black line is the 355nm light and red line correspond to 1064nm laser. (b) Repetition rate and pulse separation for the 1064nm Q-switched laser. Black line correspond to the pulse separation. Red line is the repetition rate.

may origin from thermal issues. The maximum repetition rate is $\approx$ 13KHz. For all pump levels the FWHM of the pulses are 6ns for the 1064nm laser and 4.2ns for the UV generated light. Assuming Gaussian pulses the theoretical value for the FWHM duration of the UV pulse is $\Delta_{355} = \Delta_{1064}/\sqrt{3} \approx 3.5$ns, which is shorter than the measured value by 0.7ns. This is however the lower value as the available detector for measuring UV light has a rise time of 0.35ns and the oscilloscope is limited to 1GHz, which increases the measured value. On figure 5.3 the resulting peak power is shown where the measured FWHM values are used, the peak power are calculated according to:

$$P_{\text{Peak}} = \sqrt{\frac{4\ln(2)}{\pi}} \cdot \frac{< P_\lambda > \delta\tau}{\Delta_\lambda} \tag{5.1}$$

where $< P_\lambda >$ is the average power, $\delta\tau$ is the pulse separation and Δ_λ is the FWHM duration of the pulse. The prefactor is the Gaussian correction factor compared to a square pulse.
To reach a broader range of wavelengths in the UV region the cascaded system has been modified and the SFG process is done intracavity in a 946nm Nd:YAG cavity between the SHG pulsed 532nm light and the CW 946nm laser light. Currently sub mW of 340nm light has been generated using this setup and the characteristic relaxation oscillation for this system is shown in figure 5.4.

5.4 Summary

Using this compact passively Q-switched 1064nm laser 10mW of 355nm light is generated with a maximum peak power of $\approx$ 180W and a repetition rate of $\approx$ 13KHz. The conversion of 1064nm light is based on cascaded nonlinear crystals and weak focusing which yields a conversion efficiency of 2% from the 450mW of 1064nm power incident on the PPKTP crystal. Instead of cascading two nonlinear crystals a Quasi periodic structured crystal phasematching both processes could be used see chapter 2, this would reduce the size of this UV system even further. Since the pulsed 1064nm light in this case only has to be focused in a single nonlinear crystal,

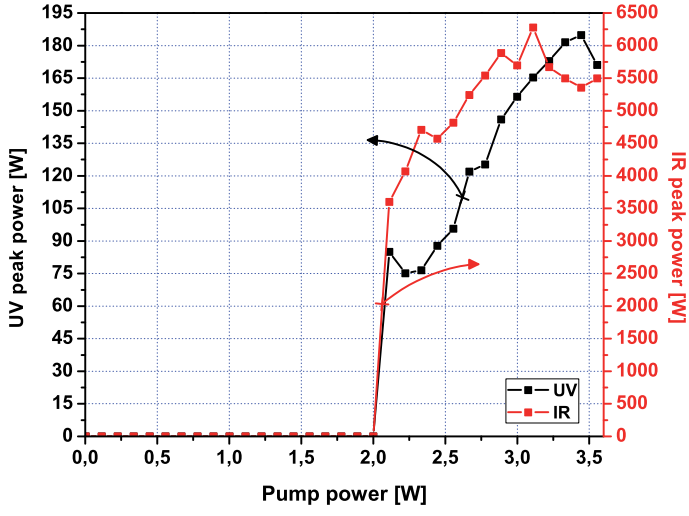

Figure 5.3: Peak power for the 355nm light and the 1064nm laser. Black line is the 355nm light and the red line correspond to 1064nm laser.

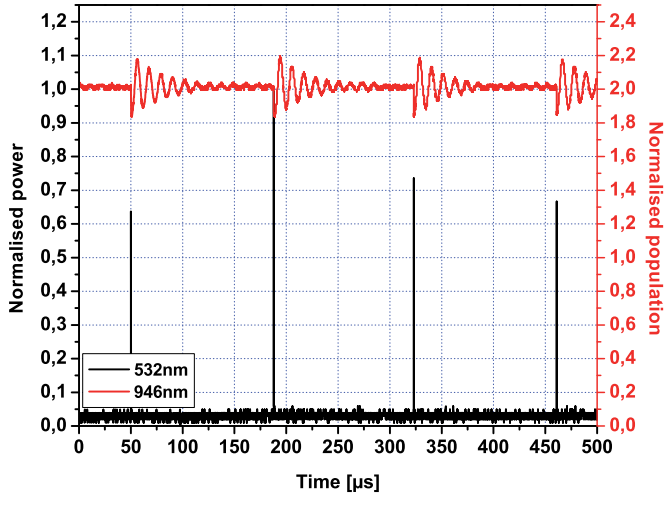

Figure 5.4: The dynamic behavior of the 340nm system. Generation of 340nm light occur when a 532nm pulse (black line) is incident on the nonlinear crystal and the relaxation oscillation for the 946nm laser is seen (red line).

it can be placed directly after the output mirror of the Q-switched laser, thereby exploiting that a positive radius of curvature of the output mirror forms a beam waist outside the 1064nm cavity. Using nonlinear cavity dumping for the second frequency conversion in a cascaded nonlinear UV system it is demonstrated that

sub mW of 340nm light can be generated.

5.5 Photo induced reactions

The pulsed UV laser is used for two very different experiments, the first is the synthesize of PentaFluoroPhenylPhosphonic Acid Ethyl Ester (PFPPAEE) using a photochemical equivalent of the Arbuzov reaction [81]. This experiment is carried out by Henrik Thalbitzer Andersen (DTU) and Frederik Diness (KU). In the second experiment the performance of this pulsed UV light source is examined for bleaching of lenses from humans eyes. This experiment is carried out by Line Kessel (KU).

5.5.1 UV enhanced Arbuzov reaction

The reaction of bromopentafluorobenzene with triethyl phosphite to produce pentafluorophenylphosphonic acid ethyl ester under the normal Arbuzov conditions is known not to take place see equation 5.2, and the route for producing PFPPAEE without photochemical assistance require reaction steps involving Cadmium as one of the catalytic components. This element is, however, highly toxic and special precautions has to be taken when working with cadmium. This reactions also leads to the formation of biproducts. Burton *et al.* [81] have shown that a similar reaction can take place under a photochemical equivalent of the Arbuzov reaction using 355nm light, as seen in equation 5.2. Their experiment was carried out using a 200W UV lamp for 120 hours, though UV lamps emit light over very broad spectral area and most of the power is emitted in the IR region. Furthermore the light is emitted in all directions and can be very hard to direct in a preferred direction (High M^2). It is therefore expected that the reaction can be enhanced using 355nm laser light which has a very narrow linewidth, and is highly directional (Low M^2) compared to the UV lamp.

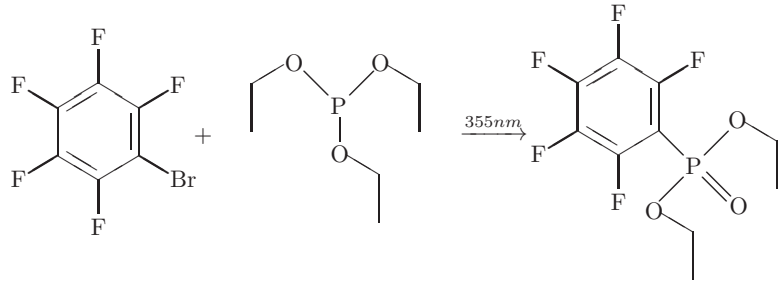

(5.2)

UV experiment

0.802mmol of bromopentafluorobenzene and 1.232mmol of triethyl phosphite where placed in a small cylindrical glass cell. One end of the glass cell is sealed with a plane quartz window in order for the 355nm light to enter. The experiment was run for approximately 50 hours with $\approx$ 10mW average UV power available, which gives around

1800J in total incident on the sample[1]. The sample is then analysed at Faculty of Pharmaceutical Sciences and the result is that 70% of the reagents have reacted and no biproducts are seen except for the residual reagents. This gives approximately 0.561mmol of PFPPAEE, and a reaction rate of 0.311mmol/KJ (mol/E_{UV}). For the UV bulb assisted experiment by Burton *et al.* the experiment had run for 120 hours using a UV light bulb with a unspecified UV radiation of 35W giving a total amount of 15.12MJ UV energy. The experiment produced 7.36mmol giving a reaction rate of 0.487nmol/KJ. By comparing the reaction rate for the two experiment it is clear that the UV laser sources is (0.311mmol/KJ)/(0.487nmol/KJ)$\approx$ 640 times more efficient than the UV bulb in terms of the emitted UV energy.

5.5.2 UV irradiation of eye lens

Cataract is a disease of the eye of the lens where the lens becomes opaque because of a change in the protein-protein interaction leading to increased light scattering [82]. It is believed that prolonged exposure to light and ultraviolet radiation is important for the formation of cataract [83]. To test this hypothesis the UV laser is used. In the experimental setup a lens is irradiated with ultraviolet light at 355nm through a 1.4mm aperture for three days with an average power of 1mW. As can be seen in figure 5.5, the lens does indeed become dark coloured after prolonged exposure to ultraviolet radiation.

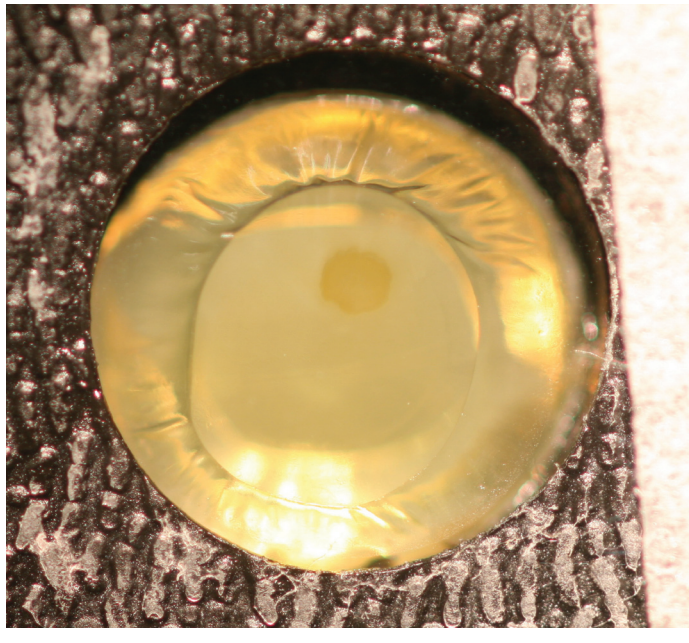

Figure 5.5: The photograph shows the lens of an eye after UV irradiation. The exposed area can be seen as a brown spot.

[1]Due to an error in the power supply the laser was shut down before the end of the experiment, so the exact time is not know.

5.6 Conclusion

Using cascaded nonlinear crystals light at 355nm is generated in a simple passive setup generating 10mW of pulsed 355nm power with a peak power of 180W using 3.5W of 808nm pump power. First doubling the Q-Switched 1064nm laser using a PPKTP crystal then sum frequency mixing the 1064nm and 532nm light using BBO. In order to reach other wavelength in the UV region The cascaded method is combined with the nonlinear cavity dumping technique and sub milliwatts at 340nm has been generated. The 355nm laser is then used for the modified Arbuzov reaction, in this experiment the use of the 10mW pulsed UV light is approximately 640 times more efficient than a 35W UV lamp in terms of emitted UV energy. Irradiating of eye lens shows that exposures to 355nm pulsed UV light forms a brown spot similar to the formation of cataract, and exposure to UV does indeed change the colour of eye lenses.

Chapter 6

488nm generation using generic design

In this chapter efficient visible light generation based on singly resonant sum frequency mixing of an external cavity tapered diode laser and a diode pumped solid state laser is presented. The generic approach described in the theory in chapter 2 is here exemplified by generation of more than 300mW of 488nm coherent blue light by mixing of a 950mW beam from an external cavity 766nm tapered diode laser with the intracavity field of a diode pumped, high finesse 1342nm solid state laser using periodically poled KTP as the nonlinear medium. Using this approach, a conversion efficiency of more than 30% of the 766nm beam was obtained.

This work has been published in:

- *Efficient visible light generation by mixing of a solid-state laser and a tapered diode laser*
  E. Karamehmedović, C. Pedersen, **M. T. Andersen** and P. Tidemand-Lichtenberg.
  Optics Express, Vol. **15**, Issue 19, 12240-12245, September 2007

- *300 mW of coherent light at 488 nm using a generic approach*
  E. Karamehmedović, C. Pedersen, **M. T. Andersen** and P. Tidemand-Lichtenberg.
  Photonic West SPIE 2008, Vol. **6875**, (Oral, paper), January 2008

6.1 Introduction

The generic approach for generating visible light described in chapter 2 is here exemplified by SFG between a Diode Pumped Solid State Laser(DPSSL) and a Tapered External Cavity Diode Laser(ECDL). The approach here combines desirable properties of different solid state technologies: the wide range of available diode lasers in the near infrared (NIR) spectral region, the tuneability of tapered ECDLs, the high intracavity power of DPSSLs and the flexibility of using quasi phasematching. As nonlinear material Periodically Poled KTP (PPKTP) is used.

6.2 Setup

The setup used in the experiment is shown in figure 6.1. It consists of a single frequency 766nm external cavity tapered diode laser, a folded cavity 1342nm solid-state laser, and a 10mm long intracavity PPKTP crystal.

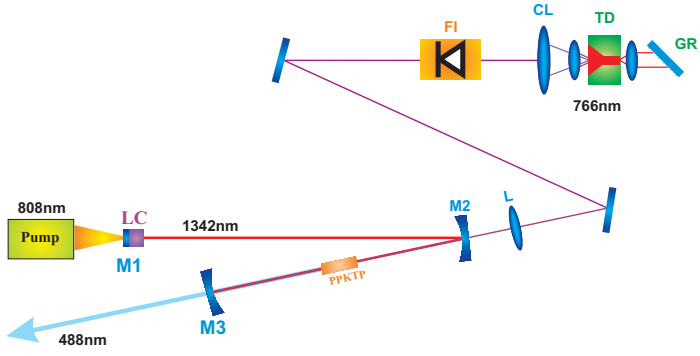

Figure 6.1: Schematic of the experimental setup. The 766nm beam from a tapered laser diode (TD) in Littrow configuration is single passed through a PPKTP crystal placed in the beamwaist of a high finesse 1342nm laser for efficient SFG into the blue spectral region.

The 1342nm solid state laser comprises a 8mm long a-cut Nd:YVO_4 crystal with a Nd doping of 0.5atm%. The high finesse cavity is formed by three mirrors: M1 (plane end surface of the laser crystal), M2 ($r = -100$mm) and M3 ($r = -150$mm). M1 is coated for high reflection at 1342nm and high transmission at 808nm. Mirrors M2 and M3 are coated for high reflection at 1342nm and high transmission at 766nm. Mirror M2 serves as the input coupling mirror for the 766nm beam. The distance between M1 and M2 is 200mm, and the separation of M2 and M3 is 208mm. The 1342nm cavity forms a beamwaist of 63μm and 54μm in horizontal and vertical plane, respectively, between mirrors M2 and M3 inside the Brewster's cut PPKTP. The position of the beamwaist is 54mm from mirror M2. The beam intensity profile was measured to be nearly Gaussian when pumped by up to 2.3W of 808nm diode power.

6.3 1342nm laser

6.3.1 Losses

The intracavity losses of the 1342nm laser are determined from slope efficiency measurements. For a four level system the slope efficiency of a high finesse cavity is given by:

$$\sigma_S \approx \frac{T}{T+\alpha}\eta \tag{6.1}$$

Where σ_S is the slope efficiency, T is the transmission of the mirror through which the slope measurement is done and α is the collection of all the other losses (denoted passive losses) in the cavity. η is the total efficiency factor for the pump power to laser power. By performing a slope measurement with two mirrors both with a well

known transmission, the passive losses in the cavity can be found from the two slope measurements:

$$\frac{\sigma_{S,1}}{\sigma_{S,2}} = \frac{\frac{T_1}{T_1+\alpha}\eta}{\frac{T_2}{T_2+\alpha}\eta} \Leftrightarrow \alpha = \frac{T_1 T_2 \left(\frac{\sigma_{S,1}}{\sigma_{S,2}} - 1\right)}{T_1 - T_2 \frac{\sigma_{S,1}}{\sigma_{S,2}}} \tag{6.2}$$

In the current setup two partly reflective (PR) mirrors at the position of M3 ($T_1 = 1.35\%$ and $T_2 = 3.5\%$) are used. From these slope measurements the passive roundtrip loss of the 1342nm cavity is found to be as low as

$$\alpha^P_{1342} = \frac{1.35\% \cdot 3.5\% \left(\frac{343}{391} - 1\right)}{1.35\% - \frac{343}{391} \cdot 3.5\%} = 0.34\% \tag{6.3}$$

6.3.2 Circulating power

To estimate the circulating power of the 1342nm laser mirror M3 is exchanged with the partly reflecting mirror ($T_1 = 1.35\%$). The small fraction of the 1342nm beam transmitted through the HR coated mirror M2 is measured. The ratio between the transmitted power of M2 and M3 is used for determining the actual transmission coefficient of M2. Thus the power leaked through mirror M2 can be used to estimate the intracavity power of the high finesse cavity. Special care is taken to avoid detection of any other signal but the 1342nm beam. Intracavity powers of up to 200W were measured when the 1342nm laser was pumped with 2.3W of 808nm with the 766nm beam blocked. When generating 229mW of blue light the intracavity power drops to 182W because of the loss introduced by nonlinear conversion.

6.4 Tapered Diode

The tapered diode laser is used in a standard Littrow configuration [84] (see figure 6.1). The rear end of the AR coated tapered diode receives feedback from a reflection grating with 1800lines/mm. The result is single frequency operation (sub MHz) and the option for wavelength tunability of the output beam of ±6nm. The maximum output power is 1.4W at a drive current of 3.1A. The output beam is collimated by two lenses (CL), and passed through a Faraday isolator (FI). Mirrors CM1 and CM2 are used for alignment and the lens (L), focus the beam into the nonlinear PPKTP crystal. The focal length of the lens is $f = 100$mm. The beam quality parameters of the tapered ECDL along the horizontal and vertical axes at the position of the nonlinear PPKTP crystal are measured to be $M^2_{H,766} = 1.48$ and $M^2_{V,766} = 2.1$, respectively, at an output power of 1.4W. However, only 68% of 766nm power from the laser reaches the nonlinear crystal due to losses in the Faraday isolator, steering mirrors and lenses. The 766nm laser is linearly polarised in the horizontal plane parallel to the polarisation axis of the 1342nm laser. The spot size (radius) of the 766nm laser at the beam waist of the 1342nm cavity is 49μm and 15μm in the horizontal and vertical plane, respectively. Furthermore, the spot size in the PPKTP crystal is magnified to 102μm in the horizontal plane, as a result of the oblique angle(Brewster's angle) of incidence at the Brewster cut PPKTP. Considering these spot sizes and the measured M^2 values, the focusing parameters are found according to [40]:

$$\xi = \frac{l}{b}, \quad b = 2z_0 = M^2 \cdot \frac{2\pi n w^2}{\lambda_0} \tag{6.4}$$

where l is the crystal length, n is the refractive indices of the crystal and w is the beam waist. This gives the following focusing parameters for the horizontal and vertical plane of the two lasers:

$$\xi_H^{1342} = 0.30, \quad \xi_V^{1342} = 0.40$$
$$\xi_H^{766} = 0.04, \quad \xi_V^{766} = 1.40$$

The generalised Boyd Kleinman factor for SFG h_m can then be calculated, and for the two directions it is found to $h_m^h = 0.09$ and $h_m^v = 0.48$ respectively using the approach by Guha *et al.* [85]. The average h_m factor is then found to $h_{eff} \approx \sqrt{h_m^h \cdot h_m^v} = 0.21$. The optimum focusing parameters are just as in the SHG case 2.84 and for these specific wavelengths and M^2 values, the beamwaist are found using equation 6.4 setting $\xi = 2.84$ which is the optimum confocal parameter [85]:

$$w_H^{1342} = \sqrt{\frac{l_c\lambda}{2\pi n M_{H,1342}^2 \xi}} = 20.3\mu m, \qquad w_V^{1342} = \sqrt{\frac{l_c\lambda}{2\pi n M_{V,1342}^2 \xi}} = 20.3\mu m$$
$$w_H^{766} = \sqrt{\frac{l_c\lambda}{2\pi n M_{H,766}^2 \xi}} = 12.5\mu m, \qquad w_V^{766} = \sqrt{\frac{l_c\lambda}{2\pi n M_{V,766}^2 \xi}} = 10.5\mu m$$

The M^2 value for the 1342nm laser in both directions is close to unity, and the beamwaists are therefore equal in size. Because of the Brewster angle the beam waist in the horizontal plane for the single pass laser has to be focused to a beam waist of $\cos(\arctan(n)) \cdot w_H^{766} \approx 6\mu m$ because of the magnification factor. The Brewster angle also magnifies the spot size for the 1342nm laser, though the magnification can be compensated by working close to the Gaussian stability edge found using ABDC calculations. From the confocal parameters for the system it is clear that the system is not operated at the optimum focusing. There are, however, other factors that has to be considered which limits the performance under optimum focusing. Since the PPKTP is positioned intracavity of the 1342nm resonator the beam waist formed is a function of the geometry of the resonator, and has to obey the stability criteria. In order to avoid damaging the nonlinear crystal due to the high circulating power the beam waist is deliberately larger than required for optimum focusing. The Brewster angle of the PPKTP minimise the losses in the cavity, though the oblique angle enlarges the spot size for the single pass laser in the horizontal plane by a factor of $m = 1/\cos(\arctan(n_{PPKTP}) \approx 2$. The M^2 value of the 766nm tapered diode also reduces the confocal parameter and together with the difficulties of having a fast and a slow axis, an experiment was carried out where the tapered diode is coupled into a single mode polarising maintaining fibre, this reduces the M^2 value and removes the ellipticity of the tapered diode, this experiment is described in more details in chapter 7. However a significant increase of the nonlinear coupling efficiency is expected from an improved mode matching of the fundamental 766nm beam in the current setup.

Figure 6.2 shows the emitted spectra from the two lasers. Note that the linewidth of the ECDL is smaller than the resolution of the instrument (5pm). The wavelength stability of the 766nm ECDL was measured over a period of one hour. The maximum deviation from the nominal wavelength during this period was measured to be 5pm, again limited by the resolution of the spectrometer. The spectrum of the 1342nm laser contains multiple peaks corresponding to etalon effects in the 8mm long Nd:YVO_4 crystal in combination with the gain bandwidth of the Nd:YVO_4.

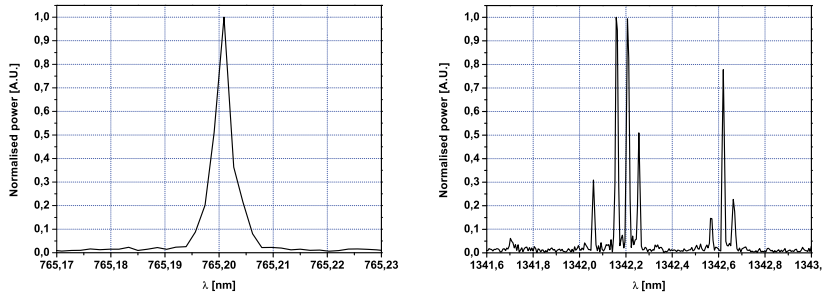

(a) **(b)**

Figure 6.2: (a) Spectrum of the 766nm tapered diode laser and (b) spectrum of the high finesse 1342nm laser.

The spectrum of the 1342nm laser is not stable over time, but changes in a slowly manner. The relatively broad linewidth of the free running 1342nm laser also reduces the coupling efficiency. For a 10mm long PPKTP crystal the FWHM wavelength acceptance bandwidth at 1342nm is 0.4nm [53, 86] which is the same as the cluster spacing shown at the spectrum in figure 6.2 (b). By inserting a thin etalon the spectrum can be narrowed and it is expected to increase the nonlinear coupling, a more detailed description of a 1342nm laser with a etalon inserted is described in chapter 9. The power stability of the 766nm ECDL was measured over a period of one hour. After reaching thermal equilibrium, power fluctuations of less than 1% were measured.

6.5 Sum frequency generation

The PPKTP crystal is temperature controlled using a peltier element. Optimizing the temperature of the PPKTP crystal for maximum conversion efficiency a phase-match temperature of approx. 42.5° C was found. This resulted in a maximum of 308mW of blue light at 488nm when pumping the Nd:YVO_4 laser crystal with 2.3W of 808nm pump power corresponding to a drive current of 2.5A. The tapered ECDL power incident on the PPKTP crystal was 950mW, corresponding to a maximum drive current of 3.1A. Thus the conversion efficiency of the incident 766nm power to 488nm blue light was 32% at this pump level for the 1342nm cavity. When the two incident beams are considered nondepleted, a linear relation exists between the fundamental powers and the generated power.

$$\begin{aligned} P_{SFG} &= \eta_{\mathrm{SFG}} \cdot P_{1342,circ} \cdot P_{766} \cdot h_m \\ &= \eta_{eff} \cdot P_{1342,circ} \cdot P_{766} \end{aligned} \tag{6.5}$$

where P_{766} is the power of the 766nm beam, $P_{1324,circ}$ is the circulating steady state intracavity power at 1342nm, P_{488} is the power of the generated beam, and η_{eff} is the conversion efficiency factor. From these results the measured efficiency factor can be found:

$$\eta_{eff}^{meas.} = \frac{308\mathrm{mW}}{950\mathrm{mW} \cdot 182\mathrm{W}} = 0.0018\mathrm{W}^{-1} \tag{6.6}$$

The theoretical value for the efficiency factor η_{eff} for the interaction can then be found from equation 2.21 which is the same expression reported by Tukker *et al.* [87] and the MatLabcode can be found in appendix A.3:

$$\eta_{eff}^{theo} = \frac{32\pi d_{eff}^2 l_{NLO}}{n_1 n_2 n_3 c\epsilon_0 \lambda_1 \lambda_2} \frac{k_1 k_2}{k_1 + k_2} \cdot h_{eff}$$
$$\eta_{eff}^{theo} = 0.0301\mathrm{W}^{-1} \cdot 0.21 = 0.0063\mathrm{W}^{-1} \tag{6.7}$$

Where n is the refractive indices, c is the speed of light, ϵ_0 is the permittivity of free space, l_{NLO} is the length of the nonlinear crystal, d_{eff} is the effective nonlinear coefficient and $k_{1,2}$ are the wavevectors inside the nonlinear crystal. The theoretical value is seen to be 3.5 times larger than the measured. The theoretical value, however, do not take into account that both the 1342nm circulating field and the 766nm laser does contain astigmatism. The 1342nm resonator is a folded cavity and contains a Brewster cut PPKTP, which from ABCD matrices introduce an axial astigmatism of around 5mm. For the 766nm laser astigmatism is introduced from the difference in the M^2 value for the horizontal and vertical plane but also because of the Brewster crystal and unfortunately the astigmatism is opposite compare to the 1342nm laser giving $z_h^{766} \approx z_v^{1342}$ reducing the mode overlap.

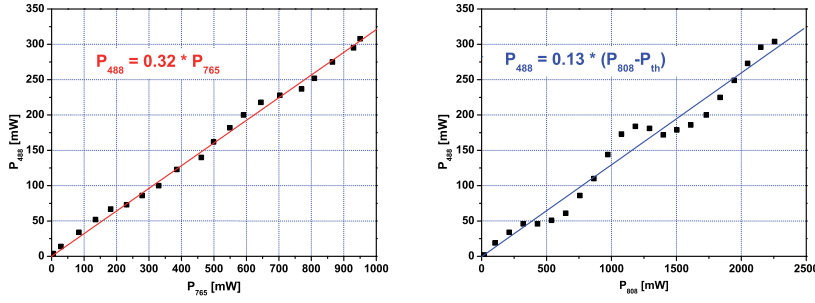

(a) (b)

Figure 6.3: (a) Power of the generated 488nm light as a function of the injected 766nm power when $P_{808} = 2.3$W. (b) Power of the generated 488nm light as a function of 808nm pump power, P_{808}, for the 1342nm laser and with $P_{766} = 950$mW incident on the nonlinear crystal.

Figure 6.3 (a) shows the power of the generated blue light as a function of the injected 766nm power, when changing the current of the tapered ECDL from 0 to 3.1A. An almost linear dependency is seen as expected from equation 6.5. This is in strong contrast to second harmonic generation, where the dependence is parabolic. The deviation from a straight line is believed to be due to small changes in the intensity profile of the focused 766nm beam as the diode laser current changes. The change in the intensity profile in turn alters the efficiency of the SFG process. The conversion efficiency of the 766nm beam to the 488nm beam in the present configuration is found to be approx. 32%, independently of the power of the 766nm beam. The output power at 488nm as a function of pump power of the 1342nm laser is shown in figure 6.3 (b). The cavity was optimised at a 808nm pump power of 2.3W. Varying the pump power changes the thermal lens in the laser material, thus displacing the beamwaist as well as perturbing the oscillating spectrum of

the 1342nm laser. These effects resulted in the nonlinear characteristics of the curve shown in figure 6.3 (right). The spectrum of the generated blue light at the optimal PPKTP temperature is shown in figure 6.4 (a). Comparing with figure 6.2 (b), a strong resemblance to the asymmetrical spectrum of the 1342nm laser having two clusters of characteristic peaks is clearly seen. The measured 488nm output power as a function of PPKTP temperature is shown in figure 6.4 (b), (black squares). The measured FWHM temperature acceptance bandwidth is approx. 3.5° C. Theoretically, a FWHM temperature acceptance bandwidth of 3.2° C is found, see figure 6.4 (b, (green curve) [53, 88, 89]. The increased bandwidth seen in figure 6.4 (b) is primarily due to the two clusters in the spectrum of the 1342nm laser seen as shown in figure 6.2 (b).

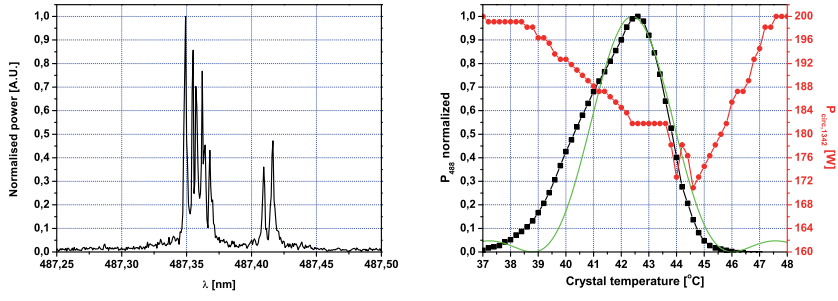

(a) (b)

Figure 6.4: (a) Spectrum of the generated 488nm light and (right) normalised 488nm output power as a function of the temperature of the PPKTP crystal (black squares). The green curve shows the theoretical acceptance temperature of 3.2 °C assuming spectral delta functions. The corresponding change in the intracavity 1342nm power (red circles) is also shown.

Figure 6.4 (b, red circles) shows the circulating intracavity power of the 1342nm laser as a function of the PPKTP temperature. Since the phasematch condition is a function of temperature, also the intracavity power changes, since a part of the 1342nm photons are converted into 488nm photons. The nonlinear loss at 1342nm, $\alpha_{1342}^{\mathrm{SFG}}$, is proportional to the generated 488nm power, P_{488}. At the optimum phasematch temperature the intracavity 1342nm power is decreased by approx. 10% ($\mathrm{P}_{1342,\mathrm{PM}} = 182\mathrm{W}$) compared to the non phasematched power ($\mathrm{P}_{1342,\mathrm{NPM}} = 200\mathrm{W}$). The losses for the 1342nm resonator due to the nonlinear interaction, is found by picturing the losses as an output coupler, since the output coupled 1342nm light is converted to 488nm light, the measured 488nm power, P_{488}, is proportional to the P_{1342}^{SFG} by the energy ratio:

$$P_{1342,PM} \cdot \alpha_{1342}^{SFG} = P_{out}^{SFG} = P_{488} \cdot \frac{488\mathrm{nm}}{1342\mathrm{nm}} \tag{6.8}$$

When the PPKTP temperature scan was performed, the phasematched output power was $\mathrm{P}_{488} = 229\mathrm{mW}$, and the nonlinear loss at 1342nm is then found to:

$$\alpha_{1342}^{SFG} = \frac{488\mathrm{nm}}{1342\mathrm{nm}} \cdot \frac{229\mathrm{mW}}{182\mathrm{W}} \approx 0.046\% \tag{6.9}$$

Knowing the nonlinear loss, it is possible to calculate the passive loss of the 1342nm laser, using a different approach compared to the previously described method which

relied on the slope efficiencies. Since the pump power of the 1342nm laser is kept constant throughout the temperature scan, the circulating power of the 1342nm in the non phasematch and phasematch case is given by:

$$P_{1342,NPM} = \frac{P_{\text{pump}}}{\alpha^{P}_{1342}}, \quad P_{1342,PM} = \frac{P_{\text{pump}}}{\alpha^{P}_{1342} + \alpha^{SFG}_{1342}} \tag{6.10}$$

as the nonlinear loss is only present under the SFG process. This gives the following relation for the passive loss:

$$\alpha^{P}_{1342} = \frac{P_{1342,\text{PM}} \cdot \alpha^{\text{SFG}}_{1342}}{P_{1342,\text{NPM}} - P_{1342,\text{PM}}} = \frac{182\text{W}}{200\text{W} - 182\text{W}} \cdot 0.046\% \approx 0.47\% \tag{6.11}$$

This confirms that the passive intracavity loss α^{P}_{1342} is indeed very small, thus resulting in the very high circulating intracavity power reported here. The actual difference between the 0.34% passive loss of the 1342nm cavity calculated using the slopes efficiency approach and the 0.47% passive loss found using the change of intracavity 1342nm power due to the nonlinear conversion can be explained by an additional scattering loss induced by thermal lensing of the blue light in the PPKTP crystal. Since the passive losses are very small even the small changes due to temperature in the PPKTP may slightly missalign the cavity which increases the passive losses in the cavity. In addition to the expected decrease in intracavity power proportional to the generated sum frequency signal, there are some additional drops in circulating power at 44-46 ° C. The reason for this decrease in power is not know, but it may be caused by thermal effects in the PPKTP crystal thereby changing the spectral or the spatial properties of the 1342nm laser. This is to be investigated further. The stability of the 488nm beam was measured, showing a slow power variation of less than 3%. The fluctuation is ascribed to an instability of the intracavity power of the DPSSL, primarily due to mechanical and thermal changes in the setup. Finally, in spite of very high intensities inside the PPKTP crystal, no grey tracking was observed even after several hours of operation at maximum currents.

6.6 Conclusion

More than 300mW of coherent 488nm light was generated by sum frequency mixing in an intracavity singly resonant configuration using a diode pumped solid state 1342nm Nd:YVO_4 laser and a single frequency tapered ECDL at 766nm. A power conversion efficiency of 32% of the 766nm beam to 488nm was achieved in the mixing module. Furthermore, it was shown that the power conversion efficiency at a constant 808nm pump level of the mixing module is practically independent of the injected power of the 766nm beam. Thus, the technique is equally efficient for high and low power seed lasers, as long as the small signal regime is maintained that is, as long as the circulating 1342nm power is not significantly depleted. This is in strong contrast to SHG. There are several ways to improve the experimental realisation of the system. The mechanical, thermal and spectral properties of the system can be significantly improved especially in the 1342nm laser, and it is believed that power scaling to the watt level of the suggested system is straightforward, since no saturation effects have been observed. In conclusion, we have demonstrated the possibility to synthesise visible light at a predetermined wavelength using the

suggested generic approach. The particular system generates light at 488nm, but by using a tapered diode laser with an appropriate wavelength or by using the different solid state laser lines, combined with the flexibility of using PPKTP makes it possible to generate light efficiently at virtually any desired wavelength within the visible spectrum.

Chapter 7

Fibre coupled Tapered diode

In this chapter the beam from the tapered diode is coupled into a single mode polarising maintaining fibre. This removes high order transverse modes and astigmatism from the beam. The drawback is the high losses from coupling the 766nm beam into the fibre. The influence on the mixing process between this mode cleaned tapered diode and the solid state mixing module is investigated

This work has been published in:

- *300 mW of coherent light at 488 nm using a generic approach*
  E. Karamehmedović, C. Pedersen, **M. T. Andersen** and P. Tidemand-Lichtenberg.
  Photonic West SPIE 2008, Vol. **6875**, (Oral, paper), January 2008

7.1 Setup

The setup is similar to the one used in chapter 6, although the 1342nm module is in this case a z-shaped cavity. The change in the 1342nm module is done because simulations indicate that this setup is more stable with respect to thermal lensing. The setup is shown on figure 7.1.
The 1342nm solid state laser comprises an 8mm long a-cut Nd:YVO_4 crystal with a Nd doping of 0.5atm%. The high finesse cavity is formed by four mirrors coated for high reflection at 1342nm: M1 (plane end surface of the laser crystal), M2 ($r = -100$mm), M3 ($r = -150$mm) and M4 (plane mirror). M1 is coated for high reflection at 1342nm and high transmission at 808nm. Mirror M2 is coated for high transmission at 766nm and serves as the input coupling mirror for the 766nm beam. The distance between M1 and M2 is 213mm, and the separation of M2 and M3 is 178mm. The mirrors M3 and M4 are 250mm apart. The 1342nm cavity forms a beamwaist between mirrors M2 and M3 inside the Brewster's cut PPKTP. The beamwaist in the crystal has theoretical dimensions of around 62μm and 39μm in horizontal and vertical axis, respectively. The position of the beamwaist is around 66mm from mirror M2. The beam intensity profile was measured to be nearly Gaussian when pumped by up to 3W of 808nm diode power. The passive losses of the 1342nm laser are found using the method described in chapter 6. The slope efficiency measurements are done using to PR mirrors at the position M4 ($T = 1.35\%$ and $T = 3.7\%$) using equation 6.2 the passive roundtrip loss of the 1342nm

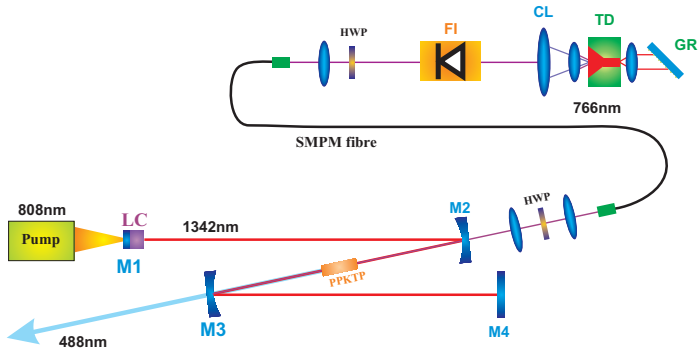

Figure 7.1: Schematic of the experimental setup: The 766nm beam from a Tapered laser Diode (TD) in Littrow configuration is coupled into a single mode polarising maintaining fibre(SMPM) and single passed through a 10mm long PPKTP crystal, which is placed in the beamwaist of a high finesse 1342nm laser for efficient SFG into the blue spectral region.

cavity is found to be as low as $\alpha^P_{1342} = 0.6\%$.

$$\alpha^P_{1342} = \frac{1.35\% \cdot 3.7\% \left(\frac{277}{344} - 1\right)}{1.35\% - \frac{277}{344} \cdot 3.7\%} = 0.60\% \tag{7.1}$$

The circulating power of the 1342nm resonator is found as described in chapter 6 here M4 is exchanged with a $T = 1.35\%$ mirror and the leakage power through M2 is measured. This way the circulating field in the high finesse cavity is found to 105W when pumping with 2.0W of 808nm pump power and with the 766nm beam blocked. When generating 94mW of blue light, the intracavity power drops by around 8% to 96.6W because of the loss introduced by the nonlinear conversion.

7.2 Fibre coupled Tapered Diode

The beam quality parameters of the tapered ECDL along the horizontal and vertical axes after passing through the Faraday isolator are measured to be $M^2_H = 1.4$ and $M^2_V = 1.6$, respectively, at an output power of 1.4W (1.2W after the isolator). The linearly polarised light is coupled into a Single Mode Polarisation Maintaining (SMPM) fibre with design wavelength of 980nm. Around 50% of light is transmitted through the fibre and together with reflective losses in the steering mirrors, the coupling mirror M2 and the HalfWave Plate (HWP), and of the 1.4W power of output from the 766nm tapered ECDL around 550mW reaches the nonlinear crystal. The 766nm laser is linearly polarised in the horizontal plane and parallel to the polarisation axis of the 1342nm Nd:YVO_4 laser. However, it is observed that the polarisation of the beam is not stable, especially at high output powers for the tapered ECDL. The SMPM fibre available for this experiment has as mentioned a cutoff wavelength of 980nm which is far from the ECDL wavelength of 766nm. The result is that high order modes for 766nm is occasionally excited in the fibre which leads to instability of the polarisation. As a consequence it is necessary to reduce the output power of the tapered diode laser to around 500mW to stabilise the polarisation, and a maximum of 200mW 766nm light is incident on the crystal during sum frequency generation.

The beamwaist diameter of the 766nm laser inside the Brewster cut PPKTP is measured to be 104μm (50μm in free space) and 52μm in the horizontal and vertical plane, respectively. The beam quality parameters at the crystal surface are measured to $M_H^2 = 1.2$ and $M_V^2 = 1.2$. From these values the confocal parameter is found using the same approach as in the previous chapter from equation 6.4

$$\xi_H^{1342} = 0.30, \quad \xi_V^{1342} = 0.77$$
$$\xi_H^{766} = 0.05, \quad \xi_V^{766} = 0.20$$

From these numbers the generalised Boyd Kleinman factor for the two directions is numerically found to $h_m^h = 0.11$ and $h_m^v = 0.36$. The average factor is calculated to $h_{eff} \approx 0.20$. With the better M^2 value the optimum beamwaists are calculated to:

$$w_H^{1342} = \sqrt{\frac{l_c\lambda}{2\pi n M_{H,1342}^2 \xi}} = 20.3\mu m, \qquad w_V^{1342} = \sqrt{\frac{l_c\lambda}{2\pi n M_{V,1342}^2 \xi}} = 20.3\mu m$$
$$w_H^{766} = \sqrt{\frac{l_c\lambda}{2\pi n M_{H,766}^2 \xi}} = 13.9\mu m, \qquad w_V^{766} = \sqrt{\frac{l_c\lambda}{2\pi n M_{V,766}^2 \xi}} = 13.9\mu m$$

Because of the Brewster angle the beam has to be focused to $\approx$ 6.62μm. The spectrum of the Tapered Diode is shown in figure 7.2 (a) which is limited by the resolution of the optical spectrum analyser, and the spectrum of the 1342nm laser is shown on figure 7.2 (b)

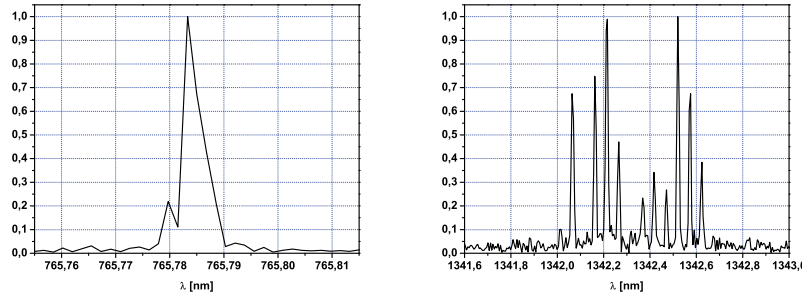

(a) **(b)**

Figure 7.2: (a) Spectrum og the 766nm Tapered ECDL, the spectrum is limited by the resolution of the OSA. (b) Spectrum of the high finesse 1342nm laser at three different pump current I_{pump}

7.3 Sum Frequency Generation

The PPKTP crystal is temperature controlled using a Peltier element. Optimizing the temperature of the PPKTP crystal for maximum conversion efficiency, a phase-match temperature of approx. 51 $°C$ was found. This is around 8 degrees difference than from the optimum temperature found in chapter 6 and is caused by a minor shift in the wavelength of the tapered ECDL, since the phasematch temperature is strongly dependent on the wavelength. In the first experiment the Tapered diode

was kept at $\approx$ 765.8nm and in this the wavelength was at 765.2nm. Theoretically this shift correspond to $\approx 7.5\,^{\circ}C$ using a poling period of 7.2μm and the sellmeier equation for KTP published in [86]. A maximum of 94mW of blue light at 488nm when pumping the Nd:YVO_4 laser crystal with 2W of 808nm pump power corresponding to a drive current of $I_{808} = 2.3$A and a intracavity power of 105W is measured. The tapered ECDL power incident on the PPKTP crystal is measured to 200mW, corresponding to a drive current of 2A. Thus, the conversion efficiency of the incident 766nm power to 488nm blue light is 47% at this pump level for the 1342nm cavity. From these results the measured efficiency factor given in equation 6.5 can be found:

$$\eta_{eff}^{meas.} = \frac{94\text{mW}}{200\text{mW} \cdot 96.6\text{W}} = 0.0048\text{W}^{-1} \tag{7.2}$$

The theoretical value for the efficiency factor is found to:

$$\eta_{eff}^{theo} = 0.0301\text{W}^{-1} \cdot 0.20 = 0.0060\text{W}^{-1} \tag{7.3}$$

The measured value is nearly 3 times higher than the one given in equation 6.6, though the theoretical estimate is identical. Assuming that mode overlap etc. is more or less the same in this experiment, there are only one main factor which can explain this significant increase of the coupling efficiency. The M^2 factor is only introduced as a decrease in the confocal parameter, though in reality a beam with a poor M^2 factor consist of many high order modes with a decreasing nonlinear coupling efficiency. The interaction between different high order modes through the nonlinear coupling should be included to get a better theoretical estimate, this has recently been demonstrated by Buchhave *et al.* [90]. The measured value is, however, close to the theoretical estimate and the difference is believed to be mainly due to the beams deviation from the pure Gaussian. In chapter 8 a similar experiment is done using a Titan Sapphire ringlaser as the single pass laser, here the beam quality is close to the Gaussian profile.

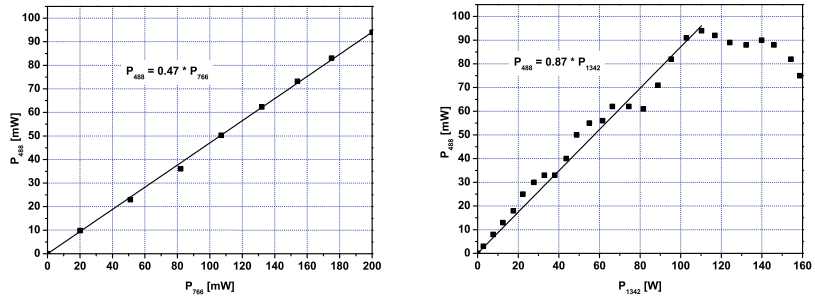

(a) **(b)**

Figure 7.3: (a) Power of the generated 488nm ligth as function of the single pass power of 766nm Tapered ECDL, with $P_{1342} = 105$W circulating power. (b) Power of the generated 488nm light as function of the intracavity power of the high finesse 1342nm laser, with $P_{766} = 200$mW incident on the PPKTP.

Under small signal approximation, the conversion efficiency η_{eff} for the single pass 766nm tapered ECDL can be found from figure 7.3 (a) to 47% which is approxi-

mately 15% better than for the previous chapter even at significantly lower circulating power. Figure 7.3 (a) shows the generated 488nm light as a function of the injected 766nm power when $I_{808} = 2.3$A. A linear dependence is seen as expected from equation 6.5 (small signal regime). Figure 7.3 (b) shows the generated 488nm light as a function of the intracavity 1342nm power, which is controlled by the drive current I_{808} of the broad area pump diode. The power of the 766nm tapered ECDL is kept constant at 200mW. The rolloff at high intracavity power is attributed to thermal effects such as thermal lensing. For strong thermal lensing the eigenmode of the cavity changes resulting in a change in the position of the beamwaist situated inside the PPKTP thereby reducing the mode overlap between the two interacting beams. It is therefore vital to optimise the cavity at a working point, and this was done for a circulating power of 105W ($I_{808} = 2.3$A). Furthermore the threshold for higher order cavity modes are reached at high pumping, and since the mixing process is most efficient between fundamental modes the efficiency of the process is decreasing.

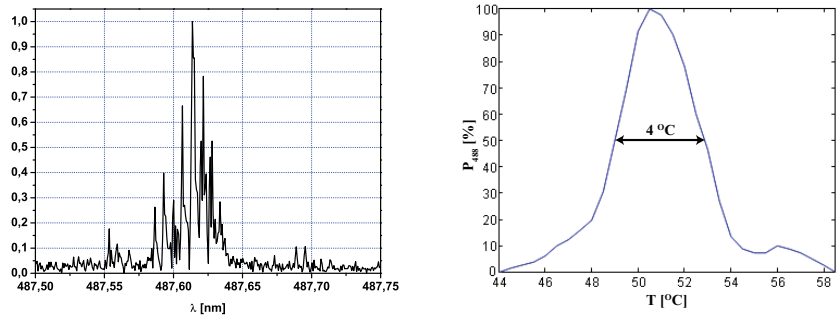

(a) **(b)**

Figure 7.4: (a) Spectrum of the generated 488nm light. (b) Temperature acceptance bandwidth for the 10mm Brewstercut PPKTP, the bandwidth is found to 4 °C.

The spectrum of the generated blue light at the optimal PPKTP temperature is shown at figure 7.4 (a) and in figure 7.4 (b) the normalised 488nm light is shown as function as the temperature of the PPKTP. The FWHM is found to 4 °C. The theoretical curve can be seen on figure 6.4 where the FWHM is found to be 3.2 °C. The measured T_{FWHM} is slightly larger than the one found in the previous experiment, though because of the strong dependence for the phasematch of the interacting beams and the relatively large spectrum for the 1342nm the measured temperature acceptance bandwidth agrees well with the theoretical calculated using monochromatic light. From the temperature scan the active loss can be calculated using equation 6.8:

$$\alpha_{1342}^{SFG} = \frac{488\text{nm}}{1342\text{nm}} \cdot \frac{94\text{mW}}{96.6\text{W}} = 0.035\% \tag{7.4}$$

again the passive losses can be calculated from the steady state circulating powers of the 1342nm cavity and the active loss using equation 6.11:

$$\alpha_{1342}^{P} = \frac{96.6\text{W}}{105\text{W} - 96.6\text{W}} \cdot 0.034\% \approx 0.41\% \tag{7.5}$$

This is also in very good agreement with the value obtained using the slope method.

7.4 Conclusion

Using a single mode polarising maintaining fibre for mode cleaning of the Tapered ECDL is shown to have a significant effect on the conversion efficiency. The result is nearly 3 times increase in the η_{eff} compared to the setup described in chapter 6. However the cost is a loss of more than 50% of the output power from the Tapered ECDL, and as a change in the drive current for the Tapered diode changes the focus point for the fast axis making it necessary to realign the fibre coupling. A more elaborate scheme would be to improve the beam quality of the Tapered diode itself. If the power level of the generated beam is not the most vital part, the nonlinear interaction can itself be used for mode cleaning, since the interaction between the two beams are placed in the focal point of both laser beams the convolution between the higher order spatial frequency can be reduced by varying ratio of focusing between the two lasers. A demonstration of this concept has been published by Tidemand-Licthenberg *et al.* [91].

Chapter 8

488nm generation using Ti:Sapphire

In this chapter a Titan Sapphire(Ti:S) ringlaser is used as the single pass laser. This laser oscillates on a single longitudinal mode with a Gaussian spatial distribution, giving the most optimum beam for nonlinear interaction. Comparing the performance of the tapered diode to the Ti:S laser gives an idea how well the tapered diode system can be optimised.

This work has been published in

- *Comparison of a Ti:S Laser and a Tapered External Cavity Diode Laser for Sum Frequency Generation in a High-Finesse 1342 nm Nd:YVO_4 Laser*
  M. T. Andersen, P. Tidemand-Lichtenberg, E. Karamehmedović and C. Pedersen.
  ASSP 2008, WB19, (Poster, abstract), January 2008

8.1 Setup

The SFG setup is shown in figure 8.1. It consists of a folded 1342nm laser cavity including a Brewster cut periodically poled KTP crystal situated as an intracavity component. The 1342nm laser comprises a 8x3x3mm^3 Nd:YVO_4 crystal with a doping level of 0.5atm%, folding mirrors M5 (planar), M6($r = -100$mm) and the end mirror M7 ($r = -50$mm). The end surface of the laser crystal and the mirrors M5, M6 and M7 are coated for high reflection at 1342nm. The Nd:YVO_4 laser crystal is end pumped by a Lumics fibre coupled 3W laser diode. The 1342nm cavity forms a beamwaist of approximately 80μm and 30μm in horizontal and vertical axis, respectively, between mirrors M6 and M7 inside the PPKTP. The Ti:S laser consists of a 10x3x3 mm^3 Ti:S crystal with a doping level of 0.15atm%, two curved mirrors M1 and M2 ($r = -100$mm) and two plane mirrors M3 and M4. Mirrors M1, M2 and M3 are coated for high reflection at 680-880nm, whereas M4 is 95% reflective and used as the output coupling mirror for the Ti:S laser. The birefringent plates are used for tuning the wavelength of the laser. In the present setup the wavelength of the Ti:S laser is tuned to 766nm. To obtain single frequency operation, a TGG crystal is inserted together with a HWP enforcing unidirectional operation. The Ti:S laser is pumped by a 5W, Coherent 532nm Verdi laser. CM1 (plane mirror)

is used for alignment of the 766nm beam to the 1342nm cavity. The 10mm long Brewster cut PPKTP crystal is poled with a QPM period of 7.1μm, corresponding to first order SFG of the 766nm and 1342nm lasers.

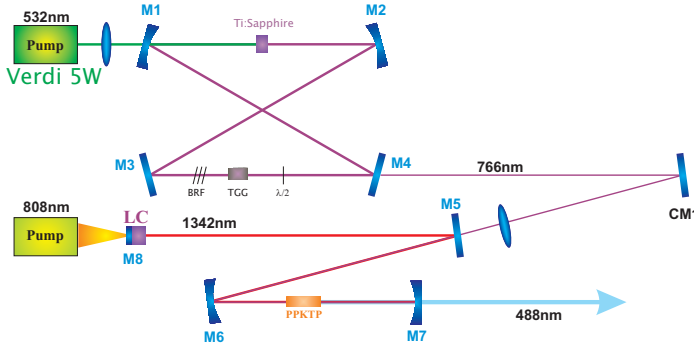

Figure 8.1: Schematic setup for generation of CW 488nm light using a 766nm Ti:Sapphire ringlaser and z-shaped Nd:YVO_4 laser oscillating at 1342nm. The Brewster cut PPKTP is placed intracavity of the 1342nm laser.

8.2 Focusing parameters

The focusing parameters in this experiment is estimated using the beamwaist values found by ABCD matrix calculations. The beam waist for the 1342nm is estimated to $w_H^{1342} = 83\mu$m and $w_V^{1342} = 30\mu$m and $w_H^{766} = w_V^{766} = 30\mu$m for the Ti:S laser. And under the assumption than both beams are close to a TEM_{00} mode the focusing parameters is then found to:

$$\xi_H^{1342} = 0.17, \quad \xi_V^{1342} = 1.30$$
$$\xi_H^{766} = 0.17, \quad \xi_V^{766} = 0.73$$

giving a Boyd Kleinman factor of $h_m^h = 0.16$ and $h_m^v = 0.77$, which gives an average $h_{eff} = 0.36$. For a system with $M^2 = 1$ the optimum beamwaist are found to:

$$w_H^{1342} = 20.3\mu m, \qquad w_V^{1342} = 20.3\mu m$$
$$w_H^{766} = 15.2\mu m\,(7.3\mu m), \qquad w_V^{766} = 15.2\mu m$$

8.3 Sum Frequency Generation

The optimum temperature of the PPKTP crystal is found to $52\,°C$, depending on the precise wavelength of the 1342nm and Ti:S laser see figure 8.2. The full width half maximum temperature acceptance is measured to 3.5 degrees, which fits well with the theoretical phasematch curve calculated for the Ti:S laser running at 765.1nm with a full width half maximum of 3.2 degrees [53, 88, 89]. In figure 8.2 (b) the generated 488nm power, P_{488} is shown as function of the 766nm single pass power, P_{766}, for three levels of circulating 1342nm power, P_{1342}. The typical linear dependence of the single pass laser is clearly seen, as expected from a nondepleted system given by equation 6.5 From figure 8.2 (b) the single pass conversion efficiency

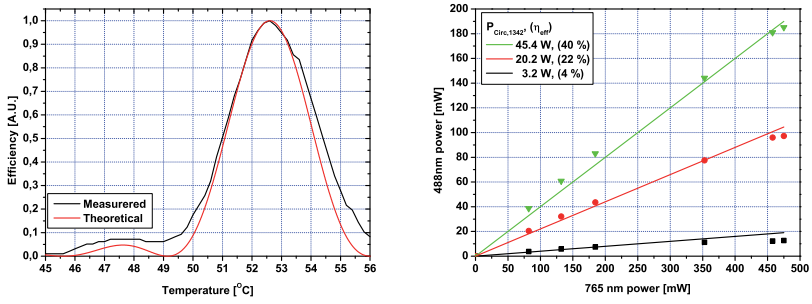

(a) (b)

Figure 8.2: (a) Temperature acceptance bandwidth of the PPKTP. The dip in the measured curve is believed to be due to a wavelength shift of the Ti:S laser. (b) Conversion efficiency for the single pass Ti:S laser at three different circulating fields.

can be found and for a circulating power of 45.4W the slope efficiency is found to 40% for the fitted curve:

$$\eta_{SP} = \frac{P_{488}}{P_{766}} = \frac{189\text{mW}}{470\text{mW}} \approx 40\% \tag{8.1}$$

The measured η_{eff} in equation 6.5 is found to:

$$\eta_{eff}^{meas} = \frac{P_{488}}{P_{1342} \cdot P_{766}} = \frac{189\text{mW}}{45.4\text{W} \cdot 470\text{mW}} = 0.0089\text{W}^{-1} \tag{8.2}$$

A theoretical value is found to:

$$\eta_{eff}^{theo} = 0.0301\text{W}^{-1} \cdot 0.36 = 0.0107\text{W}^{-1} \tag{8.3}$$

The measured value is in good agreement with the theoretical estimated value, and the deviation can be attributed to the estimate of the beamwaists and that the M^2 value are assumed to be unity. The measured efficiency value are however around 2 times bigger than for the fibre coupled tapered ECDL and more than 6 times greater than using the non coupled Tapered ECDL directly. The Boyd Kleinman factor in this experiment is nearly twice the value found for the Tapered ECDL experiments. Optimising the focusing in the Tapered ECDL experiment it is expected that an increase in generated power by a factor of 2 especially in the SMPM fibre coupled experiment.

8.4 Summary

Figure 8.3 compares the 488nm power as a function of the incident 766nm light from the three experiment. The conversion efficiencies are - 32%, 47% and 40%, respectively. Note, however, the difference in the circulating power in the three setups. In the experiments with the tapered ECDL the circulating field is more than four times higher than in the Ti:S setup and 2 times higher in the SMPM tapered diode. The focusing in the three experiments are not the same and optimised

focusing is expected to improve the performance of all the three systems. The important parameters for the three systems are summarised in table 8.1 and looking at the agreement between the measured and theoretical value it is clear that the mode quality plays a vital role in the performance of the mixing process, even though the M^2 value has been included in the calculation of h_m. Including the Boyd Kleinman factor in the theoretical estimation of η_{eff} the different focusing parameters are removed and agreement can only be attributed to the linewidth of the 1342nm resonator and the beam quality of the two interacting lasers. Since the 1342nm resonators are build using the same type of gain material the beam quality and linewidth are assumed to be comparable. The beam quality of the tapered EDCL can then be compared with the Ti:S laser since they all runs single frequency. The mode cleaning using the SMPM fibre is seen to drastically improve the performance and using this approach the conversion efficiency is actually slightly larger than the one found for the Ti:S laser, the drawback is though the loss of more than 50% of the output power from the Tapered ECDL.

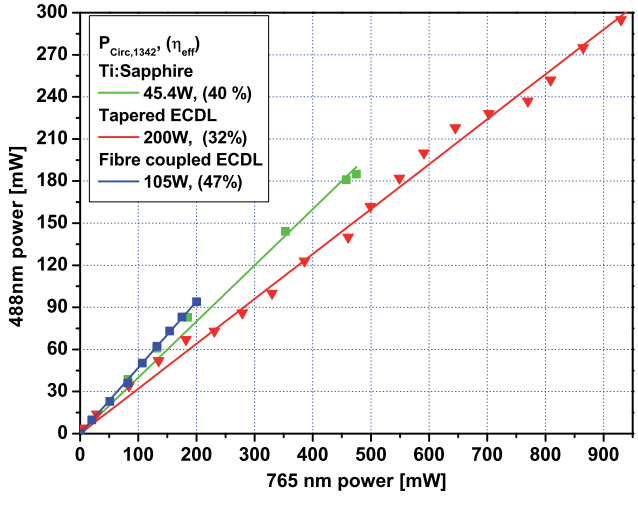

Figure 8.3: Conversion efficiency of the Ti:S laser compared with the tapered diode from the two experiments. Note the difference in the circulating power of the 1342nm resonators used.

The performance of the systems are summarised in table 8.1. It is clear that the theoretical calculations for the η_{eff} gives an overestimate compared to the measured value, especially for high M^2 values. As mentioned in chapter 2 the M^2 value is a simplified description of the beam quality and tells how well a beam can be focused. It does not tell how the actual spatial distribution of the actual beam is, and for the tapered diode a complex far field intensity distribution is observed.

A method to improve the spatial beam quality of the tapered diode can be to use feedback to the front facet in a configuration with a external output coupling mirror. The spatial filtering can be done using a pinhole inserted in a beamwaist formed between the front facet of the tapered diode and the mirror, though problem with hotspots inside the semiconductor material has to be considered. The tapered diode laser can also be build as the gain material in a ringlaser configuration, in this

way hotspots can be avoided and the unidirectional operation will enforces single frequency oscillation. Another method of filtering can be done using the nonlinear conversion, since the mixing process is a convolution of the two interacting beams the high order temporal components of tapered diode can be removed by weaker focusing of the beam compared to the beamsize of the 1342nm laser inside the PPKTP [91].

Table 8.1: Summary of the measured values for the single pass efficiencies and the conversion efficiencies for the three experiments.

Type	M_H^2/M_V^2 766nm	h_{eff}	η_{SP} %	η_{eff} W^{-1}	agreement %	$P_{\max}$ mW
ECDL	1.48/2.1	0.21	32	0.0018	29	300mW
Fibre	1.2/1.2	0.20	47	0.0046	80	94mW
Ti:S	(1/1)	0.36	40	0.0089	84	184mW

Chapter 9

SFG using SDL and DPSS 1342nm laser

In this chapter the performance of a sum frequency system comprising of a semiconductor disk laser(SDL) and a diode pumped solid state laser is investigated, the large tuning range of the SDL is investigated for the possibility of generating tunable visible light, finally a comparison between the performance of the systems described in the previous chapters and this work is made

This work has been published:

- *Singly-resonant sum frequency generation of visible light in a semiconductor disk laser*
  M. T. Andersen, P. J. Schlosser, J. E. Hastie, P. Tidemand-Lichtenberg, M. D. Dawson and C. Pedersen.
  Optics Express, Vol. **17**, Issue 8, 6010-6017, April 2009

- *Intracavity Frequency Mixing in a Semiconductor Disk Laser Generating >100mW in the Yellow-Orange*
  J. E. Hastie, **M. T. Andersen**, M. D. Dawson and P. Tidemand-Lichtenberg
  ASSP 2009, MB22, (Poster, abstract), January 2009)

9.1 Introduction

Intracavity SFG within a resonator using SDL as gain material has been demonstrated, here both wavelengths are generated within the laser cavity and LBO is used to generate SFG visible light [92]. In this chapter a generic approach for generation of visible light is investigated, here a hybrid approach based on SFG between a single pass near infrared(NIR) laser source and the intracavity field of a SDL is used. The approach is experimentally demonstrated through sum frequency mixing of a single pass Nd:YVO_4 solid state laser oscillating at 1342nm and an InGaAs based SDL with peak emission at 1064nm generating light at 593nm. In the following the experimental setup is described, including a characterisation of each of the two laser sources, followed by analysis of the nonlinear frequency conversion and the measured parameters of the generated light. One of the advantages of using SDL is the large tuning range and the possibility of broad wavelength tuning of the SFG light is discussed.

9.2 Setup

Figure 9.1 depicts the experimental configuration. The SDL is designed as a 4 mirror, z-folded cavity with an InGaAs SDL gain structure, similar in design and structure to that reported earlier [93], acting as a planar end mirror. The cavity mirrors M1, M2 and M3 are high reflectivity (HR) coated at 1064nm and high transmittance (HT) at 808nm, all mirrors has a radius of curvature of -100mm. In order to match the cavity mode to a pump spot size of 80μm at the SDL, the cavity arm lengths are set to be: 53mm, 457mm, and 156mm, respectively. An additional beam waist of $\approx 89\mu$m and $\approx 43\mu$m in the horizontal and vertical axis respectively, is located in the cavity arm, where the nonlinear crystal is positioned. For this experiment a 10mm Brewster cut periodically poled KTiOPO4 (PPKTP) crystal is used and the oblique angle is the reason for the relatively large waist size in the horizontal plane. The middle arm contained a three plate BiRefringent Filter (BRF) allowing for wavelength tuning of around 30nm, centred at an emission wavelength of 1055nm. 13W of optical pump power are incident at the SDL structure applied by an 808nm fibre coupled diode laser. At this power level a high heat load is introduced into the semiconductor structure and therefore a 500μm thick diamond heatspreader is liquid capillary bonded to the intracavity surface of the semiconductor for thermal management and the structure is kept at a temperature of 0 °C via a water/glycol cooled brass mount.

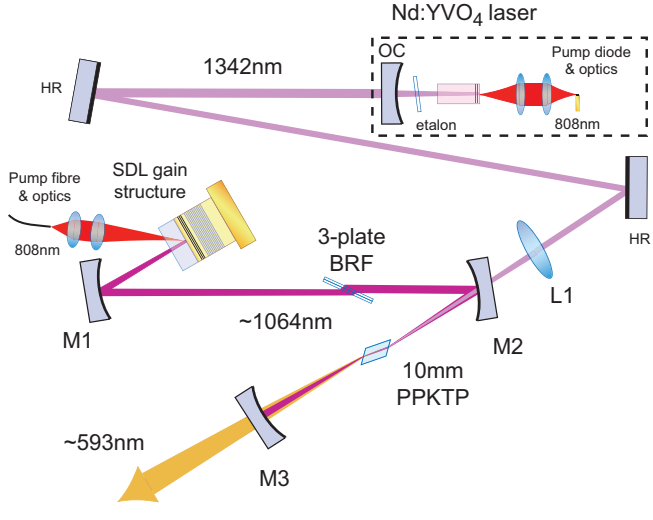

Figure 9.1: Experimental setup for generation of 593nm yellow orange light within a high finesse SDL cavity, including PPKTP at an intracavity focus and a single pass of the output beam of a diode pumped Nd:YVO_4 solid state laser. HR: high reflector; OC: output coupler; BRF: birefringent filter.

The single pass 1342nm beam is generated by an 8mm long a-cut Nd:YVO_4 crystal (0.5atm% Nd-doped), pumped by an 808nm 4W broad area laser diode. The pump end facet of the crystal is coated for HR and HT at 1342nm and 808nm respectively, whereas the intracavity facet is anti reflection (AR) coated at 1342nm.

The cavity is established between the HR coated facet and a 2% output coupler (OC) of -200mm radius of curvature. A 0.3mm thick intracavity etalon enabled wavelength tuning and line shape narrowing. The beam is aligned and focused into the PPKTP crystal by two plane steering mirrors and a lens L1 ($f = 120$mm, measured power transmittance at 1342nm 93%). The 1342nm beam is coupled into the PPKTP crystal through mirror M2, having a measured power transmittance of 87% at this wavelength. The sum frequency generated beam at 593nm is coupled out through the end mirror M3 with a measured power transmittance of 85%.

9.3 SDL characterisation

In order to achieve efficient sum frequency conversion, the fundamental power levels reaching the nonlinear crystal must be maximised, the spectrum of the fundamental fields must be within the spectral acceptance bandwidth of the nonlinear material, the state of polarisation of the fields must align with the highest possible second order susceptibility of the NLO material and the beam quality must be close to the fundamental TEM_{00} mode. SDLs have a significant gain bandwidth, allowing for broad tuning around their design wavelength, which typically leads to broadband emission. It is therefore necessary to introduce intracavity spectral filters to narrow and tune the emission spectrum. This is done by placing the three plate quartz BRF within the SDL cavity, plate thicknesses 4-, 2-, and 1- mm where the thickest BRF determines the filter resolution and the thinnest the spectral range [94]. Figure 9.2 (a) illustrates the measured SDL spectrum using the three plate BRF. The linewidth is measured to be less than 0.1nm (corresponding to 125 longitudinal cavity mode spacings), which is comparable to the linewidth achievable by a single 4mm BRF. The benefit of the three plate filter in this case is to suppress the additional peaks allowed by a single BRF, figure 9.2 (b), which broaden the emission spectrum, thus lowering the conversion efficiency. The separation of the additional peaks corresponds to the free spectral range (0.4nm) of the 500 μm thick diamond heatspreader.

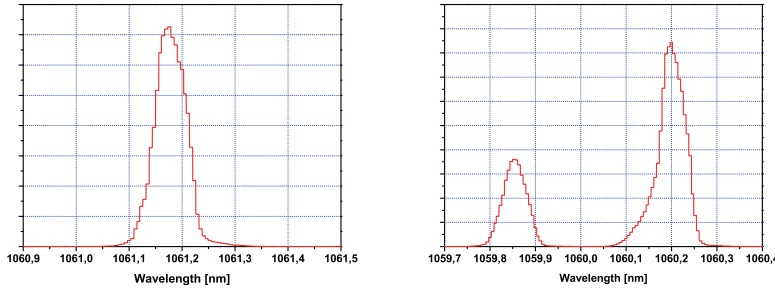

(a) **(b)**

Figure 9.2: Spectrum of the SDL: (a) using a three plate BRF. The spectral line width is <0.1nm, no additional peaks are seen using the three plate filter. (b) using a simple 4mm BRF.

To estimate the circulating power of the SDL cavity a partly reflecting(PR) mirror with a known transmission of $T = 2\%$ is positioned between the BRF filter and

mirror M2. The leakage power through mirror M1 is correlated with the output power of the PR mirror. The power transmittance is measured to 0.017%, and the circulating power in the SDL cavity is found to be approx 40W. The SDL is pumped by a 50W 808nm Limo fibre coupled broad area laser diode. The pump is fixed to an operating current of 16A delivering 16W of pump power, because of the diamond heatspreader approximately 17% of the power is reflected, leaving 13W of pump power incident on the SDL.

9.4 1342nm solid state laser

The 1342nm transition line of Nd:YVO_4 has a relatively narrow gain bandwidth compared to the SDL and therefore a thin intracavity etalon, in this case 0.3mm thick, is sufficient to ensure a spectral emission of less than 0.2nm (corresponding to 30 longitudinal mode spacings). The corresponding spectra and tuning range obtained by tilting the etalon are shown in figure 9.3 (a). The measured power performance is shown in figure 9.3 (b), for an emission wavelength of 1342.4nm, corresponding to the red line spectrum of figure 9.3 (a). The maximum output power of the Nd:YVO_4 laser is measured to 900mW at 1342.4nm, at high pump powers the 1342nm laser experience roll off this is due to thermal lensing in the Nd:YVO_4 crystal. Approximately 20% is lost via the two steering mirrors, the mode matching lens L1 and mirror M2, lowering the maximum input power incident of the nonlinear material to less than 700mW.

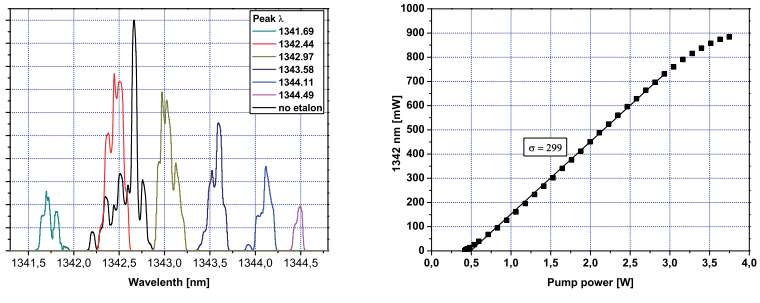

Figure 9.3: Characteristics of the 1342nm laser with intracavity 0.3mm thick etalon. (a) Output spectra obtained over the tuning range of the laser by means of tilting the etalon, and (b) slope efficiency at 1342.4nm at high pump powers the slope deviates from the linear slope.

The M^2 value of the 1342nm laser is measured at the position of the PPKTP. The values in the horizontal and vertical axis are measured to $M_H^2 = 1.42$ and $M_V^2 = 1.36$, which is slightly higher than expected based on previous measurements.

From the measured beam waists the focusing parameters are found for both lasers using equation 6.4 and setting the $M^2 = 1$ for the SDL laser:

$$\xi_H^{1064} = 0.12, \quad \xi_V^{1064} = 0.50$$
$$\xi_H^{1342} = 0.13, \quad \xi_V^{1342} = 0.54$$

The generalised Boyd Kleinman factor for the SFG is calculated for the horizontal and vertical plane to $h_m^h = 0.12$ and $h_m^v = 0.48$ giving $h_{eff} = 0.24$. In the optimum case setting $\xi = 2.84$ the beam waists are found to:

$$w_H^{1064} = 18.05\mu m, \qquad w_V^{1064} = 18.05\mu m$$
$$w_H^{1342} = 17.05\mu m\,(8.2\mu m)\,, \qquad w_V^{1342} = 17.42\mu m$$

The value in parenthesis is the optimum focusing for Brewster cut crystals. It is worth noting that the intracavity beamwaist is determined by the resonator design and from ABCD matrix calculations the horizontal beamwaist is fixed to values around $85 - 90\mu$m in order to obtain a stable resonator. A smaller beamwaist could be obtained by changing mirror M2 to a mirror with a smaller radius of curvature, though this would move the beamwaist closer to M2 and in the present setup this would be impossible, as the PPKTP and its oven would block the beam in arm 1. One possible solution could be to build a cavity setup similar to the one used in chapter 7 where the PPKTP is placed in the centre arm. The BRF filtering could then be placed in the arm between mirror M2 and M3.

9.5 Sum Frequency Generation

For efficient phasematching, the temperature of the PPKTP crystal could be controlled within the range 22 to 52 °C. In order to generate the data plotted in figure 9.4, the wavelengths of the SDL and single pass laser is kept fixed at 1063nm and 1342.4nm respectively, while the temperature of the PPKTP crystal is scanned through this temperature range. Optimum phasematching is found for a PPKTP temperature of 42 °C, which is in close agreement with that theoretically predicted value using the Sellmeier equations for KTP (PPKTP poling period 12.65μm) [86]. A maximum generation of 136mW at 593nm is obtained for a single pass power of 680mW incident on the PPPKTP crystal, this correspond to a conversion efficiency of 20% of the single pass 1342nm power. It is expected that the conversion efficiency of the system can be improved to more than 30% by reducing the spotsize of the 1064nm laser. An optimization of the polarisation extinction ratio which is measured to be approx 1/65, see figure 9.5 can invoke a minor improvement of the performance. The limited extinction ratio is due to the intrinsic unpolarised nature of the vertically emitting semiconductor gain region, and imperfections in the alignment of the many intracavity Brewster's surfaces, which also adds to the intracavity losses limiting the circulating power in the 1064nm cavity.

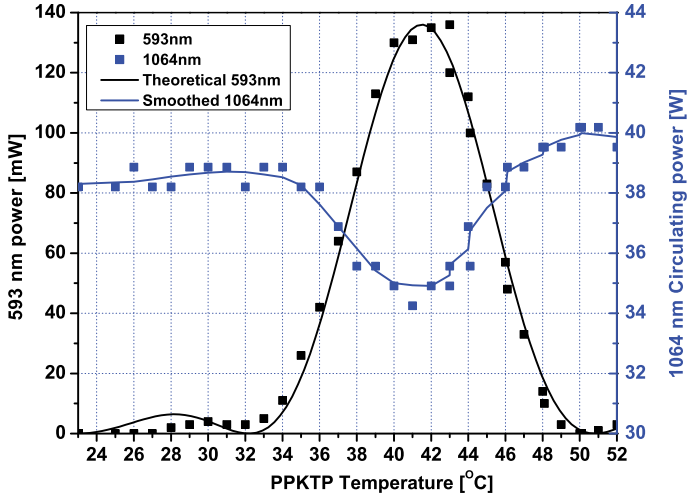

Figure 9.4: Measured phasematching temperature acceptance bandwidth of the PPKTP crystal shown as the generated output power at 593nm as a function of crystal temperature for a single pass 1342nm power of 680mW. Close agreement with the theoretical curve is seen. Also shown is the simultaneous measurement of circulating intracavity power at 1064nm. The data is averaged over 5 points using adjacent averaging.

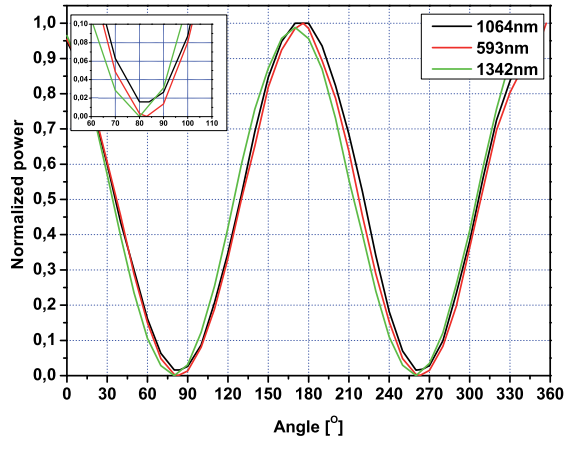

Figure 9.5: Polarisation characteristics of the fundamental and generated beams: measured power transmitted through a polarising beamsplitter cube as it is rotated 360^{circ}.

The generated power is shown as a function of single pass power in figure 9.6. The single pass power is varied using a HWP and a polarising beamspiltter, in this way the thermal load in the laser is constant throughout the whole experiment. It is worth noting the linear slope, even at low power levels, which is in strong contrast to second harmonic generation.

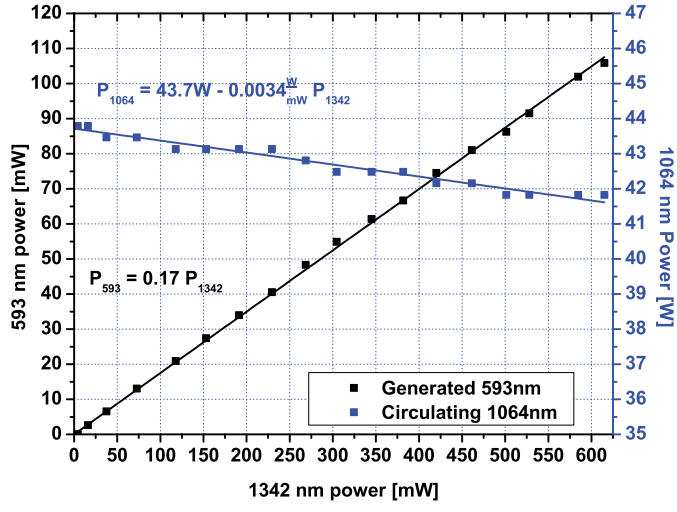

Figure 9.6: Generated output power at 593nm and intracavity circulating power at 1064nm as a function of single pass 1342nm power.

The slope for this measurement is 17%. From figure 9.4 and 9.6 the efficiency factor can be calculated to:

$$\eta_{eff}^{meas} \approx \frac{136\text{mW}}{35\text{W} \cdot 680\text{mW}} = 0.0057 \tag{9.1}$$

$$\eta_{eff}^{meas} \approx \frac{106\text{mW}}{42\text{W} \cdot 615\text{mW}} = 0.0041 \tag{9.2}$$

The theoretical estimate is found using equation 6.7 and the h_{eff}

$$\eta_{eff}^{theo} = 0.0195\text{W}^{-1} \cdot 0.24 = 0.0047\text{W}^{-1} \tag{9.3}$$

This shows that the measured value is close to the theoretical estimate under the given focusing condition and estimated beam qualities. If the polarisation ratio of the SDL 1064nm laser is taking into account the amount of circulating field that contribute to the nonlinear interaction the measured efficiency is increased slightly (0.0058 and 0.0041). The losses due to the conversion can be found to:

$$\alpha_{1064}^{SFG} = \frac{593\text{nm}}{1064\text{nm}} \cdot \frac{105\text{mW}}{42\text{W}} \approx 0.14\% \tag{9.4}$$

Using equation 6.11 an estimate of the passive losses in the SDL cavity is found to

$$\alpha_{1064}^{P} = \frac{42\text{W}}{44\text{W} - 42\text{W}} \cdot 0.14\% \approx 2.93\% \alpha_{1064}^{P} = \frac{42\text{W}}{44\text{W} - 42\text{W}} \cdot 0.14\% \approx 2.93\% \tag{9.5}$$

Which confirms that there are indeed high losses in the cavity compared to the 1342nm mixing modules used in the previous chapters and this is the reason for relatively low circulating field for a pump power of 13W.

9.6 Wavelength tuning

Wavelength tuning of the generated light is usually achieved by tuning the wavelength of the fundamental and changing the temperature of the nonlinear material to obtain phasematching. For SFG it is possible to change the wavelength of the two fundamentals independently with the possibility to obtain phasematching for minor changes of the temperature of the nonlinear crystal. This is investigated for the present system and as mentioned in the introduction, and demonstrated in [37], one of the interesting features of using semiconductor materials as gain media is the significant large gain bandwidth of these devices. To investigate the potential tuning range of a visible light source based on SFG in a SDL, a numerical model based on the temperature dependent Sellmeier equations for KTP [86, 95] and the available tuning range of the SDL, is written and the results are shown in figure 9.7. For comparison the same simulation is carried out for the common NLO crystal LBO [96], see appendix A.4 for the MatLab code.

In figure 9.7 (a) and (b) the dotted lines are iso-wavelength lines for the generated field; the line in the upper right corner corresponds to 600nm and the lower left line corresponds to 582nm. The blue crosses in figure 9.7 (a) and 9.8 indicate phasematching curves for PPKTP maintained at a fixed temperature of 18, 43 and 52 °C, respectively, and the solid blue lines indicate the possible tuning range of the 1342nm laser. In order for the nonlinear PPKTP crystal to accommodate phasematching over the entire tuning range available from the SDL, a temperature scan of more than 250 °C is needed. As shown, a wavelength tuning of less than 2nm/34 °C is achieved using PPKTP. Using type I phasematched LBO a numerical calculation shows that a wavelength tuning of almost 10nm in the generated field can be achieved by changing the LBO temperature 10 °C (see figure 9.7 (b)), however, using LBO compared to PPKTP reduces the nonlinear coefficient by almost one order of magnitude, thus reducing the overall conversion efficiency of the system. A magnified view of the indicated range in figure 9.7 (a) is shown in figure 9.8 with experimentally measured points that are seen to agree closely with theoretically predicted values.

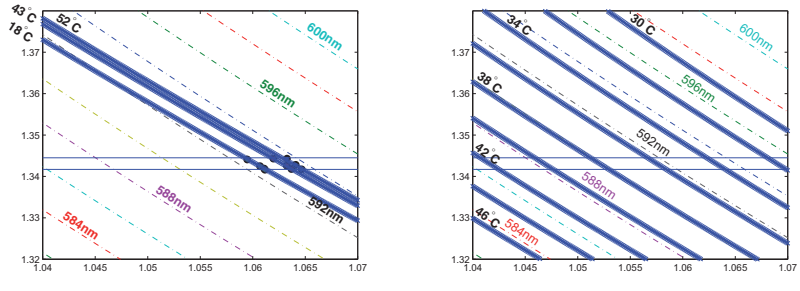

(a) (b)

Figure 9.7: Phasematching diagrams for sum frequency mixing between wavelengths centred around 1055nm and 1342nm for the full tuning ranges available from the lasers used. Dotted lines indicate iso-wavelength curves for the generated light, and blue crosses indicate phasematching curves for the nonlinear crystal at different temperatures. (a) for PPKTP at four different temperatures, from left to right 18, 43 and 52 °C, (b) for type I phasematched LBO.

It is clearly seen that dual wavelength tuning to allow a fixed temperature operation of the nonlinear material is not possible at the wavelengths investigated for the present setup. However, other wavelength ranges or alternative nonlinear materials with different dispersion relations would perhaps make dual wavelength tuning possible. Alternatively, chirped or fanned poling structures could enable significant tuning of such devices.

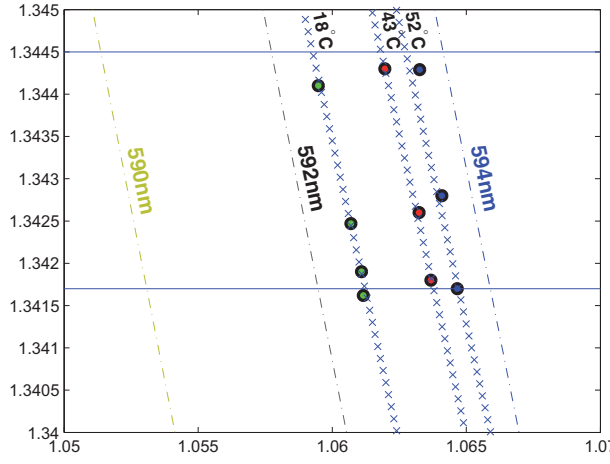

Figure 9.8: Zoom of the phasematching diagram for PPKTP, the green, red and blue points show measured data for PPKTP at 18, 43 and 52 °C.

9.7 Summary

A generic approach to visible light generation has been presented, using a semiconductor disk laser as one of two mixing lasers, allowing for generation of high power single frequency intracavity fields tunable over a broad range of wavelengths in the NIR (depending on the composition of the gain structure). Combining these devices with efficient quasi phasematched nonlinear crystals and single pass lasers delivering watts of power, it is in principle possible to generate hundreds of mW of SFG power anywhere in the visible spectrum with the possibility of tuning of the generated wavelength. However, if the full tuning potential of the SDL is to be transferred to the visible spectral region, tuning of the phasematch condition is needed, either using a fanned structure combined with mechanical movement or using a chirped structure at the expense of reduced efficiency. As demonstrated in this experimental realisation, 136mW of output power in the orange spectral range has been reached. Although this first demonstration has a lower efficiency compared to more mature systems based on two solid state lasers, the potential of using semiconductor disk lasers in combination with intracavity sum frequency mixing has been demonstrated.

In table 9.1 the measured values and the theoretical calculated η_{eff} for the four hybrid systems are shown. As mentioned in the previous chapter the theoretical

values gives a overestimate of the actual values for η_{eff}, which becomes more pronounced for increasing M^2 value. The value for the η_{eff} is seen to differ for SFG of 488nm and 593nm and is due to the difference for the interacting wavelengths.

Table 9.1: Summary of the measured values for the single pass efficiencies and the conversion efficiencies for the four experiments.

Type	M^2_H/M^2_V SP	h_{eff}	η_{SP} %	η_{SFG} W^{-1}	η_{eff} W^{-1}	agreement %	P_{max} mW
ECDL	1.48/2.1	0.21	32	0.0301	0.0018	29	300mW
Fibre	1.2/1.2	0.20	47	0.0301	0.0046	80	94mW
Ti:S	(1/1)	0.36	40	0.0301	0.0089	84	184mW
SDL	1.42/1.36	0.24	20	0.0195	0.0041	87	136mW

Chapter 10

Conclusion and Outlook

10.1 Conclusion

In this thesis the synthesise of any wavelengths in the visible and UV spectral region based on sum frequency generation have been sought based on a hybrid system combining solid state and semiconductor technology.

To reach the UV spectral region nonlinear materials with transparency range in the UV is required. Three GdCOB crystals with co-doping of lutetium and scandium has been investigated. Here the nonlinear coefficients for SHG of NIR light have been measured. The light is propagating along the **Y** axis of the crystals with the fundamental polarised along the **Z** direction. For $Gd_{0.871}Lu_{0.129}$ the nonlinear coefficient is found to be 0.78pm/V at a fundamental wavelength of 799nm. The temperature dependent acceptance bandwidth of the phasematching is measured to have a FWHM of 22.9K·cm using a 6mm long crystal. For $Gd_{0.93}Lu_{0.07}$ the nonlinear coefficient is measured to 0.81pm/V for a fundamental wavelength of 812nm, and the temperature dependent FWHM acceptance bandwidth is measured to 16.3K·cm. The third crystal is $Gd_{0.96}Sc_{0.04}$ for which a nonlinear coefficient of 0.89pm/V is found by second harmonic generation of 815nm and the temperature dependent FWHM is measured to 18.5K·cm. These nonlinear coefficients are comparable with the value for LBO ($d_{eff} = 0.75pm/V$), and the ability to obtain NCPM at a large range of wavelengths makes this crystals a promising candidate for nonlinear frequency conversion into the blue-UV spectral range for a number of applications.

A novel method for cavity dumping based on nonlinear frequency conversion has been investigated. The system comprises of a high finesse 1342nm cavity with a PPKTP crystal placed intracavity. The PPKTP is phasematched for SFG of 1342nm and 1064nm, and by single pass of a 1064nm pulse the intracaviy field is effectively dumped, and no backconversion is observed, which would be expected for the case where both lasers are single passed through the PPKTP. The origin for this is the dynamic of intracavity SFG, where the feedback of the excess circulating field to the SFG process and the roundtrip time of the cavity compared to pulse length has to be taken into account. Simulations indicates that a small amount of backconversion do occur, though since no attempt have been made to force single frequency operation and combined with the distortion of the spatial mode for the circulating field this is expected to reduce the backconversion even further. The

output power of this system is modest though the possibility of tailoring the system for other hard to reach wavelengths is huge, as demonstrated by generation of 340nm UV light based on this cavity dumping scheme. The process is done by cascading of SHG og the 1064nm pulsed laser then intracvity SFG in a 946nm Nd:YAG laser and the SHG 532nm pulse. The cascading process is also explored to generate 355nm by tripling the 1064nm Q-switched laser. This 355nm source is furthermore used for photo induced reactions.

In the investigated hybrid approach the single pass laser is exchanged with a semiconductor tapered diode laser, and more than 300mW of 488nm light is generated by intracavity SFG in a 1342nm high finesse cavity between the circulating 1342nm field and the single pass 766nm tapered diode. The single pass conversion efficiency was found to 32%, which is 27% of a theoretical estimate. This is compared to a system where the output of the tapered diode laser is spatial filtered using a single mode polarising maintaining fibre, and for this system the single pass conversion efficiency was found to 47%, which is 80% of a theoretical estimate. An all solid state system based on a single frequency Ti:S laser as the single pass laser was found to 40%, which is 84% of a theoretical estimate. From these values it is clear that further work for improving the spatial mode of the tapered diode can be made.

Another approach using semiconductor material is investigated, here the gain material of the high finesse cavity is exchanged with an optically pumped semiconductor disk laser oscillating at 1064nm. The single pass laser is a solid state 1342nm laser. The circulating field of the semiconductor disk laser was four times less than compared to the 300mW 488nm system, however, 136mW 593nm light is generated giving a single pass conversion efficiency of 20%, which is 87% of a theoretical estimate. Finally tuning of the SFG light has been investigated, though the phasematching conditions for the PPKTP crystal used in the experiment did not allow for large tuning, it is expected that using LBO as nonlinear material is better suited for tuning of the generated light.

10.2 Outlook

During the work with this project, many new ideas and further improvement of the conducted experiments has evolved. The limitation of this three year project means that many interesting suggestion and experiments could not be undertaken during this work. Therefore some of the most interesting suggestions for future experiments are listed below.

All semiconductor approach

Building a SDL high power laser with the nonlinear material placed intracavity, and mixing it with a tapered diode laser. This combination gives a high degree of freedom firstly with the desired wavelength secondly since both lasers can be tuned over a broad range, by appropriate choice on nonlinear material this would give an efficient compact tuneable light source at any wavelength in the visible and UV region. As an example a semiconductor disk laser with its centre wavelength around 1064nm has a tuning range of around 30nm, and a ECTDL oscillating at 766nm with a tuning range of 20nm could potentially give a total tuning range of the SFG light from around 437nm to 450nm.

Difference frequency generation

Difference frequency generation for generation of more than 100nm tuning range in the mid infrared using the same method as described above is also a very interesting experiment, the phasematching curves Lithium Tantalate bends in the mid infrared which gives a huge tuning range for a small change in temperature of the nonlinear crystal. Only a few efficient light sources exist in the mid infrared area and for gas sensing light sources in this area is highly sought.

The same setup as proposed for the SFG can be used to upconvert mid infrared light to the NIR or visible spectrum where effective detectors exist. In the mid infrared region high quantum efficiency detection usually require cryogenic temperatures of the detectors and are very costly. Furthermore detectors in this area have a very low detection efficiency, by converting the light to the visible spectrum standard low cost, easy to handle and very efficient detectors can be used.

Imaging

It is possible to transfer image using SFG, this has been demonstrated by Emir *et al.* in an article pending for publishing. The convolution between the image and the intracavity beam generate an upconverted image which will inherit the image of the single pass laser (if hard focused) convolved with a Gaussian intensity distribution inherit from the intracavity laser, under the assumption that it lases at TEM_{00} mode. Using computer algorithm the original image can be restored. The main advantage of this is that in situ measurement can be made of for example very hot gases, liquids where the intense heat would destroy probes in close contact. With this method measurement can be made at a safe distance and real time [91].

Bibliography

[1] Max Planck. Über irreversible Strahlungsvorgäng. *Sitzungsberichte der Königlich Preußischen Akademie der Wissenschaften zu Berlin*, pages 440–480, June 1899.

[2] Max Planck. Ueber das Gesetz der Energieverteilung im Normalspectrum. *Annalen der Physik*, 309(2):553–563, January 1901.

[3] Albert Einstein. Über einen die Erzeugung und Verwandlung des Lichtes betreffenden heuristischen Gesichtspunkt. *Annalen der Physik*, 322(6):132–148, March 1905.

[4] Albert Einstein. Zur quantentheorie der strahlung. *Physikalische Zeitschrift*, 18:121–128, 1917.

[5] J. P. Gordon, H. J. Zeiger, and C. H. Townes. Molecular Microwave Oscillator and New Hyperfine Structure in the Microwave Spectrum of NH_3. *Physical Review*, 95(1):282–284, July 1954.

[6] T. H. Maiman. Stimulated Optical Radiation in Ruby. *Nature*, 187:493–494, August 1960.

[7] Gordon Gould. The LASER, Light Amplification by Stimulated Emission Radiation. page 128, University of Michigan, June 1959. The Ann Arbor Conference on Optical Pumping.

[8] A. Javan, W. R. Bennett, and D. R. Herriott. Population Inversion and Continuous Optical Maser Oscillation in a Gas Discharge Containing a He-Ne Mixture. *Physical Review Letters*, 6(3):106–110, Feb 1961.

[9] R. N. Hall, G. E. Fenner, J. D. Kingsley, T. J. Soltys, and R. O. Carlson. Coherent Light Emission From GaAs Junctions. *Physical Review Letters*, 9(9):366–368, November 1962.

[10] I. Hayashi, M. B. Panish, and F. K. Reinhart. GaAs-$Al_xGa_{1-x}As$ Double Heterostructure Injection Lasers. *Journal of Applied Physics*, 42(5):1929–1941, September 1971.

[11] Gilbert N. Lewis, David Lipkin, and Theodore T. Magel. Reversible Photochemical Processes in Rigid Media. A Study of the Phosphorescent State. *Journal of the American Chemical Society*, 63(11):3005–3018, November 1941.

[12] P. A. Franken, A. E. Hill, C. W. Peters, and G. Weinreich. Generation of Optical Harmonics. *Physical Review Letters*, 7(4):118–119, August 1961.

[13] Robert C. Miller and Albert Savage. Harmonic Generation and Mixing of $CaWO_4$: Nd^{3+} and Ruby Pulsed Laser Beams in Piezoelectric Crystals. *Physical Review*, 128(5):2175–2179, December 1962.

[14] Gerard Aka, A. KahnHarari, D. Vivien, JM Benitez, F. Salin, and J. Godard. A new non-linear and neodymium laser self-frequency doubling crystal with congruent melting: $Ca_4GdO(BO_3)_3$(GdCOB). *European Journal of Solid State and Inorganic Chemistry*, 33(8):727–736, 1996.

[15] T. Baer. Large-amplitude fluctuations due to longitudinal mode coupling in diode-pumped intracavity-doubled Nd:YAG lasers. *JOSA. B*, 3(9):1175–1180, 1986.

[16] Peter Tidemand-Lichtenberg, Jirí Janousek, Radek Melich, Jesper L. Mortensen, and Preben Buchhave. Synchronization of 1064 and 1342 nm pulses using passive saturable absorbers. *Optics Communications*, 241(4-6):487 – 492, 2004.

[17] Jirí Janousek, Sandra Johansson, Peter Tidemand-Lichtenberg, Shunhua Wang, Jesper Mortensen, Preben Buchhave, and Fredrik Laurell. Efficient all solid-state continuous-wave yellow-orange light source. *Optics Express*, 13(4):1188–1192, Feburary 2005.

[18] Y. F. Chen. Design Criteria for Concentration Optimization in Scaling Diode End-Pumped Lasers to High Powers: Influence of Thermal Fracture. *IEEE Journal of Quantum Electronics*, 35(2):234–239, February 1999.

[19] A. Giesen, H. Hügel, A. Voss, K. Witting, U. Brauch, and H. Opower. Scalable concept for diode-pumped high-power solid-state lasers. *Applied Physics B*, 58(5):365–372, May 1994.

[20] Liguo Luo and P. L. Chu. Self-pulsation and bistability in a cw pumped erbium-doped fiber resonator system. *Optics Communications*, 135(1-3):116–120, 1997.

[21] Will Ray, Kurt Wiesenfeld, and Jeffrey L. Rogers. Refined fiber laser model. *Physical Review E (Statistical, Nonlinear, and Soft Matter Physics)*, 78(4):046203, 2008.

[22] Zhuang Zhuo, Tao Li, Xiaomin Li, and Hongzhi Yang. Investigation of Nd:YVO_4/YVO_4 composite crystal and its laser performance pumped by a fiber coupled diode laser. *Optics Communications*, 274:176–181, January 2007.

[23] Raphael Lavi, Steven Jackel, Yitshak Tzuk, Michael Winik, Eyal Lebiush, Mordechai Katz, and Idan Paiss. Efficient pumping scheme for neodymium-doped materials by direct excitation of the upper lasing level. *Applied Optics*, 38(36):7382–7385, 1999.

[24] W. P. Risk. Modeling of longitudinally pumped solid-state lasers exhibiting reabsorption losses. *JOSA B*, 5(7):1412–1423, 1988.

[25] D. H. Sutter, G. Steinmeyer, L. Gallmann, N. Matuschek, F. Morier-Genoud, U. Keller, V. Scheuer, G. Angelow, and T. Tschudi. Semiconductor saturable-absorber mirror assisted Kerr-lens mode-locked Ti:sapphire laser producing pulses in the two-cycle regime. *Optics Letter*, 24(9):631–633, 1999.

[26] Walter Kroechner. *Solid State Laser Engineering*. Optical Sciences. Springer, sixth edition, 2006.

[27] E. Fred Schubert. *Light-Emitting Diodes*. Cambridge University Press, second edition, 2003.

[28] B. Dahmani, L. Hollberg, and R. Drullinger. Frequency stabilization of semiconductor lasers by resonant optical feedback. *Optics Letters*, 12(11):876–878, 1987.

[29] K. C. Harvey and C. J. Myatt. External-cavity diode laser using a grazing-incidence diffraction grating. *Optics Letters*, 16(12):910–912, 1991.

[30] B. L. Volodin, S. V. Dolgy, E. D. Melnik, E. Downs, J. Shaw, and V. S. Ban. Wavelength stabilization and spectrum narrowing of high-power multimode laser diodes and arrays by use of volume Bragg gratings. *Optics Letters*, 29(16):1891–1893, 2004.

[31] J. N. Walpole. Semiconductor amplifiers and lasers with tapered gain regions. *Optical and Quantum Electronics*, 28(6):623–645, June 1996.

[32] Marc T. Kelemen, Juergen Weber, Michael Mikulla, and Guenter Weimann. High-power high-brightness tapered diode lasers and amplifiers. In Shibin Jiang and Michel J. Digonnet, editors, *Components and Materials II*, volume 5723, pages 198–208, San Jose, CA, USA, January 2005. SPIE.

[33] A. K. Goyal, P. Gavrilovic, and H. Po. Stable single-frequency operation of a high-power external cavity tapered diode laser at 780 nm. *Applied Physics Letters*, 71(10):1296–1298, 1997.

[34] Patrick Friedmann, Jurgen Gilly, Stefan Moritz, Ralf Ostendorf, and Marc T. Kelemen. 5 W frequency stabilized 976 nm tapered diode lasers. In Mark S. Zediker, editor, *High-Power Diode Laser Technology and Applications VI*, volume 6876, page 68761J. SPIE, 2008.

[35] Alexander Knitsch, Martin Traub, Karsten Rotter, Dieter Hoffmann, Peter Loosen, and Reinhart Poprawe. Characterization of tapered diode laser bars for the use in high-power diode laser systems. volume 5336, pages 56–64. SPIE, 2004.

[36] A. R. Zakharian, J. Hader, J. V. Moloney, S. W. Koch, P. Brick, and S. Lutgen. Experimental and theoretical analysis of optically pumped semiconductor disk lasers. *Applied Physics Letters*, 83(7):1313–1315, 2003.

[37] Stephane Calvez, Jennifer E. Hastie, Mircea. Guina, Oleg G. Okhotnikov, and Martin D. Dawson. Semiconductor disk lasers for the generation of visible and ultraviolet radiation. *Laser & Photonics Review*, pages 1–28, January 2009.

[38] Robert W. Boyd. *Nonlinear Optics*. Academic Press, 525 B Street, Suite 1900, San Diego, CA 92101-4495, USA, third edition, 2008.

[39] D. A. Kleinman. Nonlinear Dielectric Polarization in Optical Media. *Physical Review*, 126(6):1977–1979, June 1962.

[40] G. D. Boyd and D. A. Kleinman. Parametric Interaction of Fucused Gaussian Light Beams. *Journal of Applied Physics*, 39(8):3597–3639, July 1968.

[41] S. E. Harris, M. K. Oshman, and R. L. Byer. Observation of Tunable Optical Parametric Fluorescence. *Physical Review Letters*, 18(18):732–734, May 1967.

[42] R. L. Byer and S. E. Harris. Power and Bandwidth of Spontaneous Parametric Emission. *Physical Review*, 168(3):1064–1068, April 1968.

[43] Y.-S. Lee, T. Meade, V. Perlin, H. Winful, T. B. Norris, and A. Galvanauskas. Generation of narrow-band terahertz radiation via optical rectification of femtosecond pulses in periodically poled lithium niobate. *Applied Physics Letters*, 76(18):2505–2507, May 2000.

[44] C. Weiss, G. Torosyan, Y. Avetisyan, and R. Beigang. Generation of tunable narrow-band surface-emitted terahertz radiation in periodically poled lithium niobate. *Optics Letters*, 26(8):563–565, April 2001.

[45] J.A. Armstrong, N. Bloembergen, J. Ducuing, and P.S. Pershan. Interactions between light waves in a non-linear dielectric. *Physical Review*, 127(6):1918–1939, 1962.

[46] Bahaa E. A. Saleh and Malvin Carl Teich. *Fundamentals of Photonics*. Pure and Applied Optics. Wiley, 2nd edition edition, 2007.

[47] Makoto Iwai, Taisuke Kobayashi, Hiroyuki Furuya, Yusuke Mori, and Takatomo Sasaki. Crystal Growth and Optical Characterization of Rare-Earth (Re) Calcium Oxyborate $ReCa_4O(BO_3)_3$ (Re = Y or Gd) as New Nonlinear Optical Material. *Japanese Journal of Applied Physics*, 36(Part 2, No. 3A):L276–L279, 1997.

[48] H. Furuya, M. Yoshimura, T. Kobayashi, K. Murase, Y. Mori, and T. Sasaki. Crystal growth and characterization of $Gd_xY_{1-x}Ca_4O(BO_3)_3$ crystal. *Journal of Crystal Growth*, 198-199(Part 1):560 – 563, 1999.

[49] V. G. Dmitriev, G. G. Gurzadyan, and D. N. Nikogosyan. *Handbook of Nonlinear Optical Crystals*, volume 64 of *Optical Science*. Springer, third revised edition, February 1999.

[50] G. D. Boyd and C. K. N. Patel. Enhancememt of optical second-harmonic generation (SHG) by reflection phase matching in ZnS and GaAs. *Applied Physics Letters*, 8(12):313–315, June 1966.

[51] Duan Feng, Nai-Ben Ming, Jing-Fen Hong, Yong-Shun Yang, Jin-Song Zhu, Zhen Yang, and Ye-Ning Wang. Enhancement of second-harmonic generation in $LiNbO_3$ crystals with periodic laminar ferroelectric domains. *Applied Physics Letters*, 37(7):607–609, October 1980.

[52] Jr. C. F. Dewey and L. O. Hocker. Enhanced nonlinear optical effects in rotationally twinned crystals. *Applied Physics Letters*, 26(8):442–444, April 1975.

[53] M.M. Fejer, G.A. Magel, D.H. Jundt, and R.L. Byer. Quasi-phase-matched second harmonic generation: tuning and tolerances. *IEEE Journal of Quantum Electronics*, 28(11):2631–2654, November 1992.

[54] Keren Fradkin-Kashi and Ady Arie. Multiple-Wavelength Quasi-Phase-Matched Nonlinear Interactions. *IEEE Journal of Quantum Electronics*, 35(11):1649–1656, 1999.

[55] Alon Bahabad, Oren Cohen, Margaret M. Murnane, and Henry C. Kapteyn. Quasi-periodic and random quasi-phase matching of high harmonic generation. *Optics Letters*, 33(17):1936–1938, September 2008.

[56] Alon Bahabad, Noa Voloch, Ady Arie, and Ron Lifshitz. Experimental confirmation of the general solution to the multiple-phase-matching problem. *Journal of the Optical Society of America B*, 24(8):1916–1921, August 2007.

[57] A. Bahabad, N. Voloch, and A. Arie. Analysis of Colinear Quasi-Phase-Matching in Nonlinear Photonic Crystals. *Quantum Electronics, IEEE Journal of*, 44(7):638–644, July 2008.

[58] Ron Lifshitz, Ady Arie, and Alon Bahabad. Photonic Quasicrystals for Nonlinear Optical Frequency Conversion. *Phys. Rev. Lett.*, 95(13):133901, Sep 2005.

[59] M. Baudrier-Raybaut, R. Haïdar, Ph. Kupecek, Ph. Lemasson, and E. Rosencher. Random quasi-phase-matching in bulk polycrystalline isotropic nonlinear materials. *Nature*, 432(7015):374–376, November 2004.

[60] Y. Cui, M. H. Dunn, C. J. Norrie, W. Sibbett, B. D. Sinclair, Y. Tang, and J. A. C. Terry. All-solid-state optical parametric oscillator for the visible. *Optics Letters*, 17(9):646–648, 1992.

[61] Malcolm H. Dunn and Majid Ebrahimzadeh. Parametric Generation of Tunable Light from Continuous-Wave to Femtosecond Pulses. *Science*, 286(5444):1513–1517, 1999.

[62] Graham A. Turnbull, David J.M. Stothard, Majid Ebrahimzadeh, and Malcolm H. Dunn. Transient dynamics of CW intracavity singly resonant optical parametric oscillators. *IEEE Journal of Quantum Electronics*, 35(11):1666–1672, November 1999.

[63] Peter Tidemand-Lichtenberg, Knud Palmelund Sø rensen, Martin Thalbitzer Andersen, Preben Buchhave, and Christian Pedersen. Theoretical comparison of SHG and SFG efficiencies and stability. In *EOSAM - TOM 1: Biophotonics*, volume TOM 1. EOS, 2008.

[64] Zhengping Wang, Xinguang Xu, Kun Fu, Renbo Song, Jiyang Wang, Jingqian Wei, Yaogang Liu, and Zongshu Shao. Non-critial phase matching of $Gd_xY_{1-x}Ca_4O(BO_3)_3$($Gd_xY_{1-x}COB$) crystal. *Solid State Communications*, 120(9-10):397–400, November 2001.

[65] Lucian Gheorghe, Voicu Lupei, Pascal Loiseau, Gerard Aka, and Takunori Taira. Second-harmonic generations of blue light in nonlinear optical crystals of $Gd_{1-x}Lu_xCa_4O(BO_3)_3$ and $Gd_{1-x}Sc_xCa_4O(BO_3)_3$ through noncritical phase matching. *JOSA. B*, 23(8):1630–1634, August 2006.

[66] Martin Thalbitzer Andersen, Jesper Liltorp Mortensen, Sven Germershausen, Peter Tidemand-Lichtenberg, Preben Buchhave, Lucian Gheorghe, Voicu Lupei, Pascal Loiseau, and Gerard Aka. First measurement of the nonlinear

coefficient for Gd_{1-X} Lu $_XCa_4O(BO_3)_3$ and $Gd_{1-X}Sc_XCa_4O(BO_3)_3$ crystals. *Optics Express*, 15(8):4893–4901, April 2007.

[67] Emilie Herault, François Balembois, and Partick Georges. 491 nm generation by sum-frequency mixing of diode pumped neodymium lasers. *Optics Express*, 13(15):5653–5661, July 2005.

[68] Sandra Johansson, Shunhua Wang, Valdas Pasiskevicius, and Fredrik Laurell. Compact 492-nm light source based on sum-frequency mixing. *Optics Express*, 13(7):2590–2595, April 2005.

[69] Y. F. Chen, Y. S. Chen, and S. W. Tsai. Diode-pumped Q-switched laser with intracavity sum frequency mixing in periodically poled KTP. *Applied Physics B*, 79(2):207–210, July 2004.

[70] R. Mildren, M. Convery, H. Pask, J. Piper, and T. Mckay. Efficient, all-solid-state, Raman laser in the yellow, orange and red. *Optics Express*, 12(5):785–790, 2004.

[71] H. M. Pask and J. A. Piper. Efficient all-solid-state yellow laser source producing 1.2-W average power. *Optics Letters*, 24(21):1490–1492, November 1999.

[72] Z. Gürkan Figen and Orhan Aytür. Nanosecond sum-frequency generating optical parametric oscillator using simultaneous phase matching. *Opt. Express*, 13(13):4896–4902, June 2005.

[73] Hong-xia Li, Ping Xu, Ya-xian Fan, Peng Lu, Zhi-da Gao, Sheng Liu, Shi-ning Zhu, and Jing-liang He. All-solid-state red and green laser by temperature tuning. *Journal of Physics D: Applied Physics*, 37(17):L21–L24, August 2004.

[74] H. Statz, G. A. DeMars, D. T. Wilson, and C. L. Tang. Problem of Spike Elimination in Lasers. *Journal of Applied Physics*, 36(5):1510–1514, May 1965.

[75] M. Ramaswamy, M. Ulman, J. Paye, and J. G. Fujimoto. Cavity-dumped femtosecond Kerr-lens mode-locked Ti:Al_2O_3 laser. *Optics Letters*, 18(21):1822–1824, 1993.

[76] G. N. Gibson, R. Klank, F. Gibson, and B. E. Bouma. Electro-optically cavity-dumped ultrashort-pulse Ti:sapphire oscillator. *Opt. Lett.*, 21(14):1055–1057, July 1996.

[77] A. W. Tucker, M. Birnbaum, C. L. Fincher, and J. W. Erler. Stimulated-emission cross section at 1064 and 1342 nm in Nd:YVO_4. *Journal of Applied Physics*, 48(12):4907–4911, 1977.

[78] Yushi Kaneda and Shigeo Kubota. Continuous-wave 355-nm laser source based on doubly resonant sum-frequency mixing in an external resonator. *Optics Letters*, 20(21):2204–2206, November 1995.

[79] A. H. Kung, Lee Jr-i, and Poe-Jou Chen. An efficient all-solid-state ultraviolet laser source. *Applied Physics Letters*, 72(13):1542–1544, March 1998.

[80] H. Kitano, K. Sato, N. Ushiyama, M. Yoshimura, Y. Mori, and T. Sasaki. Efficient 355-nm generation in CsB_3O_5 crystal. *Optics Letters*, 28(4):263–265, February 2003.

[81] Donald J. Burton and Richard M. Flynn. A Facile Synthesis of Trifluoromethane- and Pentafluorobenzenephosphonates. *Communications*, 1979:615, August 1979.

[82] Larry Takemoto and Christopher M. Sorensen. Protein-protein interactions and lens transparency. *Experimental Eye Research*, 87(6):496–501, September 2008.

[83] M. J. Davies and R. J. Truscott. Photo-oxidation of proteins and its role in cataractogenesis. *Journal of Photochemistry and Photobiology B: Biology*, 63(1-3):114–125, July 2001.

[84] Mingjun Chi, Ole Bjarlin Jensen, Jesper Holm, Christian Pedersen, Peter Eskil Andersen, Götz Erbert, Bernd Sumpf, and Paul Michael Petersen. Tunable high-power narrow-linewidth semiconductor laser based on an external-cavity tapered amplifier. *Optics Express*, 13(26):10589–10596, December 2005.

[85] Shekhar Guha and Joel Falk. The effects of focusing in the three-frequency parametric upconverter. *Journal of Applied Physics*, 51(1):50–60, January 1980.

[86] Kato K. Temperature Insensitive SHG at 0.531 μm in KTP. *Quantum Electronics*, 28(10):1974, October 1992.

[87] Teunis W. Tukker, Cees Otto, and Jan Greve. Elliptical-focusing effect on parametric oscillation and downconversion. *JOSA. B*, 15(9):2455–2461, September 1998.

[88] Keren Fradkin-Kashi, Ady Arie, A. Skliar, and G. Resonman. Tunable mid-infrared source by difference frequency generation in bulk periodically poled $KTiOPO_4$. *Applied Physics Letters*, 74(7):914–916, February 1999.

[89] Shai Emanueli and Ady Arie. Temperature-Dependent Dispersion Equations for $KTiOPO_4$ and $KTiOAsO_4$. *Applied Optics*, 42(33):6661–6665, November 2003.

[90] Preben Buchhave and Peter Tidemand-Lichtenberg. Generation of higher order Gauss-Laguerremodes in single-pass 2nd harmonic generation. *Optics Express*, 16(22):17952–17961, 2008.

[91] Emir Karamehmedović, Christian Pedersen, Ole Bjarling Jensen, and Peter Tidemand-Lichtenberg. Nonlinear beam clean-up using resonantly enhanced sum-frequency mixing. *Applied Physics B*, May 2009.

[92] A. Härkönen, J. Rautiainen, T. Leinonen, Y.A. Morozov, L. Orsila, M. Guina, M. Pessa, and O.G. Okhotnikov. Intracavity Sum-Frequency Generation in Dual-Wavelength Semiconductor Disk Laser. *Photonics Technology Letters, IEEE*, 19(19):1550–1552, October 2007.

[93] Jun-Youn Kim, Soohaeng Cho, Junho Lee, Gi Bum Kim, Seong-Jin Lim, Jaeryung Yoo, Ki-Sung Kim, Sang-Moon Lee, Jongin Shim, Taek Kim, and Yongjo Park. A Measurement of Modal Gain Profile and Its Effect on the Lasing Performance in Vertical-External-Cavity Surface-Emitting Lasers. *Photonics Technology Letters, IEEE*, 18(23):2496–2498, December 2006.

[94] D. R. Preuss and J. L. Gole. Three-stage birefringent filter tuning smoothly over the visible region: theoretical treatment and experimental design. *Applied Optics*, 19(5):702–710, March 1980.

[95] Herman Vanherzeele, John D. Bierlein, and F. C. Zumsteg. Index of refraction measurements and parametric generation in hydrothermally grown $KTiPO_4$. *Applied Optics*, 27(16):3314–3316, 1988.

[96] K. Kato. Temperature-tuned 90° phase-matching properties of LiB_3O_5. *Quantum Electronics, IEEE Journal of*, 30(12):2950–2952, December 1994.

Appendix A

MatLab code

A.1 Relaxation Osscilation

```
%------------------------------ rateslover.m ------------------------------
close all;
clear all;

%constants
c = 299792458; % [m/s] speed of light
h = 6.6260755E-34; % [J*s] planck's constant

%laser properties
Tsp = 90E-6; % [s] spontaneous emission Nd:YVO
sigma = 6.0E-23; % [m^2] stimulated emission cross section Nd:YVO
Lambda = 1342E-9; % [m] lasing wavelength
Lpump = 808E-9; % [m] pump wavelength
Ep = h*c/Lpump; % [J] pump photon energy
El = h*c/Lambda; % [J] laser photon energy

%cavity
Lcav = 0.432; % [m] cavity length
Trt = 2*Lcav/c; % [s] roundtrip time
Lcry = 8E-3; % [m] laser crystal length
n = 2.2; % refractive indices Nd:YVO
% cavity losses
Tout = 0.00046
Lp = 0.0047
%Tout = 0.005; % output coupling
%Lp = 0.009; % other passive losses
Tp = 2*(n*Lcry + Lcav)/(c*(-log(1-Tout-Lp)));


%variables
Wpump = 350E-6; % [m] waist of pump
Wlaser = 190E-6; % [m] waist of laser
Power = 3.5; % [W] power of pump laser
npump = Power/Ep % [1/s] photons pr second
V = Lcry*pi*(Wpump)^2; % [m^3] volume

S = 10E-4/Tsp; % [1/s] Spontaneous emission decay to laser mode
Wi = sigma*c*Lcry/Lcav; % [m^3/s] Stimulated emission constant

%efficiencies
nq = Lpump/Lambda; %quantum efficiency
nm = 1; %Wlaser^2/Wpump^2; %modeoverlab
na = 0.58; %total absorption
etatot = na*nm; %total efficiencies
R = etatot*npump/V; % [1/(m^3*s)] Pumprate
Rt = 1/(Wi*Tp*Tsp); % [1/(m^3*s)] Threshold Pumprate
r=R/Rt; % pumpratio (times above Threshold Pumprate
```

```
%steady state values
n2SS = 1/(Wi*Tp); % upper state population
pSS = (R*Wi*Tp-1/Tsp)/Wi; % photon density
BP = pSS*c*pi*Wlaser^2*El*Lcry/Lcav; % power circulating field

%measured data
data = dlmread('pulsedata.txt');

%initial conditions
n20 = n2SS ; % [1/(m^3)] population in upper laser level
p0 = pSS ; % [1/m^3] photons in cavity

conditions = [n20,p0,R,1/Tsp,1/Tp,Wi,S]
%conditions2 = [1,1,30,0.01,30,3,0]

%Laser switch on until steady state
[T1,Y1] = ode45(@rateeq,[0 9E-6],conditions);

%photon dumped
conditions = [Y1(end,1),Y1(end,2),R,1/Tsp,1/Tp,Wi,S]
[T2,Y2] = ode45(@rateeq,[9E-6 13E-6],conditions);

conditions = [Y2(end,1),Y2(end,2),R,1/Tsp,1/Tp,Wi,S]
[T3,Y3] = ode45(@rateeq,[13E-6 100E-6],conditions);

T=[T1;T2;T3];
Y= [Y1;Y2;Y3];
Y(:,2) = Y(:,2)*c*pi*Wlaser^2*El*Lcry/Lcav; %converting to power
Y(:,2) = Y(:,2)/Y(1,2); %normalising to steady state
T = T*1E6; % scaling to micro seconds

alpha = r/(2*Tsp*1E+6); % [1/mu s] average damping coefficient
damping = exp(-alpha*(T-35)); % damping term
wm=sqrt(1/(Tsp*Tp*1E+12)*(r-1)-alpha^2)% [1/mu s]avg. oscillation frequency
swing = cos(wm*(T-35)); % Osscilation

% plot routines
BP
plot(T,Y(:,1))
figure

%plot(data(:,1),data(:,2),'r')
%hold on
plot(T,Y(:,2))
%hold on
%plot(T,1+damping.*swing,'r')
axis([0 100 0 9])

%------------------------------ rateeq.m ------------------------------
function dn = rateeq(t,n)
% n = [n20 p0 R 1/Tsp 1/Tp Wi S]

dn = zeros(6,1)

dn(1) = n(3) - n(4)*n(1) - n(6) * n(1)*n(2) % upper state
dn(2) = -n(5)*n(2) + n(6) * n(1)*n(2) + n(7)*n(1) % photon flux
dn(3) = 0
dn(4) = 0
dn(5) = 0
dn(6) = 0
dn(7) = 0
```

A.2 Nonlinear Conversion

```
%------------------------ conversionpulse.m ---------------------------------
close all;
clear all;

%Universal constants
hbar = 6.6262E-34/(2*pi); % [J*s]
C = 2.9979E+8; % [m/s]
e0 = 8.8542E-12; % [F/m]
u0 = 1.2566E-6; % [H/m]
imp0 = sqrt(u0/e0); % [ohm] impedance

%initial beam conditions
A=pi*(70E-6)^2; % [m^2] spotsize for beam in PPKTP
n = 1.8; % refractive index (close)

%efficiency terms
mm = [0.5 0.7 0.8 0.9 1]; % modeoverlap
%ellipticity for the two beams are in opposite directions

%beam = [lambda,power,phase] mm,W,rad,m^2
b1 = [1064E-9, 1, 0]; % pulsed laser
b2 = [1342E-9, 50, 0]; % 1342nm cavity
b3 = [b1(1)*b2(1)/(b1(1)+b2(1)), 0, 0]; % SFG beam
res = 200; % resolution
x = exp(-linspace(-5,5,res).^2); %gaussian pulse to 1E-11
% peak power vector
powervector = [6 10 100 200 300 400 500 600 700 900 1000 1500 ...
    2000 2400 6000]; % [W]

% nondepletion 0 = no depletion, 1 = normal depletion
dp = [1 1 1];% nondepletion vector

trt = 2*(0.008*2.2+0.432)*1E+9/C; % [ns] roundtrip time
width = 7; % [ns] pulse width

% crystal setup
lc = 0.063E-3; % [m] coherence length giving poling period at 12.6 mym
dz = 0.001E-3; % [m] step size through crystal
Lc = [0:dz:20E-3]; % [m] crystal length PPKTP
d33 = 15E-12; % [m/V] nonlinear coefficient PPKTP
d32 = 2.65E-12; %[m/V] highest non d33 coefficient
deff = 2*d33/pi; % [m/V] efficient QPM nonlinear coefficient

g=sqrt((2*pi)^3*2*hbar*C^3*imp0^3*e0^2/(n^3*b1(1)*b2(1)*b3(1)));

% number of times before circulating field is returned
runde = ceil(trt*res*sqrt(log(2))/(5*width));
% vector fixing the circulating field for feedback
%fix = ones(1,res);
fix = [ones(1,runde) linspace(2,res+1-runde,res-runde)];
for power = 1 : length(powervector)
    text1 = int2str(powervector(power));
    for mode = 1 : length(mm)
        %scaling to flux density for the pulse
        a10 = sqrt(powervector(power)*x*b1(1)/(hbar*C*2*pi*A))*exp(i*b1(3));
        a20 = sqrt(b2(2)*b2(1)/(hbar*C*2*pi*A))*exp(i*b2(3));
        a30 = sqrt(b3(2)*b3(1)/(hbar*C*2*pi*A))*exp(i*b3(3));
        text2 = num2str(mm(mode));
        Pa = []; % resetting the wave development vector
        for p =1 : length(x)
          a = [a10(p) a20 a30];
          for count=1 : length(Lc)-1
              da = nonlinear(a(count,:),dz,Lc(count),g*deff,0,dp,mm(mode));
              a(count+1,:) = a(count,:) + da;
          end
         % Rescaling to power from a
         Pa = [Pa; a(end,:)];
         a20 = Pa(fix(p),2);
         p
         end
         % scaling Pa to watts [W]
```

```
        Pa = A*hbar*C*2*pi*abs(Pa).^2;
        Pa(:,1) = Pa(:,1)/b1(1);
        Pa(:,2) = Pa(:,2)/b2(1);
        Pa(:,3) = Pa(:,3)/b3(1);
        text = [text1 'WMode' text2 '.txt']
        % saving data in the format xxxxWModexx.txt
        dlmwrite(text, Pa, 'delimiter', '\t','precision', 15)
    end
end
```

```
%------------------------------ nonlinear.m ------------------------------
function da = nonlinear(a,dz,z,g,DeltaK,dp,nmm)
%NONLINEAR Summary of this function goes here
%   Detailed explanation goes here

da1 = -i*g*nmm*a(3)*conj(a(2))*exp(-i*DeltaK*z)*dz;
da2 = -i*g*nmm*a(3)*conj(a(1))*exp(-i*DeltaK*z)*dz;
da3 = -i*g*nmm*a(1)*a(2)*exp(i*DeltaK*z)*dz;

da = [da1 da2 da3].*dp;
```

```
%------------------------------ plotpulse.m ------------------------------
close all;
clear all;

P = dlmread('6WMode1.txt');

C = 2.9979E+8; % [m/s]
res = 200; % resolution
width = 7; % [ns] pulse width
trt = 2*(0.008*2.2+0.432)*1E+9/C; % [ns] roundtrip time

% plot routines
xakse = linspace(0,5*width/sqrt(log(2)),res); %setting time axis
plot(xakse,P(:,2)/max(P(:,2)),'k','Linewidth',2)
hold on
plot(xakse,P(:,1)/max(P(:,1)),'r','Linewidth',2)
plot(xakse,P(:,3)/max(P(:,3)),'g','Linewidth',2)
hold off
grid on
% setting font size ect for the plot
axis([0 xakse(end) 0 1.05])
legend('1342nm','1064nm','  593nm','Location','SouthEast')
set(legend,'FontSize',12,'fontweight','b')
set(gca,'XTick',0:5:40,'YTick',0:0.1:1,'FontSize',14,'fontweight','b')
xlabel('Time [ns]','fontsize',14,'fontweight','b')
ylabel('Normalised power','fontsize',14,'fontweight','b')

% plotting roundtrip lines
%antal = floor(xakse(end)/trt)
%for count = 1 : antal
%    line([trt*count trt*count],[0 100],'linestyle',':')
%end
```

```
%------------------------------ Saturation.m ------------------------------
close all;
clear all;

C = 2.9979E+8; % [m/s]
res = 200; % resolution
width = 7; % [ns] pulse width
trt = 2*(0.008*2.2+0.432)*1E+9/C; % [ns] roundtrip time
xakse = linspace(0,5*width/sqrt(log(2)),res);
dx = xakse(2)-xakse(1);
%mode = '1';
powervector = [6 10 100 200 300 400 500 600 700 900 1000 1500 ...
    2000 2400 6000];
mode = [0.1 0.2 0.3 0.4 0.5  0.7 1];
energy = [];
peak = [];

for p = 1 : length(powervector)
    for m = 1 : length(mode)
```

```
            text1 = int2str(powervector(p));
            text2 = num2str(mode(m));
            P = dlmread([text1 'WMode' text2 '.txt']);
            energy(p,m) = sum(P(:,3))*dx;
            peak(p,m) = max(P(:,3));
        end
    end

% plot routines
plot(powervector',energy,'Linewidth',2)
set(gca,'FontSize',14,'fontweight','b')
xlabel('1064nm peak power [W]','fontsize',14,'fontweight','b')
ylabel('593nm SFG pulse energy [nJ]','fontsize',14,'fontweight','b')
grid on
legend
figure
plot(powervector',peak,'Linewidth',2)
set(gca,'FontSize',14,'fontweight','b')
xlabel('1064nm peak power [W]','fontsize',14,'fontweight','b')
ylabel('593nm SFG peak power [W]','fontsize',14,'fontweight','b')
grid on
legend
```

A.3 Efficiency factor η_{eff}

```
%------------------------------ focussingle.m ---------------------------------
close all
clear all

% the boyd kleinmann factor is found using the approach from guha article
% Journal of applied physics 51(1) january 1980

%the beam waist factor from Tukker josa B 15(9) 1998

%integration factors
xmin = 0;
xmax = 1;
ymin = 0;
ymax = 1;

%constants
c =299792458 ;
e0 = 8.8541878176204E-12;
deff = 15.4 * 2/pi*1E-12;
%plane 1 = h 2 = v
plane = [1 2];
% interaction length
l = 10000; % mu m
DKl = linspace(0,5,100);

% wavelength
lambda1 = 1.342; % mu m
lambda2 = 0.766; % mu m
lambda3 = lambda1*lambda2/(lambda1+lambda2); % mu m
lambda = [lambda1 lambda1 lambda2 lambda2];
n1 = sellmeier(43,1,lambda1);
n1 = n1(3);
n2 = sellmeier(43,1,lambda2);
n2 = n2(3);
n3 = sellmeier(43,1,lambda3);
n3 = n3(3);

kj = 2*pi * [n1 n1 n2 n2]./lambda;
kj3 = 2*pi*n3/lambda3;
%beam waist horizontal and vertical
Waist = [63 54 49 15];
%Waist = [18.05 18.05 8.2 17.42];

magnify = 1/cos(atan(n2));
bfactor = [1 1 magnify 1];
Waistb = Waist.*bfactor;
```

```
%beam quality
%M2 = [1 1 1 1];
M2 = [1 1 1.48 2.1];

% confocal parameter (2 z0)
%b = 2*pi*M2.*Waistb.^2./lambda;
b = M2.*Waistb.^2.*kj;


% focusing parameter
xi1 = 1./b([1 2])
xi2 = 1./b([3 4])


% other factors
k = n1*lambda2/(n2*lambda1);
xi3 = xi1.*xi2*(1+k)./(xi2+ k*xi1);
xi4 = (xi1 + k*xi2)/(1+k);
A = 1/2 + (i/4)*(1./xi3+1./xi4);
C = -1/16*(1./xi3-1./xi4).^2;

h = [];
hm = [];
p = 1;
for p = 1 : 2
        for count = 1 : length(DKl)
            I = @(x,y)exp(i*DKl(count)*(x-y))./((x-A(p)).* ...
                (y-conj(A(p)))+C(p));
            I = dblquad(I,xmin,xmax,ymin,ymax);
            I = real(I);
            h(count) = I/(4*xi4(p));
            %count
        end
        hm(:,p) = h;
end
%dlmwrite('hm.txt', hm, 'delimiter', '\t','precision', 16)
eta = 32*pi*deff^2*1/(n1*n2*n3*c*e0*lambda1*lambda2)*(kj(1)*kj(3)/...
    (kj(1)+kj(3)))*1E12
havg=sqrt(max(hm(:,1))*max(hm(:,2)))
etaeff = eta * havg
max(hm)
plot(DKl,hm)

%------------------------------ sellmeier.m ---------------------------------

function indeks=sellmeier(t,crystal,lambda)

%KTP equations
if  crystal==1;
    dt=t-25;

    az1 = [9.9587 9.9228 -8.9603 4.1010]*1E-6;
    az2 = [-1.1882 10.459 -9.8136 3.1481]*1E-8;
    nz1 = (az1(1) + az1(2)/lambda + az1(3)/lambda^2 + az1(4)/lambda^3);
    nz2 = (az2(1) + az2(2)/lambda + az2(3)/lambda^2 + az2(4)/lambda^3);
    dnz = nz1*dt + nz2*dt^2;
    nz = sqrt(2.12725+1.18431/(1-(0.22690/lambda)^2)+0.6603/(1-...
        (10.0002535/lambda)^2)-0.0096896*lambda^2);

    ay1 = [6.2897 6.3061 -6.0629 2.6486]*1E-6;
    ay2 = [-0.14445 2.2244 -3.5770 1.3470]*1E-8;
    ny1 = (ay1(1) + ay1(2)/lambda + ay1(3)/lambda^2 + ay1(4)/lambda^3);
    ny2 = (ay2(1) + ay2(2)/lambda + ay2(3)/lambda^2 + ay2(4)/lambda^3);
    dny = ny1*dt + ny2*dt^2;
    ny = sqrt(2.1518+0.87862/(1-(0.21801/lambda)^2)-0.01327*lambda^2);

    nx = sqrt(2.1146+0.89188/(1-(-0.20861/lambda)^2)-0.01320*lambda^2);
    dnx = (0.7709 + 1.2307/lambda - 0.4385/lambda^2 + 0.1323/lambda^3)...
        *dt*1E-5;
end

%LBO equations
if  crystal==2;
```

```
    dt=t-20;

    nx=sqrt(2.4542+0.01125/(lambda^2-0.01135)-0.01388*lambda^2);
    dnx=(-3.76*lambda+2.30)*1e-6*(dt+29.13e-3*dt^2);

    ny=sqrt(2.5390+0.01277/(lambda^2-0.01189)-0.01849*lambda^2+...
        4.3025e-5*lambda^4-2.9131e-5*lambda^6);
    dny=(6.01*lambda-19.40)*1e-6*(dt-32.89e-4*dt^2);

    nz=sqrt(2.5865+0.01310/(lambda^2-0.01223)-0.01862*lambda^2+...
        4.5778e-5*lambda^4-3.2526e-5*lambda^6);
    dnz=(1.50*lambda-9.70)*1e-6*(dt-74.49e-4*dt^2);
end

%GdLuCaOBO 0.871
if crystal==3
    dt=t-20;
    nx=sqrt(2.80691+0.02141/(lambda^2-0.01924)-0.00622*lambda^2);
    dnx =0;
    ny=sqrt(2.90342+0.02064/(lambda^2-0.02914)-0.01432*lambda^2);
    dny=0;
    nz=sqrt(2.93547+0.02167/(lambda^2-0.02386)-0.01575*lambda^2);
    dnz=0;
end

%GdLuCaOBO 0.93
if crystal==4
    dt=t-20;
    nx=sqrt(2.80959+0.02181/(lambda^2-0.01889)-0.00691*lambda^2);

    ny=sqrt(2.89898+0.02286/(lambda^2-0.01812)-0.01094*lambda^2);

    nz=sqrt(2.93200+0.02302/(lambda^2-0.01904)-0.01325*lambda^2);
end

%GdScCaOBO 0.96
if crystal==5
    dt=t-20;
    nx=sqrt(2.81268+0.02196/(lambda^2-0.01844)-0.00588*lambda^2);

    ny=sqrt(2.90365+0.02302/(lambda^2-0.01577)-0.01054*lambda^2);

    nz=sqrt(2.93852+0.02255/(lambda^2-0.02078)-0.01362*lambda^2);
end

indeks=[nx+dnx,ny+dny,nz+dnz];
```

A.4 Tuning curves for SDL and 1342nm laser

```
%------------------------------ QPMWave1.m ------------------------------
close all;
clear all;

%Temperautre span, phasematch curves are generated at all these
%Temperatures
T =  [18 43 52];
%T = [30:2:46]; %Temperature span

%These are the limits when seaching for a solution, remember that
lm1 = 0.35; %wavelength lower limit when solving
lm2 = 3.81; %wavelength upper limit when solving

% This determines the span around the iso curves, its made as a lats
% minute attempt so it does not quite follow the phasematch curves but you
% can play alon with it.
span = 5; %span around the generated lambda3 for making iso curves

%This is the value for the poling since the program can also be changed for
%seaching for the optimum poling period its called poleguess ;-)
%for mixing 1342 and 1064
Lpoleguess = 12.5988430184509 % polings gæt i mu m
%for 1342 and 766 Lpoleguess = 7.1;
```

```
24
    %initial guess for phasematching it has to be something in order to start
    %the lsqnonlin solver
    lambda1 = 1.342;

29  %wavelength in mu m for beam 1
    lambda2 = [1.040:0.0001:1.0700];
    lambda3 = 1./(1./lambda1+1./lambda2); %wavelength in mu m for SFG
    crystal = 1;          %1=KTP, 2=LBO 3=SLT 4 and higher = special crystals
    %the checker determines which parameter to solve for. temp and poling are
34  %used the first time one recieves a crystal to check its specifications
    checker = 3;          %1=temp, 2=poling, 3=Wavelength 1

    data = [];
    count = 0;
39  %crystal directions 3 = z
    %PPKTP x=y=z=3
    % LBO x=y=3 z=2 /121
    x=3;
    y=3;
44  z=3;
    input=lambda1;
    for temp = 1 : length(T)
        Tguess = T(temp); %here is the temerature that is the initial guess
        for count = 1 : length(lambda2)
49              guess=nulcheckp(crystal,Tguess,Lpoleguess,lm1,lm2,input,...
                    lambda2(count),lambda3(count),x,y,z,checker);
                data = [data; lambda2(count) guess];
                input = guess(1);
        end
54  end

    %generating iso curves where the generated wavelength is constant.
    iso = [];
    % a is the bottom iso curve and b is the top one there value is plotted in
59  % the command window
    a = floor(lambda3(1)*1000-span)
    b = ceil(lambda3(length(lambda3))*1000+span)
    for l3 = a :2: b
        iso = [iso; 1./(1/(l3/1000) - 1./lambda2)];
64  end
    % plotting iso courves
    plot(lambda2,iso,'-.')
    hold on
    % measured data at 52, 43 and  18-18.4
69  plot([1.06326 1.06409 1.06466],[1.34429 1.3428 1.3417],'o',...
        'LineWidth',2,'MarkerFaceColor','b')
    plot([1.06196 1.06324 1.06368],[1.3443 1.3426 1.3418],'o',...
        'LineWidth',2,'MarkerFaceColor','r')
    plot(1.06109,1.3419,'o','LineWidth',2,'MarkerFaceColor','g')
74  %new data points at 18
    plot([1.05948 1.06070 1.06116],[1.3441 1.34247 1.34162],'o',...
        'LineWidth',2,'MarkerFaceColor','g')
    plot(data(:,1),data(:,2),'x')
    hold off
79  line([lambda2(1) lambda2(length(lambda2))],[1.3445 1.3445])
    line([lambda2(1) lambda2(length(lambda2))],[1.3417 1.3417])
    %axis([1.050 1.070 1.340 1.345])
    %text(1.066,1.3434,'594nm', 'rotation',-78)
    %text(1.059,1.3434,'592nm', 'rotation',-78)
84  %text(1.052,1.3434,'590nm', 'rotation',-78)
```